ROYAUME DU MAROC
Université Mohammed V - RABAT -
جامعة محمد الخامس – الرباط –
Faculté des sciences
كلية العلوم
CENTRE D'ETUDES DOCTORALES - SCIENCES ET TECHNOLOGIES

N° d'ordre : 3393

# THESE

En vue de l'obtention de : **DOCTORAT**

Structure de Recherche : Laboratoire de Matière Condensée et Sciences Interdisciplinaires

Discipline : Physique Informatique

Spécialité : Matière condensée et modélisation des Systèmes

Présentée et soutenue le : 20/02/2021 par :

Rachid BOUACHRAOUI

## Study of electronic, magnetic properties of Troilite FeS and magnetocaloric properties of $MnFe_4Si_3$ alloy: Monte Carlo and ab initio framework.

### JURY

| | | |
|---|---|---|
| *Abdelilah BENYOUSSEF,* | *PES, Académie Hassan II Des Sciences Et Techniques, Rabat* | *Président* |
| *Moulay Brahim SEDRA,* | *PES, Faculté des Sciences et Techniques, Errachidia, Université Moulay Ismail, Meknes* | *Rapporteur/Examinateur* |
| *Rachid MASROUR* | *PH, Faculté des sciences, Univeristé Dhar El Mahraz, Fès* | *Rapporteur/Examinateur* |
| *Hamid EZ-ZAHRAOUY,* | *PES, Faculté des Sciences, Université Mohammed V Rabat* | *Rapporteur/Examinateur* |
| *Omar EL BOUNAGUI,* | *PH, Faculté des Sciences, Université Mohammed V , Rabat* | *Rapporteur/Examinateur* |
| *Mohammed LOULIDI,* | *PES, Faculté des Sciences, Université Mohammed V , Rabat* | *Examinateur* |
| *Najim TAHIRI* | *PA, Faculté des Sciences, Université Mohammed V, Rabat* | *invité* |
| *Lahoucine BAHMAD,* | *PES, Faculté des Sciences, Université Mohammed V Rabat* | *Directeur de Thèse* |

Année Universitaire: 2020/2021

✉ Faculté des Sciences, avenue Ibn Battouta, BP. 1014 RP, Rabat –Maroc
☎ 00212(0) 37 77 18 76 🖷 00212(0) 37 77 42 61 ; http://www.fsr.ac.ma

*Dedication*

*To*

*My mother*

*My brothers and sisters*

*All my professors and teachers*

*All my friends*

# Acknowledgement

This thesis has been carried out at the Laboratory of Condensed Matter and Interdisciplinary Sciences (LaMCScI), Faculty of Science, Mohammed V University – Rabat, under the supervision of Mr. Lahoucine BAHMAD Professor of Higher Education at the Faculty of Sciences of Rabat.

First, praises and thanks go to Allah, the Almighty, for his unlimited and uncountable blessings in my whole life and throughout my research work especially.

On this page, I would like to express my very great appreciation, deep gratitude and sincere thanks to my first supervisor, Mr. Lahoucine BAHMAD, Professor of Higher Education at the Faculty of Sciences of Rabat. For giving me this opportunity to learn from their valuable expertise and to have the fruitful discussions with them. They always had time to answer my questions and they patiently provided the vision, encouragement and advise necessary for me to proceed throughout my research period. It is my privilege to be their student.

Besides my supervisor, I would like also to offer my thanks to the thesis committee for reviewing my thesis and giving their insightful and useful comments.

I would like to thank the president of the thesis committee Mr. Abdelilah BENYOUSSEF Professor of Higher Education from Hassan II Academy of Science and Technology Rabat. For reviewing this PhD thesis.

I would like also to offer my special thanks to Mr. Moulay Brahim SEDRA, Professor of Higher Education from Faculty of Science and Technology Errachidia. For reviewing and reporting my thesis.

I would like also to offer my special thanks to Mr. Rachid MASROUR, Proficiency Professor from Faculty of Science Dhar El Mahrez, Fès. For reviewing and reporting my thesis.

I would like to thank Mr. Hamid EZ-ZAHRAOUY, Professor of Higher Education from Faculty of Science Rabat. For reviewing and reporting this thesis.

I would like to offer my thanks to Mr. Omar EL BOUNAGUI, Proficiency Professor from Faculty of Science Rabat, for reviewing and reporting this thesis.

I would also like to extend my thanks to Mr. Mohamed LOULIDI, Professor of Higher Education from Faculty of Science Rabat. For reviewing my thesis.

I would also like to thank Mr. Najim TAHIRI Assistant Professor from Faculty of Science Rabat. or reviewing my thesis.

I would like also thanks all the professors of Laboratory of Condensed Matter and Interdisciplinary Sciences for their valuable suggestions and discussions.

I would also like to extend my thanks to my colleagues especially, Mr. Y. Ziat, Mr. H. Bouda, and M. Bouchtaoui.

Special thanks to my mother, my brothers and sister, for their support, patience and encouragement throughout my study.

Finally, i wish to thank my friend for their support and encouragement.

# Abstract

In this thesis, we studied the magnetic properties of the FeS and MnFe4Si3 compounds which are characterized by the very high Curie temperature. First, for the compound FeS we calculated the interaction couplings and described the electronic properties by intervening the approximation of the functional density theory (DFT), thus by the implementation of the Metropolis code within the framework of the model from Ising we deduce the phase diagrams and the magnetic properties of FeS. We also studied the magnetocaloric effect and the magnetic properties in the MnFe4Si3 alloy by Monte Carlo simulation method (MCS) after having calculated the interaction couplings carried out by experimental studies. This simulation shows the performances and the functionalities of these compounds in various fields. Then, we carried

out a study by MCS to investigate the magnetic frustration in a square lattice due to the competition of the ferromagnetic and antiferromagnetic coupling so we identify the different possible states and precisely the frustrated state, so we studied the magnetic properties and the hysteresis cycles for each state.



**Keys words**: Monte Carlo simulation; Functional Density Theory; Magnetocaloric Effect; Magnetic Frustration.

# Résumé

Dans cette thèse, Nous avons étudié les propriétés magnétiques des composés **FeS** et **$MnFe_4Si_3$** qui sont caractérisés par la température de Curie trés élevée. D'abord, pour le composé **FeS** nous avons calculé les couplages d'interactions et décrit les propriétés électroniques en intervenant l'approximation de la théorie fonctionnelle de la densité (DFT), ainsi par l'implémentation du code Métropolise dans le cadre du model d'Ising on déduit les diagrammes de phase et les propriétés magnétiques du **FeS**. Nous avons étudié également l'effet magnétocalorique et les propriétés magnétiques dans l'alliage **$MnFe_4Si_3$** par méthode de simulation Monte Carlo (MCS) après avoir calculer les couplages d'interactions menés par les études expérimentales. Cette simulation a permis de mettre en évidence les performances et les fonctionnalités de ces composés dans différents domaines. Ensuite, nous avons mené une étude par MCS pour étudier la frustration magnétique dans un réseau carré due à la compétition des couplage ferromagnétique et antiferromagnétique ainsi on identifie les différents états possibles et précisément l'état frustré, de même on étudie les propriétés magnétiques et les cycles d'Hystérésis pour chaque état.



**Mots-clefs:** Simulation Monte Carlo; théorie fonctionnelle de la densité; Effet Magnétocalorique; Frustration magnétique.



✉ Faculté des Sciences, avenue Ibn Battouta, BP. 1014 RP, Rabat –Maroc

☎ 00212(0) 37 77 18 76 🖷 00212(0) 37 77 42 61 ; http://www.fsr.ac.ma

# Résumé détaillé

Dans le domaine de la matière condensée, les nouveaux outils basés sur la modélisation des structures des matériaux et la simulation de leurs propriétés physiques, à différentes échelles, ont prouvé leur efficacité pour comprendre la structure complexe des nouveaux matériaux

synthétisés et prédire des matériaux aux propriétés exceptionnelles pouvant être utilisés dans de nouvelles applications. Grâce à la grande précision de la description des propriétés des matériaux, ces outils sont aujourd'hui de plus en plus utilisés dans le développement de nouveaux matériaux et pour l'interprétation des résultats expérimentaux. En outre, ces outils de modélisation sont capables d'aller au-delà des limites des mathématiques et des capacités expérimentales gérables. La simulation Monte Carlo (MCS) et les approches de terrain efficaces appartiennent à cette catégorie d'outils. La MCS, en particulier, tire sa puissance de décennies de recherche intense basée essentiellement sur deux développements tout aussi importants que sont les puissants algorithmes numériques et les capacités matérielles en termes de stockage et de calcul des systèmes informatiques modernes qui ont connu une évolution croissante grâce à la réduction continue de l'échelle des dispositifs microélectroniques.

Dans cette thèse, nous concentrons notre étude sur les propriétés magnétiques des matériaux magnétiques à base de Fe dont la température de Curie la plus élevée a été mesurée jusqu'à présent dans les oxydes magnétiques. Ainsi, nous avons utilisé des méthodes statistiques, telles que les simulations de Monte Carlo (MCS) et la théorie fonctionnelle de la densité (DFT) pour développer une connaissance théorique détaillée du comportement magnétique et des effets de certains phénomènes tels que l'hystérésis pour la frustration magnétique dans un réseau carré 2D et l'effet magnétocalorique pour l'alliage $MnFe_4Si_3$ dans le cadre du modèle tridimensionnel d'Ising.

Les matériaux magnétiques dont la température de Curie est la plus élevée au voisinage de la température ambiante constituent un matériau approprié pour la réfrigération magnétique, ils se caractérisent par un effet appelé : effet magnétocalorique (MCE), leurs processus adiabatiques et

isothermes en présence d'un champ magnétique externe appliqué en font de bons candidats par rapport aux technologies traditionnelles (le réfrigérateur à compression de vapeur) qui entraînent un impact négatif sur l'environnement.

De nombreuses études consacrées à l'élucidation du principe de la réfrigération magnétique ont été réalisées :

- Cycle de Brayton.
- Cycle Ericsson.
- Cycle de la RAM.

D'autre part, le degré élevé de polarisation du spin dans les matériaux magnétorésistifs tels que le composé à base de Fe étudié ici est censé résulter de l'effet du champ magnétique externe appliqué. La magnétorésistance géante (GMR) est connue pour être étroitement liée aux matériaux à forte polarisation de spin, qui rendent les matériaux à forte polarisation de spin essentiels dans les applications spintroniques. Cependant, diverses familles de composés semi-métalliques qui ont un ferro/ferrimagnétisme n'ont pas montré de grandes valeurs de magnétorésistance par effet tunnel à température ambiante, en raison de leurs basses températures de commande. Par conséquent, il est important de développer la fiabilité des matériaux ferromagnétiques, semi-métalliques, tels que les matériaux à base de Fe, qui présentent des températures de transition élevées dans le domaine de la spintronique.

Dans les matériaux et dispositifs de spintronique, la forte corrélation entre la direction du spin (spin-up ou spin-down) et la charge des porteurs de conduction sont les principaux facteurs. Des porteurs de conduction à spin élevé à température ambiante ont été trouvés dans quelques matériaux ferro/ferrimagnétiques comme les doubles pérovskites (DP) avec des propriétés intéressantes promettant leur utilisation dans des applications spintroniques. La composition chimique et la structure cristalline des DP offrent une grande variété de possibilités pour trouver d'autres matériaux à forte polarisation de spin, avec une température de transition élevée et une magnétisation importante, adaptés aux applications spintroniques. Des applications nouvelles et intéressantes telles que les capteurs avancés et les mémoires magnétiques ont été réalisées à

partir de la manipulation du spin des électrons dans le traitement de l'information. Les capteurs de champ magnétique très sensibles dans les têtes de lecture d'enregistrement pour les lecteurs de disques magnétiques sont l'une de ces applications importantes. De même, l'ingénierie spintronique peut réaliser des matériaux potentiellement appropriés pour de nouvelles mémoires à semi-conducteurs.

Dans la première partie de cette thèse, nous étudions le sujet lié aux méthodes de simulation numérique afin d'en élucider les principes et les piliers tels que la théorie fonctionnelle de la densité (DFT) et la simulation de Monte Carlo. Ces méthodes présentent un grand intérêt pour les domaines de la physique et constituent donc une technique digne de ce nom pour déterminer les propriétés des systèmes physiques. D'autre part, nous décrivons certains domaines d'application de notre composé comme la spintronique et la réfrigération magnétique

Dans la deuxième partie de cette thèse, nous présentons un nouveau composé consacré à des applications potentielles telles que la spintronique et la réfrigération magnétique. Nous jetons ainsi un peu de lumière sur les données expérimentales et théoriques existantes, et essayons de fournir des interprétations et une compréhension théorique des phénomènes considérés.

Dans le chapitre 1 de la deuxième partie, nous étudions les diagrammes de phase et les propriétés magnétiques du FeS en utilisant différentes méthodes de simulation, telles que AB initio et la simulation de Monte Carlo dans le cadre du modèle d'Ising, le composé a un système de spin (s=2). Ces deux méthodes ont donc été utilisées pour analyser les diagrammes de phase et étudier les propriétés magnétiques du composé FeS. Nous avons d'abord présenté la structure du composé et le modèle d'Ising adopté pour décrire toutes les interactions pertinentes au sein de la structure. Ensuite, nous avons établi les diagrammes de phase des états possibles. En se basant sur théorie fonctionnelle de la densité (DFT) et de la méthode FPLAPW (Full Potential Linearized Augmented Plane-Wave) qui est implémentée dans le code WIEN2K [14], nous étudions les propriétés magnétiques du Troilite FeS, le potentiel de corrélation d'échange a été traité en utilisant l'approximation du gradient généralisé (GGA) pour les calculs de l'énergie

totale [15]. Ensuite, nous avons effectué une étude par MCS combinée avec l'algorithme de Metropolis, nous avons présenté le diagramme de phase en fonction des différents couplages d'échange. Nous avons calculé la magnétisation et la susceptibilité magnétique à l'aide de la MCS.

Dans le chapitre 2, nous discutons la frustration magnétique due à la compétition des couplages d'échange ferromagnétiques et antiferromagnétiques ($J_1$, $J_2$) avec les premiers et les seconds proches voisins dans un réseau carré dans le cadre du modèle d'Ising, nous avons d'abord élaboré les diagrammes de phase de l'état fondamental. Ensuite, nous avons discuté des différentes propriétés magnétiques de ce système en utilisant la MCS.

Le chapitre 3 est consacré à l'étude de l'effet magnétocalorique du $MnFe_4Si_3$ en utilisant la MCS dans le cadre du modèle d'Ising. Le modèle a été construit pour décrire le composé comme un système mixte de spin (3/2, 3/2). En intervenant les données expérimentales pour déduire les couplages d'échange (J1, J2) avec les premiers et seconds proches voisins. Ensuite, nous avons établi les diagrammes de phase de l'état fondamental et on détermine la phase stable correspondant aux couplages d'échange (J1, J2). Dans le cadre de MCS, nous avons calculé la magnétisation et la susceptibilité à partir desquelles nous avons déduit la température de transition $T_C$ = 290K. Nous avons également étudié les propriétés magnétocaloriques de notre composé, telles que la variation d'entropie magnétique $\Delta S_m$, la variation de température adiabatique $\Delta T_{ad}$ et la puissance de refroidissement relative RCP, ces résultats obtenus sont bien confirmés par les travaux expérimentaux et renforcent la possibilité que le MnFe4Si3 soit un candidat très prometteur pour les applications de réfrigération magnétique.

Dans le chapitre 4, nous étudions les propriétés magnétoélectriques du SnO2 dopé au molybdène en utilisant la méthode DFT. Nous concluons que la stabilité FM est observée, puisque le spin majoritaire de l'état $t_{2g}^{+}$(Mo) se situe autour du niveau de Fermi à 0 Ry, le comportement semi-métallique de notre composé le rend approprié pour les applications magnétoélectroniques.

# Table of Figures

# Table of content

# List of publications

1. frustrated square lattice Ising model: Monte Carlo study
   Rachid Bouachraoui, Younes Ziat, Najim Tahiri, Lahoucine Bahmad, Omar El Rhazouani, Abdelilah Benyoussef, *Mater. Res. Express (*2019) https://doi.org/10.1088/2053-1591/ab0632

2. Magnetic and electronic properties of FeS: Monte Carlo and Ab initio studies
   Rachid Bouachraoui, Abdel Ghafour El Hachimi, Younes Ziat, Lahoucine Bahmad, Najim Tahiri , Solid State Communications 274 (2018)

3. Magnetic and Magnetocaloric properties of $MnFe_4Si_3$: Monte Carlo study
   Rachid Bouachraoui, Younes Ziat, Younes Sbai, Omar El Rhazouani, Fayçal Goumrhar, Lahoucine Bahmad, Journal of Alloys and Compounds 809, (2019)

4. Investigation on (*molybdenum-doped-$SnO_2$*) for potential use in magnetoelectronic applications: the DFT framework
   Younes Ziat, Maryama Hammi**,** Zakaryaa Zarhri, Charaf Laghlimi, Rachid Bouachraoui, Omar El Rhazouani, Julio Cesar Cruz Argüello, International Journal of Modern Physics B (2020) DOI: 10.1142/S0217979220500204

# List of Abbreviations

| | |
|---|---|
| **2D** | **TWO DIMENSIONAL** |
| **3D** | Three Dimensional |
| **AF** | Anti-Ferromagnetic |
| **DFT** | Density Functional Theory |
| **FI** | Ferrimagnetic |
| **DOS** | Densities Of States |
| **CFT** | Crystal Field Theory |
| **DRAM** | Dynamic Random Access Memory |
| **F** | Ferromagnetic |
| **SAF** | Super Anti Ferromagnetic |
| **GMR** | Giant Magneto-Resistance |
| HDD | Hard Disc Drives |
| **HMF** | Half-Metallic Ferrimagnetism |
| **RCP** | Relative Cooling Power |
| **AMR** | Active Magnetic Regenerator |
| IT | Information Technology |

| | |
|---|---|
| **MCMC** | Markov Chain Monte Carlo |
| **MCE** | Magetocaloric effect |
| **MCS** | Monte Carlo Simulation |
| **RTD** | Resonant Tunneling Device |
| **MIN** | Magnetic Insulator |
| **MRAM** | Magnetic Random Access Memory |
| **MTJ** | Magnetic Tunnel Junction |
| **NN** | Nearest-Neighbors |
| **NNN** | Next Nearest-Neighbors |
| **SE** | Super Exchange |
| **SOC** | Spin-Orbit Coupling |
| **SRAM** | Static Random Access Memory |
| **XRD** | X-Ray Powder Diffraction |

# Part 1: Methods of calculation

## 1.1 Ab-initio method

### 1.1.1 Schrödinger equation for many-body problem

Numerical simulations based on so-called ab initio calculation have gained a well-known place in modern and condensed matter physics. They can be used to guide or to plan future experiments by means of a rational process.

In order to investigate the properties of molecules, atoms and solids, the so-called Schrödinger equations is the basic tool that the solid state theorist works with. The time-independent Schrödinger equation has the form:

$$\hat{H}\Psi = E\,\Psi \qquad (1.1)$$

where $\Psi$ is the many-body wave-function, Eis the total energy and $\hat{H}$is the Hamiltonian of system.

The Hamiltonian can be written as a sum of five terms as follows:

$$\hat{H} = T_{core} + V_{core-core} + T_e + V_{e-e} + V_{core-e} \qquad (1.2)$$

Given that

$T_{core} = -\sum_{k=1}^{N_0} \frac{1}{2M_k} \Delta_{R_k}$ is the kinetic energy of the nuclei

$V_{core-core} = +\sum_{k<k'} \frac{Z_k Z_{k'}}{R_{kk'}}$ is the interaction energy between the nuclei

$T_e = -\sum_{i=1}^{N} \frac{1}{2} \Delta_{r_i}$ is the kinetic energy of the electrons

$V_{e-e} = +\sum_{i<j'} \frac{1}{r_{ij}}$ is the interaction energy between electrons

$V_{core-e} = -\sum_{k,i} \frac{z_k}{r_{ik}}$ is the interaction energy between electrons and nuclei

In the above terms, the distance between *i*-th and *j*-th electron is: $r_{ij} = |r_i - r_j|$ , the distance between *i*-th elextron and *k*-th nucleus is: $r_{ik} = |r_i - R_k|$ and the distance between the *k*-th nucleus and *k'*-th nucleus is :$R_{kk'} = |R_k - R_{k'}|$. In atomic units, the energy in Hartee and the length in Bohr.

With:

- $N_0$ is the total number of nuclei in the system and $N$ is the total number of electrons in the system.

- The indexes *k* and *k'* refer to the nuclei.

- The indexes $i$ and $j$ refer to the electrons.

- $r_i$ is the position of the electron $i$ .

- $R_k$ is the position of the nucleus $k$ .

- $Z_k$ is the charge of the nucleus $k$ .

In fact, it is not possible to solve this equation and there are many difficulties underlying the application of this technique to different classes of system, so, the use of approximations and methods are required. For example, the solid system is described by many electron wave functions $\Psi(x_1, x_2, \ldots . x_{N-1}, x_N)$ which become very complicated where each $x_i$ determinates the position and spin of each particle, given that, the Schrödinger equation should to solve $10^{23}$ simultaneous different equations.

### 1.1.2 The Born-Oppenheimer approximation

The Born-Oppenheimer approximation [1] has an essential role in electronic structure calculations. The underling rationalization of this approximation is that the mass of nuclei is

already 1835 times the mass of an electron (case of the hydrogen atom). According to that, they assumed that the nuclei move much more slowly than electrons, subsequently, we can consider the electrons are moving in a field produced by the fixed nuclei. Base on Born-Oppenheimer approximation, the $T_{core}$and $V_{core-core}$ operators are neglected in equation **(2.2)**, where the repulsion between nuclei, can be considered as a constant for a fixed configuration of the nuclei, subsequently, the remaining part of the equation **(2.2)** is called the electronic Hamiltonian, noticed $\hat{H}_{elec}$.

$$\hat{H}_{elec} = T_e + V_{e-e} + V_{core-e} \qquad (1.3)$$

At this stage the expression of the electronic wave function is:

$$\Psi_{elec} = \Psi_{elec}(r_i, R_k) \qquad (1.4)$$

Even Born-Oppenheimer approximation permits to separate the Schrödinger equation into independent electronic and nucleonic parts, the solving of this for electronic part is still theoretically a very complicated. Subsequently the uses of approximations besides methods are required.

### 1.1.3 Hartree-Fock approximation

The Hartee-Fock (HF) approximation has a remarkable position, since it is facilitating the way to more accurate calculations, thus, it is useful to solve the electronic wave function related to equation **(2.4)**. The HF approximation is used to investigate various the problems connected to materials science, as defects in solids [2] and electronic structure of insulators [3].

Even the HF approximation provides an exact description of electron exchange and includes the electron spins, it is ignored the electrons correlation property. Then, the energy associated with this approach must be different from the exact energy by an energy difference, which is called

the correlation energy. Known that the movement of a given electron affects and is affected by the movement of the other particles. Then, this is the major limitation of the HF approximation, for atoms and small molecules. While this approximation is still going on in terms of the total energy error, the limitation could be around 0.5% in a carbon atom, where the total energy is around 1000 eV, which already reaches the order of magnitude of chemical single bond energy. That is to say, to obtain a reliable description of chemical reactions, more approximations are required. This can be achieved within the wave-function based approximations and by making more elaborate methods for the many-body wave function, such as the configuration Interaction (CI) method [4], also the Møller-Plesset (MP) perturbation theory[5], and the Coupled-Cluster (CC) method [6] have achieved the greater success in the last years.

### 1.1.4 Density functional theory

Density functional theory (DFT) is a popular and successful computational quantum mechanical modeling method used in physics, materials science and chemistry. It is to study the electronic structure of many-body systems, such as molecules and atoms. The basic concept of DFT is to deal with a formulation of this many-electron problem that involves the total density of electrons instead of using the many-electron wave function in that formulation without any loss of information. In fact, Thomas [7] and Fermi [8] proposed the earliest form of DFT. Additionally, in 1964 Hohenberg and Kohn [9] demonstrated the fundamental importance of the electronic density in their theorems. After that, in 1965, Kohn and Sham [10], further developed the theory into a framework for real calculations. In many cases the results of DFT calculations for solid state studies agree quite acceptably with experimental data.

#### 1.1.4.1 Thomas-Fermi-Dirac theory

The earliest model of density functional theory proposed in 1927 by Thomas and Fermi. This model is Thomas-Fermi (TF), which used the electron density $\rho(r)$ as the basic variable instead of the wave function.

The total energy is represented, by terms defining the kinetic energy, the Coulomb interactions of

electron-electron (internal potential), nucleus-electron (external potential ), as an explicit functional of the total density of electrons. In an external potential $V_{ext}(r)$, the total energy of the system is given as a functional of the electron density ρ(r), its expression is:

$$E_{TF}[\rho] = C_F \int \rho^{\frac{5}{3}}(r)dr + \int \rho(r)V_{ext}(r)dr + \frac{1}{2}\iint \frac{\rho(r_1) - \rho(r_2)}{|r_1 - r_2|} dr_1 dr_2 \qquad (1.5)$$

Where the first, second and third terms are: the kinetic energy of the non-interacting electrons in the homogeneous electron gas model (HEG). The classical electrostatic energy of the nucleus-electron Coulomb interaction and the classical electrostatic Hartree energy approximated by the classical Coulomb repulsion between electrons.

With$C_F = \frac{3}{10}(3\pi^2)^{\frac{5}{3}} = 2.871$

And the electron density $\rho(r) = N \int \dots \int |\Psi(x_1, x_2, \dots, x_N)|^2 dx_1 dx_2 \dots dx_N$ (1.6)

When $\rho(r)$ verifies the probability of finding any of the *N* electrons within the volume *r;* however, with arbitrary spin with N-1 electrons have arbitrary positions and spin in state represented by wave function. Given that $x_i$ represents both spatial and spin coordinates.

Dirac [11] extended the equation **(2.5)** by adding a local exchange term $C_D \int \rho^{\frac{4}{3}}(r)dr$, subsequently, the Thomas-Fermi-Dirac equation is:

$$E_{TFD}[\rho] = C_F \int \rho^{\frac{5}{3}}(r)dr + \int \rho(r)V_{ext}(r)dr + \frac{1}{2}\iint \frac{\rho(r_1) - \rho(r_2)}{|r_1 - r_2|} dr_1 dr_2 + C_D \int \rho^{\frac{4}{3}}(r)dr$$

(1.7)

With $C_D = -\frac{3}{4}(\frac{3}{\pi^2})^{\frac{1}{3}}$.

1.1.4.2 Hohenberg-Kohn theorems

Hohenberg-Kohn (HK) demonstrated that the Thomas-Fermi model is in fact an approximation for an exact theory called DFT. They based on the two fundamental theorems, noticed HK-theorems [9-10] which are mentioned below:

Theorem 1. For any system of interacting particles in an external potential $V_{ext}(r)$, the potential $V_{ext}(r)$ is determined uniquely, except for a constant, by the ground state density $\rho_o(r)$.

Theorem 2. There exists a universal functional $F[\rho(r)]$ of the density, independent of $V_{ext}(r)$, such as the global minimum value of the energy functional, where, the exact ground state energy of the system is

$$E[\rho(r)] = \int \rho(r)V_{ext}(r)dr + F[\rho(r)] \qquad (1.8)$$

The proof of the first theorem is remarkably simple and proceeds by *reductio ad absurdum*. With two different external potentials, $V_{ext}(r)$ and $V'_{ext}(r)$, that give rise to the same density $n_o(r)$. The associated Hamiltonians ($\hat{H}$and $\hat{H}$'), will therefore have different ground state wave functions ( $\Psi$ and$\Psi'$), that each yield $\rho_o(r)$.

With $E_0$ and $E_0$', the ground state related to $\hat{H}$and $\hat{H}$' respectively,

$$E_0 < \langle\Psi'|\hat{H}|\Psi'\rangle = \langle\Psi'|\hat{H}'|\Psi'\rangle + \langle\Psi'|\hat{H} - \hat{H}'|\Psi'\rangle$$

$$= E'_0 + \int \rho_0(r)[V_{ext}(r) - V'_{ext}(r)]dr \qquad (1.9)$$

Hohenberg-Kohn theorems apply rigorously only to the ground state. Given that:

$E_0 + E_0' < E_0' + E_0$ (1.10)

The ground state density uniquely determines the external potential within an additive constant.

To the proof the second theorem,

The universal functional $F[\rho(r)]$ can be written as the follow:

$$F[\rho(r)] = T[\rho(r)] + E_{int}\,[\rho(r)] \qquad (1.11)$$

The kinetic energy and the interaction energy of the particles are $F[\rho(r)]$ and $E_{int}[\rho(r)]$ respectively, at this point, for the variation principle, the energy functional is:

$$E[\Psi] = \langle \Psi' | \hat{T} + \hat{V}_{\cdot int} + \hat{V}_{\cdot ext} | \Psi' \rangle \qquad (1.12)$$

Thus, the energy functional density **(1.8)** evaluated for the correct ground state density $\rho_0(r)$is indeed lower than the value of this functional for any other $\rho(r)$. Then by minimizing the total energy functional of the system with respect to variations in $\rho(r)$ , one would find the exact ground state density and energy.

The HK theories are generalized in the theory of spin density functional, with spin degrees of freedom, integrated the particle density and the spin density related to $\rho(r) = \rho\uparrow(r) + \rho\downarrow(r)$ and $S(r) = \rho\uparrow(r) + \rho\downarrow(r)$ , respectively, with ↑and ↓are the different varieties of spin, thus, the energy functional is we generalize into *E[ρ(r),S(r)]*

### 1.1.5 Kohn-Sham theorem

The HK theorems clarify that the electron density can be uniquely used rather than the wave function to determine the fundamental quantity of the many-body problems.

nevertheless, these theorems are still only pure ideas, since the calculating of the kinetic energy of interacting system does not give enough precision.
In 1964, Kohn and Sham (KS) [12] proposed a formalism to calculate *E[ρ]* based on the wave functions, subsequently they decided to describe the idea of one electron orbitals and approximate the kinetic energy of the system by the kinetic energy of non-interacting electrons. In fact, the KS formalism reduces the problem with many electrons to a problem only mono-electronic. Hence, The Kohn-Sham lead to the one electron Schrödinger-like equation called the Kohn-Sham equation which is expressed as:

$$\varepsilon\phi_i = (-\frac{1}{2}\nabla^2 + V_{eff})\phi_i \qquad (1.13)$$

where $V_{eff} = V_{ext} + V_H + V_{xc} = V_{ext}(r) + \int \frac{\rho(r)}{|r_1 - r_2|} dr_2 + \frac{\delta E_{xc}[\rho]}{\delta\rho(r)}$ (1.14)

The $\varepsilon$ are the energy of the KS-orbital where $\phi$ are the Kohn-Sham orbitals. Where $-\frac{1}{2}\nabla^2$ and $V_{eff}$ are the kinetic energy of non-interaction reference system and the effective potential. The $V_{eff}$ included the sum of the external potential, the Hartree potential and $E_{xc}$ energy-correlation potential, respectively.

The electron density is $\rho = 2\sum_{i=1}^{\frac{1}{2}N} |\phi_i|^2$ (1.15)

Here, the non-interacting kinetic energy is given by:

$$T_S[\rho] = -\sum_{i=1}^{\frac{1}{2}N} \int \phi_i^*(r)\nabla^2\phi_i(r)dr \qquad (1.16)$$

For $\varepsilon_i$ energies, the factor 2 is for spin degeneracy, we assume the orbitals are singly occupied. Subsequently, the energy of the non-interacting system, the sum of one-electron eigenvalues is

$$2\sum_{i=1}^{\frac{1}{2}N} \varepsilon_i = T_S[\rho] + \int \rho(r) V_{eff}(r) dr \qquad (1.17)$$

For that, the total energy can be obtained from the resulting density throughout:

$$E = 2\sum_{i=1}^{\frac{1}{2}N} \varepsilon_i - \frac{1}{2} \iint \frac{\rho(r_1) - \rho(r_2)}{|r_1 - r_2|} dr_1 dr_2 - \int \rho(r) V_{xc}(r) dr + E_{xc}[\rho] \qquad (1.18)$$

The KS equations should be solved self consistently. Within DFT calculations, only the total energy, the Fermi energy and the electron density have a physical meaning. The states and energies of KS are only intermediated calculations.

## 1.2 Monte Carlo Method

### 1.2.1 Introduction

A Monte Carlo method is a technique that involves using random numbers and probability to solve problems. The term Monte Carlo Method was coined by S. Ulam and Nicholas Metropolis in reference to games of chance, a popular attraction in Monte Carlo, Monaco, it is concerned with experiments study. This research tool is extensively used and applied by many professionals of different fields, be it Medicine, Finance, Biology, Physics Operational Research and so forth.

Thus, in business, MCS technics are suitable in modeling phenomena with high performance of uncertainty of initial data such as the calculation of risk; in application to space and oil exploration problems; in math, MCS is performed to evaluate the multidimensional definite integrals in the case of complicated boundary conditions; Predictions provided by MCS methods in term of failure, cost overruns (unexpected costs that appear in the budget resulting from an underestimation of the actual cost during budgeting) and schedule overruns are generally more accurate than human intuitions or other alternative methods [**42**].

- There is a diverse variety of MCS techniques that follow a common pattern.
- Collect all possible input of domain
- Exploit a random process to generate the inputs over the domain according to a probability distribution.
- Then, calculation of the grandeurs in consideration is performed in a deterministic way after reaching the equilibrium.
- Lastly, collect the results.

In whole field of physics, MCS method proves to be a reliable technique to study the behavior of various complex systems and determinate thermodynamic, magnetic properties of physical systems. The process of MCS crucially depends of the ‘time dependence’ of a model. The time dependence is commonly known as MCS steps that constitute the basis of the stochastic process in which the model changes according on a sequence of random numbers that are generated

during the simulation [**43**].

The principle base of MCS to resolve problems in the field of statistical physics either in the case of equilibrium or in the case of out-of-equilibrium is founded on numerical resolution of systems by observing their evolution in the time until reaching the equilibrium [**44**].

The processes of MCS based on a sampling algorithm such as the Metropolis algorithm is the most popular and simple one, which is pertinent to a varied class of problems involving starts and end situations. The algorithm was named after Nicholas Metropolis who first has proposed to solve the specific case of the canonical ensemble by the use of this algorithm [**45**].

The Markov chain Monte Carlo (MCMC) method is the simple example of Metropolis algorithm, that uses a probability distribution to create samples in a random sequence. This sequence serves thus as approximation of the distribution. The principal idea of this algorithm will be described in the next sections. then, the use of MCS method in combination with Metropolis algorithm reveals its great efficiency in studying the physical properties of compounds with complex structures and complex intertwined interactions and behaviors, but its power is still limited by the computing time and the memory it requires [60].

In condensed matter the main constraint is the big number of particles that lead to many problems related to the type of interactions and structure of the system, which makes difficult to find sufficient answers of all issues in consideration. Thus, that it is obvious that the answers provided by analytical methods are only approximate answers. Therefore, simulation methods like MCS are Numerical computer-based technics that are now used widely as important complementary method to further develop the understanding of complex physical systems and phenomena. Spin glasses, spin solutions, order-disorder phase transitions and critical phenomena, etc. all of them, systems and phenomena that are studied using MCS. In addition, other topics in physics use increasingly the classical simulation methods as approximation technics after suitable mappings such as the broad field of elementary particle physics, quantum gravity, and quantum statistical problems [**43**, **44**, **46**].

In addition to enhancing performance magnetic materials suitable in technological applications such as spintronics, many researches have been appeared investigating the magnetic properties and phase transitions of magnetic models describing these magnetic materials [**48**].

simulations methods in this field of research are basically performed to define theoretically phase transitions that are difficult in their treatment by the usual mathematical formalisms to gate exact analytical solutions. In this thesis, as we will see, some of these technics are more accurate than others. For several years great effort has been devoted to the study of the magnetic properties and phase transitions of magnetic systems using various approximation techniques such as MFA [**37**,**47**, **49**], EFT [**50**], renormalization group [**53**], finite cluster approximation [**51**, **52**], series expansions [**54**] and MCS [**44**, **55**]. Among these technics and others, MCS is recognized to give the more accurate results very close to the ones provided by exact solutions.

Likewise, parameters like the symmetry of the system, the dimension of the space, and the exchange interaction nature between particles inside the system are some of the more important parameters that can define if the system exhibits a phase transition or not, which means that phase transitions could not be necessarily detected in all the magnetic systems. The way in which a phase transition is determined in a magnetic system is to define an order parameter that reflects the magnetic symmetry of the system. These technics involves taking in the phase above the critical point a non-zero order parameter that become equal to zero elsewhere. For the magnetic systems that exhibit a phase transition the order parameter is nothing else than the magnetization [ **37**, **47**].

### 1.2.2 Ising Model :

In this part we propose first to overview the different spin models used in domain of the statistical physics. This investigation will be followed by the discussion of the Ising model.

All of these models are depending of two factors: The degrees of the freedom and the atomic interactions. Approximately, there are three categories of spin models

- Models based on discrete spins such as Ising model [**32**, **33**] and Potts model [**34**, **35**].
- Models based on continuous spins such as the two-dimensional unit vectors XY model, the three-dimensional unit vectors of the classical Heisenberg model [**36**, **37**] and n dimensional unit vectors (n-vector model or O(n) model) [**38**].
- Models based on arrow configurations along the links of the lattice such as in Baxter's vertex models [**39**].

In this work we studying the magnetic and magnetocaloric properties when we reducing the studied systems into simple models that represent magnetic dipole moments of atomic spins that can take only two directions (up- or down-direction). Therefore, the more adequate models that can describe the magnetic properties in consideration are the ones based on discrete spins such as Ising model. That model, named after the physicist Ernst Ising, provide the basis for the study of all the systems dealt with in this thesis. The Ising model present a particular case of the well-known model, Heisenberg model, when the first one describes the spins of atomic system as dipoles that can have only two possible orientation, up or down, whereas the second allows spin vectors to point in all the directions. The Tsing model was useful to study phase transitions [**40**] of two-dimensional square-lattice that it's simple to show magnetics properties and phase transition. Ising has solved the one-dimensional Ising model in his thesis in 1924. Much later, in 1944, Lars Onsager has given an analytic description of the two-dimensional square lattice Ising model [**41**].

The transfer-matrix method is usually the method used to solve that model, but there are other methods more accurate based on approaches related to quantum field theory. In lager systems, like the complex structures of DPs, to study the phase transitions and other magnetic properties in the framework of Ising model it is indispensable to use a numerical simulation like MCS or an approximation theory like MFA or EFT.

In the Ising model, the spin is related to the Z component of operator spin S and is usually $S = \pm 1$ (1 for up and -1 for down").

The Ising Hamiltonian is given by:

$$H = -\sum_{<i,j>} J_{ij} S_i S_j - h \sum_i S_i \qquad (1.19)$$

Where:

$< i, j >$ represents the first neighbors between $S_i, S_j$ spins

$\boldsymbol{J}$ refers to the exchange coupling interactions between $S_i, S_j$ spins. the Ising model can be classified according to the sign of the exchange coupling interactions:

- $J_{ij} > 0$ , the interaction between the spins $S_i S_j$ is ferromagnetic type.
- $J_{ij} < 0$, the interaction between the spins $S_i S_j$ is antiferromagnetic type.
- $J_{ij} = 0$, there is no interaction between the spins $S_i S_j$.

So, the Ising model present a ferromagnetic order if the configuration in which nearest neighbors spins have the same direction of polarization has higher probability. Oppositely, the model is antiferromagnetic order if the majority of nearest neighbors' spins is in an antiparallel configuration.

Otherwise, the sign convention in the second term of the Hamiltonian indicate the way in which a spin $S_i$ interact with the external field. Hence, for:

- $h > 0$ , the spin $S_i$ prefers to get the positive direction of the external field.
- $h < 0$, the spin $S_i$ prefers to get the opposite direction of the external field.
- $h = 0$, the spin $S_i$ is not influenced by the external field.

According to this conventional classification, it appears that the configuration probability is the main parameter to describe the magnetic behavior of a system in the framework of Ising model. Thus, the configuration probability is given by the Boltzmann's distribution:

$$P_\beta = \frac{e^{-\beta H}}{Z_\beta} \qquad (1.20)$$

where $\beta = (k_B T)^{-1}$. $k_B$ is the Boltzmann's constant and $T$ is the temperature of the system. To simplify, it's often taken equal to one. $Z_\beta$ is the associated partition function given by:

$$Z_\beta = \sum_S e^{-\beta H} \qquad (1.21)$$

where S is the spin state and H is the energy of the system.

In the absence of an external magnetic field and when all of the nearest neighbors <ij> have the same exchange coupling strength $J_{ij} = J$, the Ising model can be simplified to:

$$H = -J \sum_{<i,j>} S_i S_j \qquad (1.22)$$

For a system with dimension $d = 1$ the transition occurs at $T = 0$. Consequently, $d = 1$ is known to be the lower critical dimension of the Ising model.

It is well known that the Ising model has a phase transition at finite temperature for systems with dimension $d > 1$.

This model indicates that in low-temperature, the spins are ordered and the value of the order parameter m (magnetization) is different to zero, whereas in the high-temperature the spins are disordered and m disappears. the Curie temperature denoted the temperature corresponding for transition from the order to the disorder if the system is basically showing a ferromagnetic order or the Neel temperature if the system is basically showing an antiferromagnetic order. Therefore, this model is the more appropriate basic model to study all order-disorder transitions in magnetic compounds.

### 1.2.3 Pillars of Monte Carlo Method

Basically, in statistical physics we define a thermodynamic quantity as an observable. The mean value of any observable quantity, such as the internal energy or the magnetization, is ideally

calculated by averaging the quantity in the phase space over all spin states of the system, which is in the canonical ensemble, denoted by:

$$< A >_{\beta} = \sum_{S} A e^{-\beta H/Z}$$

where A denote the observable, $Z$ denotes the partition function mentioned above in eq. **1.21**.

$\beta = (k_B T)^{-1}$ stands for the invers of the temperature of the system with $k_B$ is Boltzmann's constant. $H$ in eq. **1.22** is the Hamiltonian function that usually includes the interactions governing the system. These interactions may by short-ranged reflecting the nearest neighbors interactions, medium-ranged reflecting the next nearest neighbors interactions, or long-ranged for further interactions, and the summation is running over all spin states $S$ of the system. The state space is discrete in this specific case of spins, but in other cases it can be continuous.

For an Ising model, with two spin states, on a lattice of N sites, the sum is over $2^N$ configurations in the phase space. This number of states increase very quickly which make the calculation of the partition function very difficult or even more impossible to determine. In other words, the determination of the partition function for a large system ($N \rightarrow \infty$) is difficult or impossible. So, for solving this problem, it is clear from this that a different approach is required.

Monte Carlo simulation is mainly articulated on:

- Importance sampling;
- Chain Markov;
- Ergodicity;
- Detail balance;
- Acceptation probability;

In the following section, we will unveil the basic principles of Monte Carlo Method.

A. Importance sampling

The value of an observable represents the main objectives of Monte Carlo simulations. To make the process faster, the results value should be oriented towards more likely values. The average of the quantity **A** is expressed by the sum of all the states in the system and by their respective probabilities:

$$< A >_\beta = \frac{\sum_S A e^{-\beta H/Z}}{\sum_S e^{-\beta H/Z}}$$

The value of this average depends of the number of system subsets. For large system the sum on a subset of states induces inaccuracies.

Therefore, the concept of importance sampling is to create a suitable Markov chain in which the configurations are chosen according to their Boltzmann weight.

Generally, MCS uses the Markov chain to generate randomly the system configurations. Transition to a configuration noted "$b$" depends only to the previous configuration noted "$a$", but not on the whole configurations in state space. This means that the transition, which can follow the probability $W(a \to b)$, in a Markov chain is almost local in time. A Markov chain can be described as follows:

$\{\ldots \overset{W}{\to}\{S_i\}\overset{W}{\to}\{S_i\}'\overset{W}{\to}\{S_i\}''\overset{W}{\to}\ldots\}$

Where $W$ is the transition probability from a configuration "$a \equiv \{S_i\}$" to a configuration "b ≡ $\{S_i\}'$". This probability must follow the conditions given by:

$$W(\{S_i\} \to \{S_i\}') \geq 0 \; for \; all \; \{S_i\}, \{S_i\}' \qquad (1.23)$$

$$\sum_{\{S_i\}'} W(\{S_i\} \to \{S_i\}') = 1 \; for \; all \; \{S_i\} \qquad (1.24)$$

$$\sum_{\{S_i\}} W(\{S_i\} \to \{S_i\}') \, P_\beta(\{S_i\}) = P_\beta(\{S_i\}') \; for \; all \; \{S_i\}' \qquad (1.25)$$

Thus, a Markov chain is constructed by a sequence of states that satisfy the Boltzmann's probability. This succession construction process, also known as Markov process, leading to the Boltzmann's distribution is called "coming to equilibrium". Ergodicity and detail balance are

additional ideas necessary to achieve the Markov process.

B. Markov chain

The Markov chain ensure transition from A state to another b state. The difficult part is the determination of the appropriate estimator in a Monte Carlo simulation. The Monte Carlo methods use this Markov process to choose the states considered. The processes of the Markov chain are given by the equation:

$$\frac{dP(Sa,t)}{dt} = -\sum_a W(a \to b)Pa(t-1) + \sum_b W(b \to a)Pb(t-1) \quad (1.26)$$

Where,

The first term corresponds to all the possible transitions towards state **a**, while the second one represents all the possible transitions towards state **b**, W (a → b) and W (b → a) denote the transition probabilities from state **a** to **b** and vice- versa and t is the time of the Markov process.

The state generated is not always the same; it scans the system by looking for new states with the transition probability W (a → b) on which it imposes two conditions:

- Transition probability is constant with time;
- Transition probability depends on the system properties on states **a** and **b**.

This corresponds to the fact that the transition probability W (a → b) from one state **a** to another **b** of the Markov process is always constant and must satisfy the relation:

$$\sum_a W(a \to b) = 1$$

in other for better assimilate the Markov process, ergodicity and detail balance are additional ideas necessary to achieve it.

C. Ergodicity

The idea behind the ergodicity condition is that the system can, from a given state, assume any possible state after a sufficiently long time during the Markov process. The ergodicity condition is not satisfied if all the transition probabilities from a given state are zero.

D. Detail balance

The condition of detail balance ensures that the coming equilibrium of each systems are describe only by Boltzmann distribution and not another distribution. If the system is in equilibrium, the transition probabilities from a state to b state are equal:

$$\sum_a P_\beta^a W(a \to b) = \sum_b P_\beta^b W(b \to a) \qquad (1.27)$$

According to the condition $\sum_a W(a \to b) = 1$ one can obtain**:**

$$P_\beta^a = \sum_b P_\beta^b W(b \to a) \qquad (1.28)$$

For any set of transition probabilities, which satisfies the $P_\beta^a$ distribution will be the equilibrium distribution involved by the Markov process dynamics. Unfortunately satisfy this equation does not guarantee reaching the distribution $P_\beta^a$ from any system state. To demonstrate this, consider that the transition probabilities $W(a \to b)$ are the elements of the matrix $W$ (Markov matrix).

$$q_b(t+1) = \sum_a W(a \to b)\, q_a(t) \qquad (1.29)$$

In matrix notation, eq. **2.11** is given as follows:

$$Q(t+1) = W.Q(t) \qquad (1.30)$$

If the Markov process reached equilibrium:

$$Q(\infty) = W.Q(\infty) \qquad (1.31)$$

If the Markov process reached limit cycle:

$$Q(\infty) = W^n . Q(\infty) \qquad (1.32)$$

where n is the cycle size. Eq. **2.11** therefore does not guarantee the equilibrium defined by the distribution $P_\beta^a$. To overcome this difficulty, one imposes the detail balance condition given by:

$$P_\beta^a W(a \to b) = P_\beta^b W(b \to a) \qquad (1.33)$$

This condition serves to eliminate the limit cycle. When the time approaches infinity, $Q(t)$ tends exponentially towards the eigenvector corresponding to the largest eigenvalue of $W$ (stochastic matrices property). From eq. **2.13** the largest eigenvalue of Markov matrix is one.

Eq. **1.33** can be written as:

$$P = W . P \qquad (1.34)$$

At equilibrium, $Q(t)$ tends to $P$ as the time approaches infinity. Real systems satisfy the detailed balance condition.

In order to have the Boltzmann's distribution at equilibrium, an additional condition is given by:

$$\frac{W(a \to b)}{W(b \to a)} = \frac{P_\beta^b}{P_\beta^a} = e^{-\beta(E_b - E_a)} \qquad (1.35)$$

Eqs. 2.11 and 2.17 are the necessary conditions for the choice of the probability transition $W(a \to b)$. The main goal thus is to create a program that constructs the Markov chain according to the transition probabilities. The program must run long enough to ensure that $q_a(t)$ tends to the Boltzmann's distribution $P_\beta^a$ at equilibrium.

A simple choice of the transition probability is:

$$W(a \to b) \alpha\, e^{-\frac{1}{2}\beta(E_a - E_b)} \qquad (1.36)$$

But it's not a perfect choice. There are other choices that can be performed as in the case of

Metropolis algorithm.

E. Acceptation probability

Often, standard methods do not apply to new problems. New algorithms are constructed for specific needs and several Markov process can be proposed. The exact set of transition probabilities is not necessarily defined by a given algorithm. Therefore, the acceptance probability serves to find the right transition probabilities from any Markov process. In this case the condition $W(a \to a) \neq 0$ is allowed and still satisfies the detail balance. Thus, the transition probability can be given by:

$$W(a \to b) = g(a \to b)A(a \to b) \qquad (1.37)$$

where $g(a \to b)$ is the selection probability. This is the probability to get a new state "$b$" from the old state "$a$" by the algorithm. $A(a \to b)$ is the acceptance probability. This is the probability to accept the transition from the old state "$a$" to the new state "$b$". The acceptance probability value, also known as acceptance, is random between 0 and 1. If $A(a \to b) = 0$ for any transition, $W(a \to a) = 1$.

$$\frac{W(a \to b)}{W(b \to a)} = \frac{g(a \to b)A(a \to b)}{g(b \to a)A(b \to a)} \qquad (1.38)$$

In eq. **2.20**, $\frac{A(a \to b)}{A(b \to a)} \in [0, \infty[$ and so the selection probabilities $g(a \to b)$ and $g(b \to a)$ can take any possible values. In order to avoid slowness of the algorithm, we the acceptance is usually chosen close to one. The best algorithm therefore is the one that adjust the selection probability $g(a \to b)$ and takes $A(a \to b) \simeq 1$.

### 1.2.4 Metropolis algorithm:

The general Markov chain can be dealt with by many different concrete update (or single spin flip) algorithms, but the first and the most flexible update rule is well defined by the classic Metropolis algorithm [45], which is based on a simple concept enabling it to be universally

applicable. This algorithm is known for its ability to be applied in practically all cases (discrete-spins/continuous-spins, on-lattice/off-lattice, short-range/long-range interactions, etc.).

The Metropolis algorithm follows the MCS ideas defined above. This algorithm is closely related to the choice of the acceptance $A(a \to b)$. It is worth noting that there are two kinds of MCS dynamics, in the first one only one spin exhibits a flip attempt at every MCS step and in the second one all spins in the system exhibit a flip attempt at every MCS step. The second dynamic still limited by the large size of the system and the computational time that could be long in this case although it gives more accurate results than the first one. The dynamic adopted, in the case of application of that algorithm on the Ising model given in eq. 2.1, is to make a single spin flip attempt at each MCS step. In this case, all selection probabilities are equal and given by:

$$g(a \to b) = \frac{1}{N} \qquad (1.39)$$

where $N$ is the number of the spins in the system.

Detail balance equation can therefore be written as:

$$\frac{W(a \to b)}{W(b \to a)} = \frac{g(a \to b)A(a \to b)}{g(b \to a)A(b \to a)} = \frac{A(a \to b)}{A(b \to a)} = e^{-\beta(E_b - E_a)} \qquad (1.40)$$

$$A(a \to b) = A_0 e^{-\frac{1}{2}\beta(E_b - E_a)} \qquad (1.41)$$

$A_0$ is randomly determined. The largest value of $e^{-\frac{1}{2}\beta(E_b - E_a)}$ is $e^{\beta z J}$.

To ensure that $A(a \to b) \leq 1$ the value of $A_0$ is chosen to be $A_0 \leq e^{-\beta z J}$. The algorithm is more effective for large values of the acceptance $A(a \to b)$.

Metropolis algorithm with single spin flip dynamic is thus defined by the following acceptance:

$$A(a \to b) = \begin{cases} e^{-\beta(E_b - E_a)} & for\ E_b - E_a > 0 \\ 1 & elsewhere \end{cases} \qquad (1.42)$$

Therefore, transition probability $W(a \to b)$ admits the same scheme as the acceptance. With this

choice of transition probabilities, the system tends asymptotically, when the Markov chain of states approaches infinity, to a steady state in which the probability of configuration is given by $e^{-\beta E\{S\}}$.

At every MCS step, a spin flip is always accepted if it causes an energy loss. On the other hand, when the spin flip is performed and consequently the system assumes a new configuration that has a higher energy, the update has still to be accepted with a certain probability. Therefore, a uniformly distributed random number r $(0 < r < 1)$ is drown, and if $W \leq r$ , the new configuration is accepted. Otherwise the spin flip attempt is rejected, the system keeps its old configuration and a new spin flip attempt is performed for the next spin. Metropolis algorithm is practically implemented following some steps.

For the Ising model described in eq. **1.19,** in the case of no external field, the new state "b" is generated from the old state "a", the two state differs only by the single spin flip. Practically, the spin, noted *k*, to flip is selected randomly from the sites in the predefined lattice. The energy difference $E_b - E_a$, which is needed for the acceptance test, is calculated using the expression of the Hamiltonian as follows:

$$E_b - E_a = -J \sum_{<i,j>} S_i^b S_j^b + J \sum_{<i,j>} S_i^a S_j^a = -J \sum_{<i,j>} S_i^a (S_k^b - S_k^a) \qquad (1.43)$$

If $S_k^a$=1 then $S_k^a$= -1 and $S_k^b - S_k^a$= -2

if $S_k^a$= -1 then $S_k^a$= 1 and $S_k^b - S_k^a$= 2

$$S_k^b - S_k^a = -2\, S_k^a \qquad (1.44)$$

$$E_b - E_a = 2J \sum_{<i,j>} S_i^a S_k^a = 2J S_k^a \sum_{<i,j>} S_i^a \qquad (1.45)$$

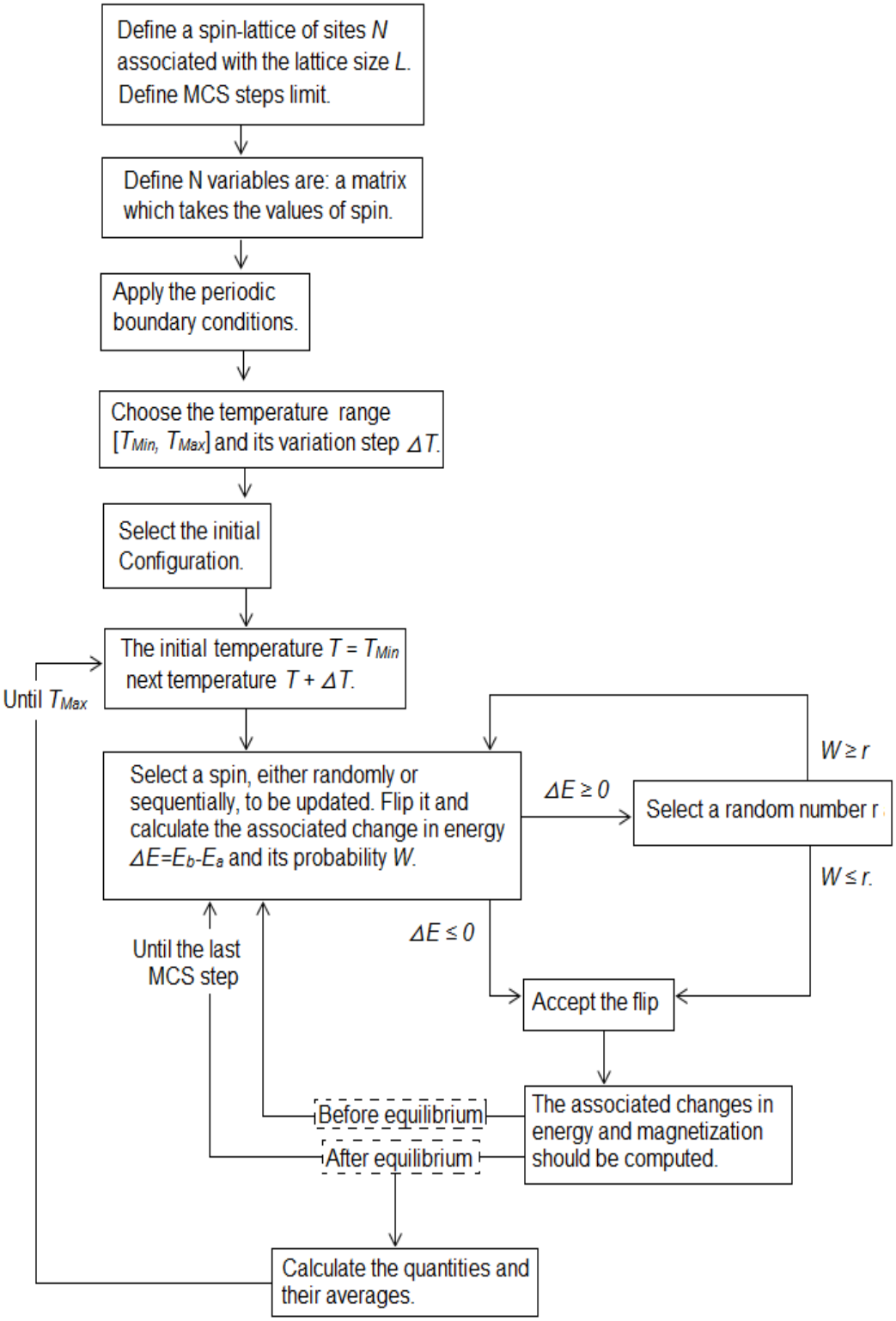


Figure 1-1: *Schematic representation of* practical implementation of Metropolis algorithm in a MCS

Some practical details should be respected during the practical implementation of Metropolis algorithm. Generally, six points require a special attention: initial configuration, select the degrees of freedom, boundary conditions, finite-size effects, random numbers, and statistical errors.

#### 1.2.4.1 Initial configuration

In principle, as noted before when discussing the transition from a state "$a \equiv \{S_i\}$" to a new state "$b \equiv \{S_i\}'$", the initial state should not, in any case, influence the new state. However, in order to reach the equilibrium faster the initial configuration should be chosen properly.

#### 1.2.4.2 Select the degrees of freedom

The degrees of freedom, which may exhibit an update, can be selected randomly or on the basis of a random permutation. However, they can follow a certain order; for instance, they can be selected by imposing a simple fixed sequential order. In some particular cases, the degrees of freedom are usually treated in such a way all even sites are updated first and then the all odd sites. The choice of the update scheme influences closely the quantitative performance, while the same scheme does not affect the qualitative behavior.

#### 1.2.4.3 Boundary conditions

Generally, one can distinguish two types of boundary conditions: periodic ones and free ones. Periodic boundary conditions are usually used for infinite systems in such a way the system is periodically repeated in all directions. While free boundary conditions are used to describe finite systems such as nanoparticles. In the case of semi-finite systems like surface systems, multi-layers systems, Nano-wire and Nano-tube systems, both boundary conditions can be used.

#### 1.2.4.4 Finite-size effects

In MCS, The lattice of a system is considered as a numerical tool that still limited by the computer capacity. Therefore, the size of the lattice must be defined properly and carefully to well mimic the macroscopic properties of the infinite system. Thus, the limit of L, above which the physical quantities do not change, is known as the thermodynamic limit. In order to define this limit, usually, an average for several different lattice sizes is calculated and then extrapolated to infinite L.

#### 1.2.4.5 Random numbers

Random numbers, in MCS code, are recovered by the usual random number generators (RNGs), which generate a sequence of numbers that cannot be reasonably predicted well than by a random chance. PRN generation is an important and common task in computer programming. The performance of a RNG is measured according to several points such as the difficulty to derive the deterministic rule on the basis of which the RNG is constructed, a very long period and the absence of any kind of correlations. Most computer programming languages include functions or library routines that provide RNGs. They are often designed to provide a random byte or word, or a floating point number uniformly distributed between 0 and 1. The default random number generator in many languages is based on the Mersenne Twister [**56**] algorithm that is explicitly stated in the language documentation. When choosing a RNG, it is always recommended to rely only on well-tested and well-documented RNG to avoid all kind of errors that can affect the results.

#### 1.2.4.6 Statistical errors

The first detail that must be fixed is the large number of MCS steps, which, like the size of lattice, still also limited by the computer capacity. At a certain MCS step, the equilibrium is reached and so the measurements can be performed and the averages in consideration can be calculated from this step until the last MCS step. Therefore, the MCS step that defines the beginning of equilibrium must be determined carefully to avoid the effect of statistical errors that

become larger near the critical point due to the critical slowing down at second order phase transitions and the problem of tunneling out of metastable states at first order phase transitions.

### 1.2.5 Equilibrium and measurements:

Simulation program must run sufficiently long time to reach the equilibrium. The time in this case is defined by MCS steps. After equilibrium one calculates on a new period the estimation of the physical quantities averages of interest. In order to determine the MCS step at equilibrium, the evolution of a quantity is followed such as the magnetization or the internal energy, which shows that the quantity firstly changes and then stabilizes at the equilibrium to display only fluctuations. In some cases, the system remains trapped in a local energy minimum. To avoid this, start from different initial configurations is recommended.

For the Ising model described in eq. **2.1** one can compute some interesting quantities such as the magnetization, the magnetic susceptibility and the specific heat that are given respectively by:

$$M = \frac{1}{N}\sum_{i=1}^{N} S_i \qquad (1.46)$$

$$\chi = \beta N(\langle M^2\rangle - \langle M\rangle^2) \qquad (1.47)$$

$$C_v = \frac{\beta^2}{N}(\langle E^2\rangle - \langle E\rangle^2) \qquad (1.48)$$

Where N represent the total number of spins in the system.

For real materials, it should be noted that, in the Hamiltonian, the exchange interaction couplings and other terms such as the crystal fields are usually determined first either by experimental or theoretical means. But in most cases, as in the case of DPs studied in this thesis, the material in consideration is so new that parameters like couplings and crystal fields are still not determined either experimentally or theoretically. Therefore, the magnetic properties are studied according to reduced parameters instead of real parameters. In this work all parameters are reduced to the same exchange coupling $J_1$ [**57**] that will be presented in the next chapter.

Finally, it's also worth noting that, heat-bath and Glauber algorithms are in the same class of algorithms as Metropolis known as single-spin-flip or local-update algorithms that are also widely used as well as Metropolis algorithm [**57**].

On the other hand, cluster algorithms or non-local-update algorithms, stepping beyond local-update algorithms, are another class of algorithms that are also developed to simulate physical systems especially in the framework of MCS. This class of algorithms was developed mainly to solve the problems affecting the local-update algorithms such as the problem of critical slowing down at second order phase transitions and the problem of tunneling out of metastable states at first order phase transitions. Among algorithms belonging to this class, the most well-known are wolf algorithm [**58**] and Swendsen-Wang algorithm [**59**]. Choosing a local-update algorithm or a non-local-update algorithm depends closely on the physics of the problem to solve.

# Part 2: magnetic compound in potential application: spintronic and magnetic refrigeration

## 2.1 Spintronic

### 2.1.1 Introduction

Recently, a technology has emerged called spintronic (spin transport electronics or spin based

electronics), based on the information storage in memories applications. This technology offers many features to include in new generation of devices associating spin dependent effect with standard microelectronic due to thanks to interaction between spin and magnetic properties of the material.

The principle of the spintronic is depending on the spin alignment (either up or down) in other words is to have the clockwise rotation or in the inverse sense, depending of applied magnetic field.

The advantages of the spintronic, are increasing data and optimize the speed, also would be increase the densities compared with conventional semiconductor, and decreased electric power consumption. As well as, the optimization of electron spin lifetimes, the detection of spin coherence in nanoscale structures, transport of spin-polarized carriers across relevant length scales.

Electronics and magnetics lead to novel spin-based devices such as spin-LED (light-emitting diode), spin-FET (field effect transistor), spin RTD (resonant tunneling device), optical switches operating at terahertz frequency, encoders, decoders modulators, and quantum bits for quantum computation and communication. Although if we can control spin degree of freedom in the semiconductors, semiconductor heterostructures and ferromagnets, we can enhance the performance and features of spin-based devices.

### 2.1.2 Giant magnetoresistance

Since 1980 the giant magnetoresistance effect (GMR) was discovered by two scientists Peter Gruenberg and Albert Fert, they concluded very values resistance changes in materials comprised of alternating very thin layers of various metallic elements (Figure 0-1).
These experiments are obtained at low temperatures and in the presence of very high magnetic fields, the magnitude of this discovery reflect the interest and power of the Giant Magneto resistive effect applications [61-62].

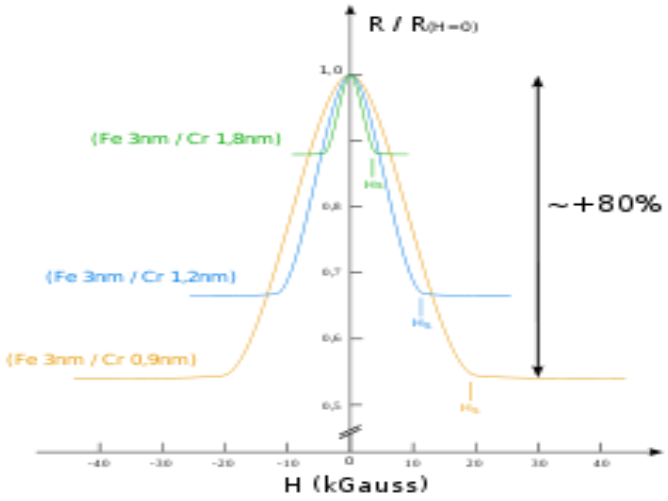


Figure 0-1: The founding results of Albert Fert and Peter Grünberg, the variation of the resistance of the GMR as a function of chromium [63].

The GMR effect is the variation of electrical resistance in response to an applied magnetic field, the transition metals present a favorite material in this field and many studies was elaborated. [64-86]
Connected to transition metals the applied external magnetic field to Fe/Cr multilayer brought to significant reduction of electrical resistance of multilayer. This effect was found to be much larger than either ordinary or anisotropic magnetoresistance and was, therefore, called “giant magnetoresistance” or GMR. Likewise, high magnetoresistance is discovered in Fe/Cu multilayers. The change in the resistance of the multilayer occurred when the applied field aligns the magnetic moments of the successive ferromagnetic layers, as is illustrated schematically in Figure 0-2 In the zero magnetic field the magnetizations of the ferromagnetic layers are antiparallel. Applying the magnetic field, which saturates the magnetization and aligns the

magnetic moments of the multilayer, leads to a drop in the electrical resistance of the multilayer [61-63].

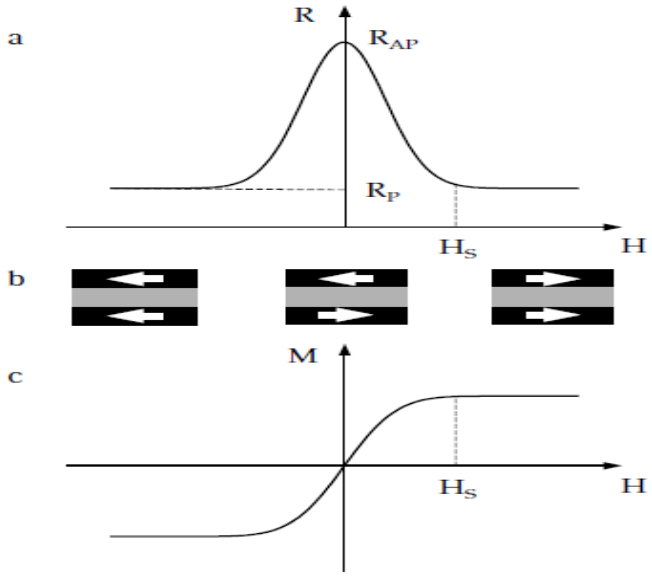


Figure 0-2: Schematic representation of the GMR effect. (a): Change in the resistance of the magnetic multilayer as a function of applied magnetic field. (b): The magnetization configurations (indicated by the arrows) of the multilayer (trilayer) at various magnetic fields: the magnetizations are aligned antiparallel at zero field; the magnetizations are aligned parallel when the external magnetic field H is larger than the saturation field $H_S$. (c): The magnetization curve for the multilayer [63].

### 2.1.3 Origin of GMR

GMR can be understood by the Mott model, which was introduced in 1936 to explain the sudden increase in resistivity of ferromagnetic metals as they are heated above the Curie temperature. There are two principal pillars proposed by Mott [61-63]:

- The electrical conductivity of metals depended of conducting channel correspond to the spin (-up and -down) electrons. In fact, the probability of spin flip scattering processes in metals are small as compared with to the probability of the scattering processes in which the spin is conserved. This prove that the (-up and -down) spin electrons do not merged over long distances and, therefore, the electrical conduction arise in parallel for the two spin channels [61-63].

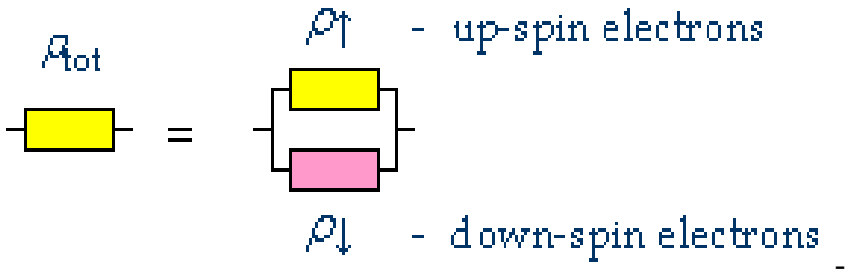


- the scattering rates of the (-up and -down) spin electrons are different regardless of the nature of the scattering. The electronic band structure in a ferromagnet metals has exchange splitting, consequently the density of states is not symmetry for (-up and -down) spin electrons at the Fermi energy. Scattering rates are proportional to the density of states, so the resistivities and scattering rates are different for electrons of different spin.

$$\rho_{\uparrow} \neq \rho_{\downarrow}$$

Based on Mott's theoretical, the scattering is strong for antiparallel spin electron with magnetic field direction, and is weak for parallel spin electron with magnetic field direction. The up-spin electrons pass cross the structure within scattering for the parallel-aligned magnetic layers, because their spin is parallel to magnetic field of the magnetization layers. On the contrary, the down-spin electrons are scattered strongly within both ferromagnetic layers, because their spin is antiparallel to the magnetization of the layers. Since conduction are present in parallel for the two spin channels, the total resistivity of the multilayer is result to the highly-conductive up-spin electrons and appears to be low. For the antiparallel-aligned multilayer, both the up-spin and down-spin electrons are scattered strongly within one of the ferromagnetic layers, because within the one of the layers the spin is antiparallel to the magnetization direction. Therefore, in this case the total resistivity of the multilayer is intense Figure 0-3.

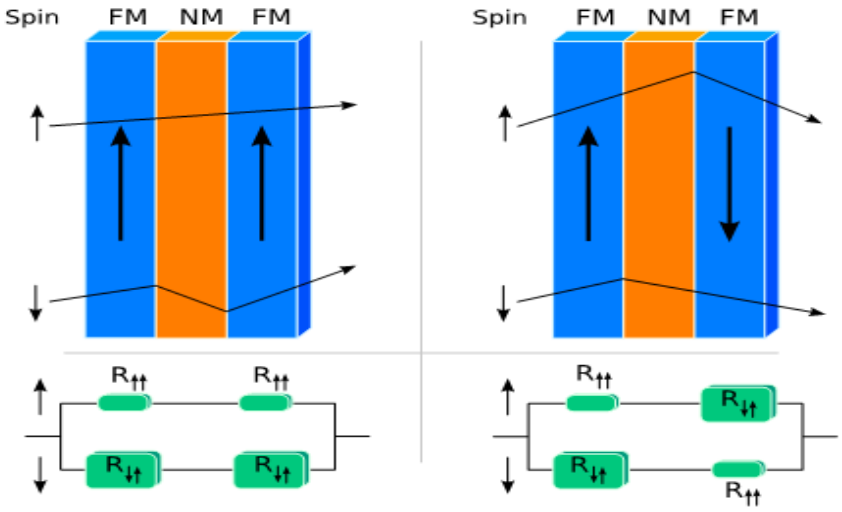


Figure 0-3: The operating principle of the GMR [67]. Depending on whether the two magnetic layers are polarized in the same direction (left) or in opposite direction (right). The total resistance of the stack of layers is different.

### 2.1.4 Magnetic Tunnel Junction

Magnetic tunnel junctions or MTJs are nanostructured devices used in the field of spintronic. The discovery of giant magnetoresistance in multilayered ferromagnetic films separated by thin insulator spacers has present a vast research interest, particularly also for a many of potential applications, e.g., in data-storage devices. To enhancing these developments and earlier efforts in tunneling devices, Moodera et al. [87]

have discovered that the tunneling current between two ferromagnetic films separated by a thin oxide layer strongly depends on an external magnetic field, this effect known as tunnel magnetoresistance (TMR). Since then, the impact of MTJs on the field of spintronics has extremely winded, particularly due to the enormous magnitude of the observed magnetoresistances at room temperature and its impact on potential applications [88].

### 2.1.5 Basic principle of MTJs

The passage of electrons when flowing across two ferromagnetic metals separated by isolated barrier, presented an effect of magnitude current depends of magnetization orientation of both electrodes see Figure 0-4 some arguments are listed below to understood this effect:

- The tunneling current depend effectively of the electrode density of states (DOS) at the Fermi level.

- the ground-state energy bands in the vicinity of the Fermi level are shifted in energy in ferromagnetic materials, yielding separate majority and minority bands for electrons with opposite spins
- the spin of the electron is preserved during tunnel transportation.

As a result of these aspects, the current between electrodes with the same magnetization direction should be higher than those with opposite magnetization (see Figure 0-4).

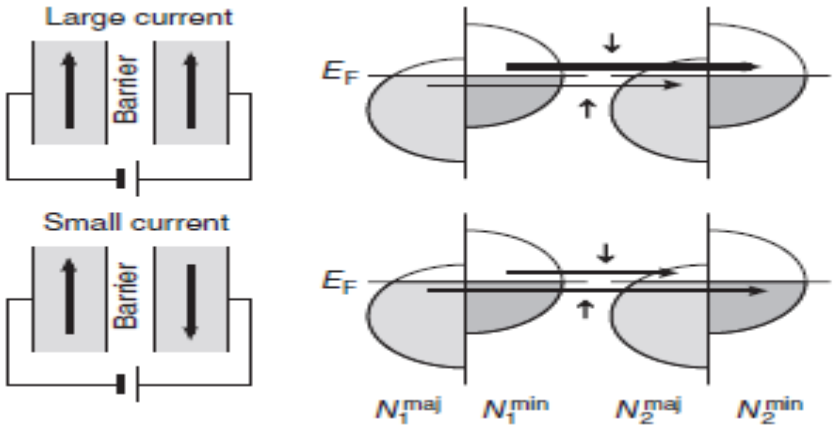


Figure 0-4: Schematic illustration showing the mechanism of TMR.

For the parallel aligned magnetization as plotted at left, electrons around the Fermi level with spin up and spin down are allowed to tunnel from majority to majority bands, and from minority to minority bands.

For the antiparallel magnetization, the tunneling takes place from majority to minority and minority to majority bands, leading to a reduction of total tunneling current. In terms of electrical

resistance, this corresponds to a higher resistance when the magnetization of the two layers is oppositely aligned.

From this simple model, the change in resistance between antiparallel and parallel magnetization (normalized to the parallel resistance) is given by:

$$\mathrm{TMR} = \frac{R_{\uparrow\downarrow} - R_{\uparrow\uparrow}}{R_{\uparrow\uparrow}} = \frac{G_P - G_{AP}}{G_{AP}} = \frac{\left(n_1^{\uparrow} n_2^{\uparrow} + n_1^{\downarrow} n_2^{\downarrow}\right) - \left(n_1^{\uparrow} n_2^{\downarrow} + n_1^{\downarrow} n_2^{\uparrow}\right)}{n_1^{\uparrow} n_2^{\downarrow} + n_1^{\downarrow} n_2^{\uparrow}} = \frac{2P_1P_2}{1 - P_1P_2}$$

Where G is the electrical conduction of the junction, and $G_P$ is related to parallel magnetization configuration and $G_{AP}$ is connected to anti-parallel magnetization configuration.

For n, the $n_i^{\uparrow}$ and $n_i^{\downarrow}$ (where i = 1 or 2) are the densities of states of majority and minority spin electrons in each electrode, and $P_j$ (where j = 1 or 2) is the polarization of the current in each of the electrodes at the Fermi level. This quantity is dimensionless and we frequently use percentage.

### 2.1.6 The magnetic random-access memories MRAM

Magnetoresistive Random Access Memory (MRAM) is different from conventional types of memory like SRAM, DRAM, and Flash, where electric charge is used to store information. Instead of exploiting the *charge* of an electron, MRAM uses its *spin* to store data.

At the heart of MRAM's spintronic nature is the magnetic tunnel junction (MTJ), a thin-film structure comprised of many ferromagnetic and nonmagnetic layers. The resistance of the MTJ, and therefore bit state of the memory element, switches purely with the change in polarization of these layers. Since these materials can hold their polarization virtually forever when unpowered, MRAM therefore falls into the nonvolatile memory (NVM) camp, along with Flash, Fe RAM, and EEPROM. To system designers in the 1960s and 70s, when semiconductor memories where relatively new, the standard way of thinking was "look to *volatile* memories when speed and density are important but power is not" and "look to *nonvolatile* memories when power is important but density and speed are not." These were simple rules that held true for the

technologies available at the time like DRAM, SRAM, and EEPROM. However, today's memory landscape includes so many technologies that making such a strict distinction is no longer possible. Each type of memory has a unique set of advantages and disadvantages, and there are "ideal memory" candidates that promise to combine the strengths of many technologies

without the weaknesses. One such candidate is the next generation of MRAM, based on spin-torque technology, known as ST-MRAM. It promises to combine the nonvolatility of Flash, the density of DRAM, the speed of SRAM, and radiation-hardness of MRAM. [89]

The MRAM architecture presents a magnetic tunnel junction connected in series with a transistor selector, Figure 0-5, a bit line and a word line. Writing is performed by closing the transistor and passing a current through the bit line and the word line that cross at the addressed memory location. This fact creates two orthogonal magnetic fields at the junction. These two fields are able to change the direction of the free layer. Each magnetic field taken independently, does not allow the reversal of the magnetization of the free layer because the magnetic field created at the intersection of the two currents must be greater than the coercively of the free layer.

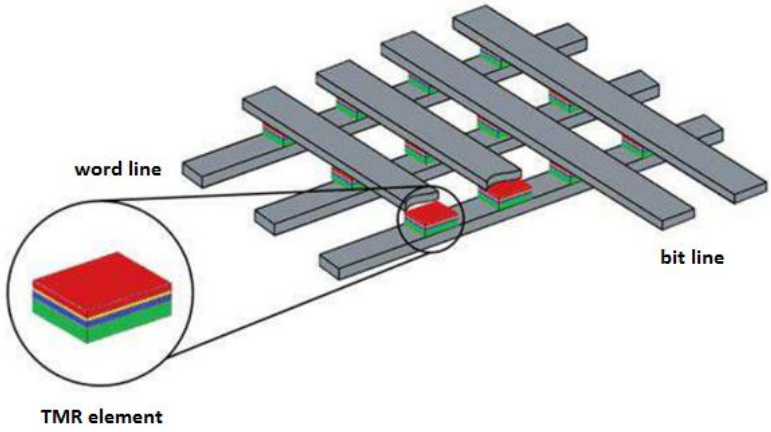


Figure 0-5: MRAM architecture formed by a matrix of magnetic tunnel junctions [90]

## 2.2 Magnetization

### 2.2.1 Introduction

the name of magnetism dates back to 600 BC when a shepherd, called Magnes, discovered magnets. The shepherd lived in a region named Magnesia near Ida Mount (literally Mountain of the Goddess) in Greece.

Zheng Gongliang in 1064, conclude that iron could acquire a thermoremanent magnetization when quenched from red heat.

In 1819 Oerstead fortuity made the connection between magnetism and electricity, discovering that a current carrying wire deflected a compass needle.

Michael Faraday's intuition that the electric and magnetic forces could be conceived in terms of all-pervading fields was critical. He discovered electromagnetic induction (1821) and demonstrated the principle of the electric motor with a steel magnet, a current-carrying wire and a dish of mercury.

Later, in 1906, Weiss proposed the ferromagnetic theory. During 1920's, the physics of magnetism was developed with theories involving electron spins and exchange interactions.

A magnetic field is produced whenever an electrical charge is in motion, although the motion of an electron give rise of:

- magnetic dipole moment
- magnetic field
- current loop

The magnetic moments associated with atoms have three origins:

1 The electron orbital motion.
2 The change in orbital motion caused by an external magnetic field.
3 The spin of the electrons.

When a material is placed within a magnetic field, the material's electrons will be affected. However, materials can react quite differently to the presence of an external magnetic field. This reaction is dependent on a number of factors such as the atomic and molecular structure of the

material, and the net magnetic field associated with the atoms. In most atoms, electrons occur in pairs. Each electron in a pair spins in the opposite direction, so when electrons are paired together, their opposite spins cause their magnetic fields to cancel each other. Therefore, no net magnetic field exists. Alternately, materials with some unpaired electrons will have a net magnetic field and will react more to an external field.

Most materials can be classified as **ferromagnetic**, antiferromagnetic, 60erromagnetic, **diamagnetic** or **paramagnetic** these stats related to the magnetic grandeur, the B, H and M fields

Where:

$$\vec{B} = \mu_o (1 + \chi_m)\vec{H} \qquad \vec{M} = \chi_m \vec{H} \qquad \mu = \mu_o (1 + \chi_m)$$

### 1.2.6 different magnetic materials

A. Diamagnetic materials $\chi_m < 0$

A material is called diamagnetic when the generated magnetization is in the opposite direction to that of the applied magnetic field and it is lost immediately after the removal of the external magnetic field. The diamagnetic substances are formed by the atoms which have no net magnetic moments. However, these are characterized by:

- the negative susceptibility (X=-10-5) [92-93]
- Slightly repelled by a magnetic field.
- Do not retain the magnetic properties when the external field is removed.
- Magnetic moment – opposite direction to applied magnetic field.
- Solids with all electrons in pairs – no permanent magnetic moment per atom.
- Properties arise from the alignment of the electron orbits under the influence of an external magnetic field.

- Most elements in the periodic table, including copper, silver, and gold, are diamagnetic.

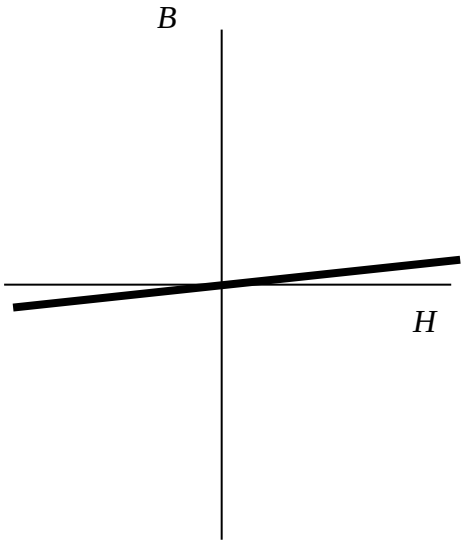


Diamagnetic material

$\chi_m < 0$ (small)

$B = \mu_o (1+ \chi_m) H$

Permeability

$\mu = \mu_o (1+ \chi_m)$ =slope of *B-H* line

B. Paramagnetic materials $\chi_m > 0$ *small*

In this class of material, some of the atoms in the material have a net magnetic moment due to incomplete electron orbitals. But there is no interaction between these atomic magnets. This material order is characterized by a magnetic moment that follows the direction of the applied field and also the magnetization is null when the applied field is removed. Paramagnetic minerals have positive susceptibility ($10^{-2}$-$10^{-4}$) [91-93].

Some properties of paramagnetic materials:

- Small and positive susceptibility.
- Slightly attracted by a magnetic field.
- Material does not retain the magnetic properties when the external field is removed.
- Properties are due to the presence of some unpaired electrons and from the alignment of the electron orbits caused by the external magnetic field.
- Examples – magnesium, molybdenum, lithium, and tantalum.

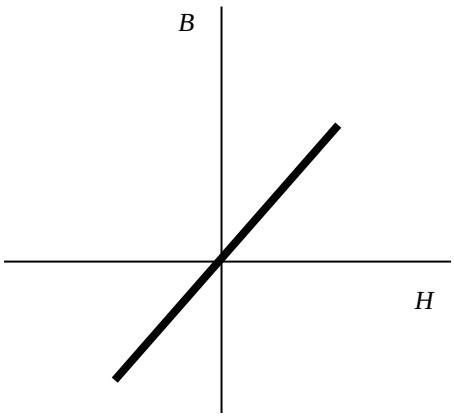


Ideal magnetic material
or paramagnetic material
$\chi_m > 0$ (small)

$B = \mu_o \mu_r H = \mu H$

$\mu$ = constant = slope of B-H curve

0. Ferromagnetic materials

Some materials with strong positive susceptibility can also carry strong remanence magnetization (magnetization that remains after the applied field is removed). This class of materials is known as ferromagnetic order. The latter has a spontaneous magnetic moment and also it is a characteristic of materials in which the magnetic direction and the applied field one is in the same direction and maintain their magnetic moment alignment parallel after the disappearance of this field. In these, substances exhibit very strong magnetism [100].

This phenomenon is restricted to transition and rare-earth elements indicates that it is related to the unfilled 3d and 4f shells in these substances.

The ferromagnetic materials characterized by:

- Large and positive susceptibility.
- Strong attraction to magnetic fields.
- Retain their magnetic properties after the external field has been removed.
- Some unpaired electrons so their atoms have a net magnetic moment.
- Strong magnetic properties due to the presence of magnetic domains. In these domains, large numbers of atomic moments ($10^{12}$ to $10^{15}$) are aligned parallel so that the magnetic force within the domain is strong. When a ferromagnetic material is in the un-magnetized state, the domains are nearly randomly organized and the net magnetic field for the part as a whole is zero. When a magnetizing force is applied, the domains become aligned to

produce a strong magnetic field within the part.

- Iron, nickel, and cobalt are examples of ferromagnetic materials.
- $\vec{B} = \mu_o (\vec{H} + \vec{M})$ Magnetization is not proportional to the applied field.
- $\chi_m$(ferrite) ~ 100 $\chi_m$(iron) ~ 1000

0. Superparamagnetism

Superparamagnetism is a type of magnetism that can appear in Nano-ferromagnetic or Nano-ferrimagnetic particles and consists of single magnetic domains. The coercivity and remanence magnetization of superparamagnetic materials are often equal to 0 or very close to 0. In addition, the superparamagnetic materials show a paramagnetic behavior below their critical temperature where the thermal agitations are not strong enough. The interaction forces between the individual atoms dominates the thermal agitations. But the thermal agitations succeed in changing the direction of the magnetization of the entire particle. As a result, the directions of the magnetic moments of the particles in the crystal are randomly arranged. Thus, the net magnetic moment is zero [94-95].

E. Antiferromagnetism

The magnetic structure similar to that of the ferromagnetic materials but is composed of two magnetic sublattices referred as **A** and **B**. The exchange interaction between neighboring atoms leads to the anti-parallel alignment of the atomic magnetic moments and also the exchange coupling is negative. Hence, the resultant magnetic moment is null when the magnetic moments are equal, they cancel each other [95-96].

In the antiferromagnetic order, we find several types which are illustrated in the table below

| Magnetic order type | Relative spin directions | Theoretical surface spin structures (unreconstructed) | | |
|---|---|---|---|---|
| A | 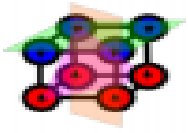 | 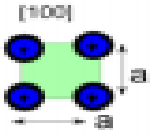  | 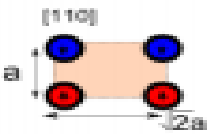  | 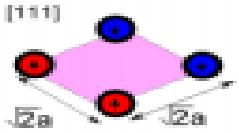  |
| B | 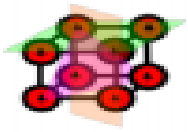 | 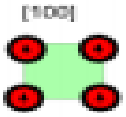  | 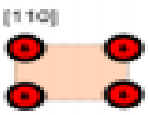  | 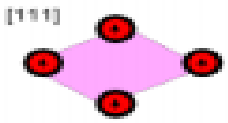  |
| C | 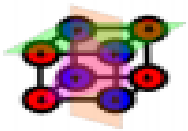 | 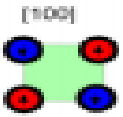  | 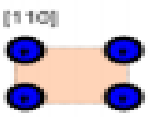  | 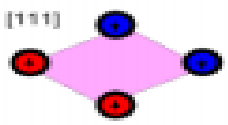  |
| D | 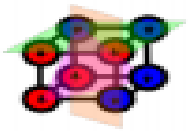 | 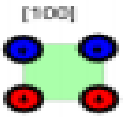  | 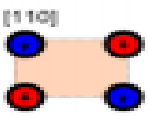  | 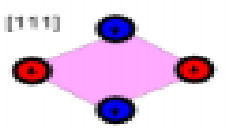  |
| E | 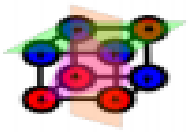 | 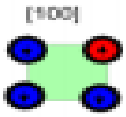  | 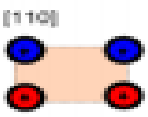  | 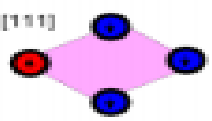  |
| F | 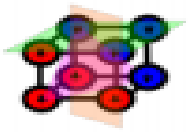 | 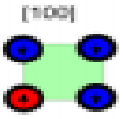  | 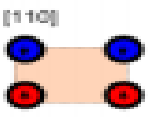  | 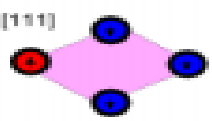  |
| G | 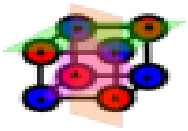 | 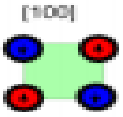  | 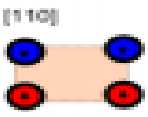  | 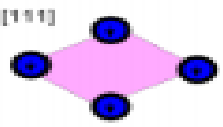  |

Tableau 1: Possible types of antiferromagnetic order, their theoretical surface spin structures with the blue atoms(spin down) and the red atoms (spin up), labeled in the conventional way according to nomenclature introduced in Ref.[97]

Connected to this table we have six types of anti-ferromagnetic orders (A, C, D, E, F and G):

- **A-Antiferromagnetic:** called super anti ferromagnetic order which corresponds to the ferromagnetic order of the magnetic atom in the basal planes (a, b) and antiferromagnetic order of these atom between these planes along c.
- **C-Antiferromagnetic:** which corresponds to the antiferromagnetic order in the basal planes (a, b) and ferromagnetic order along the c axis.
- **G-Antiferromagnetic:** which corresponds to the antiferromagnetic order of the magnetic atom in the basal planes (a, b) and antiferromagnetic order of these atom between these planes along c axis.

F. Ferrimagnetism

This order of materials occurred in complex crystal structure, there can be incomplete cancellation of antiferromagnetic arranged spin with sublattice A and B giving a net magnetic moment. The strongest interactions result in an antiparallel alignment of spins between the **A** and **B** sub- lattices [93-96].

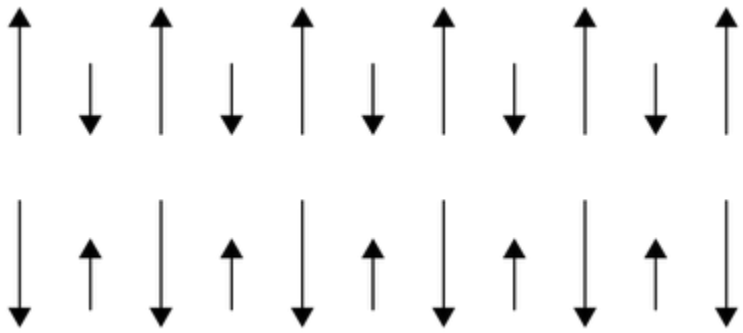

Figure 0-6: Alignment of spin moments in the ferromagnetic materials

### 2.2.2 phase transition and critical temperature

A. Curie-Weiss temperature

Ferromagnetism appears only below a certain temperature, which is known as the ferromagnetic transition temperature or simply as the Curie temperature, this temperature depends of substance. Above the Curie temperature, the moments are oriented randomly, resulting in a zero net magnetization. In this region the substance is paramagnetic, and its susceptibility is given by:

$$x = \frac{C}{T - T_c}$$

which is the Curie-Weiss law. The constant C is called the Curie constant and $T_C$ is the Curie temperature. The Curie temperature is an essential temperature for a ferromagnetic material [98]

C. Néel temperature

In an antiferromagnet which both sublattices *A* and B have equal saturation magnetizations and the spins are ordered in an antiparallel arrangement with zero net moment at temperatures below the ordering temperature which is called the Néel temperature, this temperature which distinguishes between the antiferromagnetic state and the paramagnetic one [99-100].

The susceptibility in the paramagnetic region behaves in a different fashion.

$$x = \frac{2C}{T + T_c}$$

Where C refer to a single sublattice.

D. Compensation Temperature

The compensation temperature $\mathbf{T_{comp}}$ characterizes 66erromagnetic materials when the total magnetization of the system disappears at $\mathbf{T_{comp}}$ below the critical temperature. It appears due to the nature of the exchange interaction between the two unequal moments of sub-lattices **A** and **B**

which form the 67erromagnetic material. At the compensation temperature, the magnetic moments of the two sub-lattices are antiparallel and have the same absolute value of the magnetic moment [101-102]. At $T_{comp}$ the magnetic moment of each sublattices are equal and opposite.

### 2.2.3 Crystal field theory

One of the main features of transition metal oxides, which makes them difficult to describe theoretically, is the strong localization of their 3d-electrons. This theory [103] used as a model to describe the breaking of degeneracy (the same energy of electron orbital states (d or f orbitals)) caused by a static electric field.

The crystal field theory (CFT), being a perturbation theory, may be used in different ways. One particular realization is based on the assumption about the influence of spin-orbit coupling (SOC) and field of ligands (LF) on the system. The CFT theory describes the following systems:

- Free ion without SOC (spherical symmetry, gas phase)
- Ion with SOC
- Ion with SOC placed in the field of ligands (strong SOC, weak LF)
- Ion surrounded by ligands
- Ion surrounded by ligands with SOC (strong LF, weak SOC)

A. Octahedral crystal field

The Octahedral Crystal Field present the most common type of complex. In this, six ligands form an octahedron around the metal ion. The d-orbital contains 2 levels with energy difference, **Δoct,** in the octahedral symmetry. **Δoct** (crystal-field splitting) is where the $d_{xy}$, $d_{xz}$ and $d_{yz}$ orbitals have lower energy refer as ($e_g$) and the $dz^2$ and $dx^2$-$y^2$ orbitals have higher energy refer as ($t_{2g}$). The typical orbital energy diagrams are as follows:

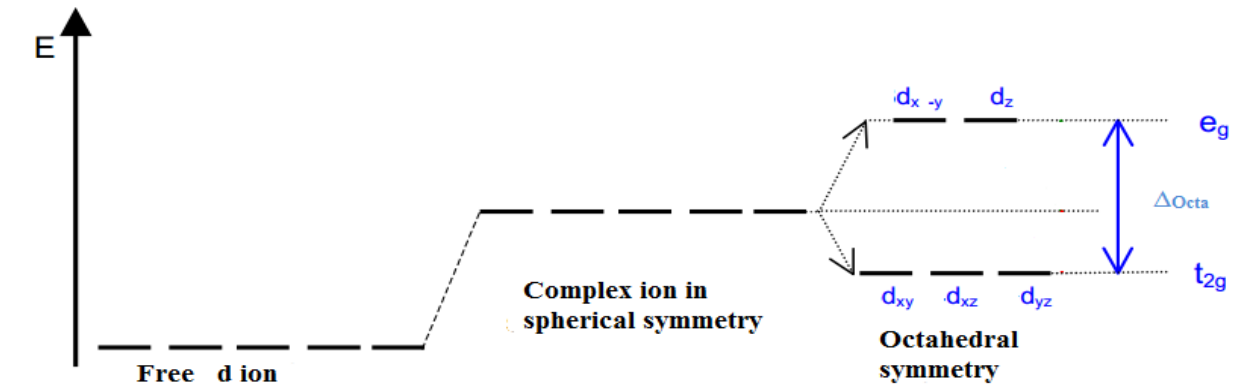


Figure 0-7: Octahedral crystal field effect on d orbitals energy level

B. Tetrahedral crystal field

The crystal field splitting in the tetrahedral field $\Delta_t$ is intrinsically smaller than in the octahedral field. The relationship with $\Delta_{oct}$ and $\Delta_t$ may be present as: $\Delta_t = 4/9\ \Delta_{oct}$

The energy diagrams of both crystal field are as follows:

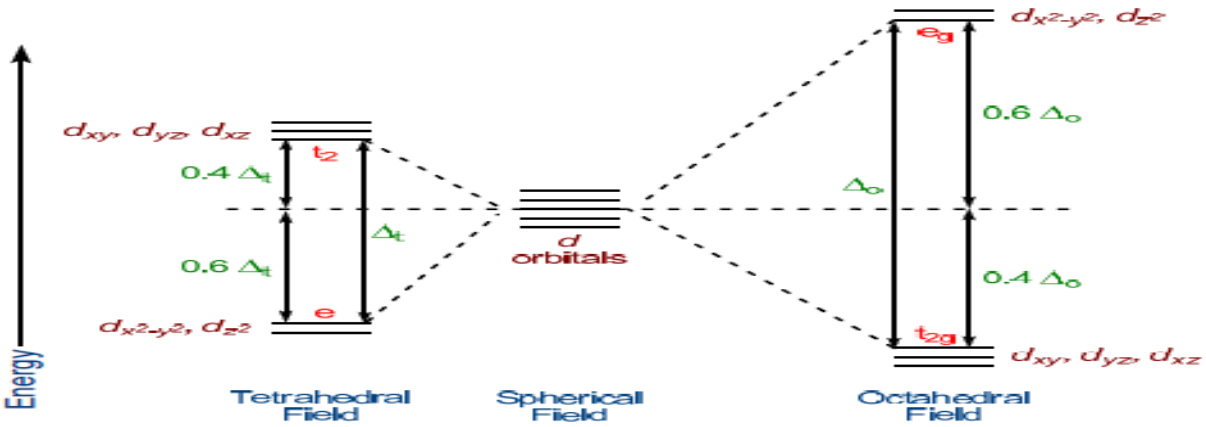


Figure 0-8: Octahedral and tetrahedral crystal fields' effect on d orbitals energy level

### 2.2.4 hysteresis loop

When a ferromagnetic material is magnetized in one direction, it will not relax back to zero magnetization when the imposed magnetizing field is removed. It must be driven back to zero by

a field in the opposite direction. If an alternating magnetic field is applied to the material, its magnetization will trace out a loop called a hysteresis loop. The lack of retraceability of the magnetization curve is the property called hysteresis and it is related to the existence of magnetic domains in the material. Once the magnetic domains are reoriented, it takes some energy to turn them back again.

In the following section, we will briefly define the four characteristic parameters of the hysteresis cycle [94].

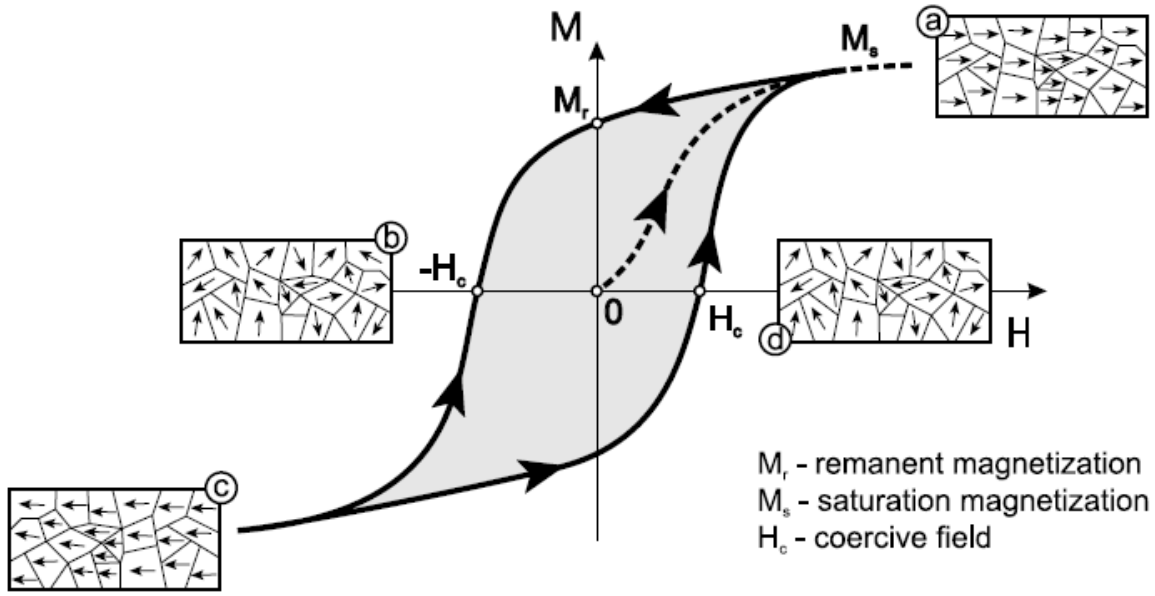


Figure 0-9: The magnetization 'M' vs magnetic field strength 'H' for a ferromagnetic:

(d) starting at zero the material follows at first a non-linear magnetization curve and reaches the saturation level, when all the magnetic domains are aligned with the direction of a field; when afterwards driving magnetic field drops to zero, the ferromagnetic material retains a

considerable degree of magnetization or "remember" the previous state of magnetization;

(b) at this point, when H = 0 a ferromagnet is not fully demagnetized and only the partial domain reorientation happened;

© saturation level in the opposite direction of applied field;

(d) in order to demagnetize a ferromagnetic material, the strong magnetic field of the opposite direction (called \coercive field, `Hc') has to be applied.

The magnetic hysteresis loop above shows the behavior of ferromagnetic materials as a function of the external magnetic field. Also, it presents the four characteristic parameters of the hysteresis cycle.

- Saturation field (Hs)

The saturation field is the minimum value of the external magnetic field to reach the saturation magnetization.

- Saturation magnetization ( Ms)

The saturation magnetization is a state reached when an increase in applied external magnetic field H cannot increase the magnetization of the material further.

- Remanence magnetization (Mr)

The remanence magnetization is the magnetization that remains after the external magnetic field is removed.

- Coercive field (Hc)

The coercive field (Hc) corresponds to the value of the field to be applied for demagnetizing a material.

### 2.2.5 magnetic anisotropy

The ferromagnetic materials are subdivided into many small sub-volumes, called domains. Each domain is spontaneously magnetized to saturation, but the direction of magnetization varies from domain to domain. The net vector sum of all the domains therefore produce a total magnetization of near zero. It wasn't until the 1930's that domains were experimentally confirmed. This

variation of direction of magnetization is known as magnetic anisotropy [104-105]

the magnetic anisotropy due to two sources:

- Dipolar interaction is a long-range order interaction and relies on the form of the sample. From this dipolar interaction, it can be illustrated, for a thin film, that the anisotropy energy contribution diminishes to

$$E_d = \frac{1}{2}\mu_0 M_s^2 cos^2(\theta)$$

  Where, Ms is the saturation magnetization and $\theta$ is the angle between the magnetization and the film normal.
- The spin orbit interaction gives the description of the coupling exchange between the electrons spin and their orbital motion.

## 2.3 Magnetocaloric effect

### 2.3.1 Introduction

The magneto caloric effect was discovered by Warburg in 1880, when he observed it in Iron [106]

This scientist observed that when iron was placed in a magnetic field, it was immediately heated,

and the iron sample cooled down when the magnetic field was removed with the cooling varying between 0.5 to 2K/T.

In 1976 Brown evince that the refrigeration could work at the ambient temperature by generating a temperature different of 47 k with a ferromagnetic refrigerant [107].

In 1997, Prof. Karl A. Gschneiger, who worked at the Laboratory of Astronautics of America, aptly discovered the concept "magnetic refrigeration" by demonstrating that magnetic refrigeration competes with gas compression cooling [108]. In 2001, Astronautics Corporation invented the world's first successful room temperature magnetic refrigerator in which permanent magnets were used to generate the magnetic field [9].

### 2.3.2 Magnetocaloric effect

The processes and origin of magneto caloric effect was interpret and explain by Debye [110] and Giauque [111]. They also suggested the first practical use of the MCE it could be realized through two fundamental thermodynamic processes (adiabatic and isotherm)

The isothermal magnetization of a paramagnet or a soft ferrimagnet (we apply H and the magnetic entropy decreases), while the adiabatic demagnetization (we remove H, the total entropy remains constant and temperature decreases since the magnetic entropy increases) see Figure 0-10.

The value of the entropy of a ferrimagnet (FM) at constant pressure depends on both H and temperature T, whose contributions are the lattice (S lat) and electronic (S el) entropies, as for any solid, and the magnetic entropy (S m)

$$S(H,T) = S_m(H,T) + S_{el}(H,T) + S_{lat}(H,T) \quad (1.1)$$

In Figure 0-11 shows a diagram of the entropy variation in vicinity of curie temperature Tc versus temperature T. The total entropy is plotted for both applied external field, $H_1$, and for zero field, $H_0$. The magnetic entropy is also shown for each case ($H_1$ and $H_0$). Two relevant processes are shown in the diagram in order to understand the thermodynamics of the MCE:

- Adiabatic process: when applied external field the magnetic entropy decreases, but as the total entropy does not changed then, the temperature increases

  $S(T_0, H_0) = S(T_1, H_1)$ (1.2)

  This adiabatic temperature rise can be visualized as the isentropic difference between the corresponding S (T; H) functions and it is a measurement of the MCE in the material

  $\Delta T_{ad} = T_1 - T_0$ (1.3)

- When the magnetic field is applied isothermally (T remains constant), the total entropy decreases due to the decrease in the magnetic contribution, and therefore, the entropy change in the process is defined as

  $\Delta S_m = S(T_0, H_0) - S(T_0, H_1)$ (1.4)

Both the isothermal magnetic entropy change $\Delta S_m$, and the adiabatic temperature change $\Delta T_{ad}$ are described effect and values of MCE. Both quantities depended of the initial temperature $T_0$, and the magnetic field variation $\Delta H = (H_1 - H_0)$

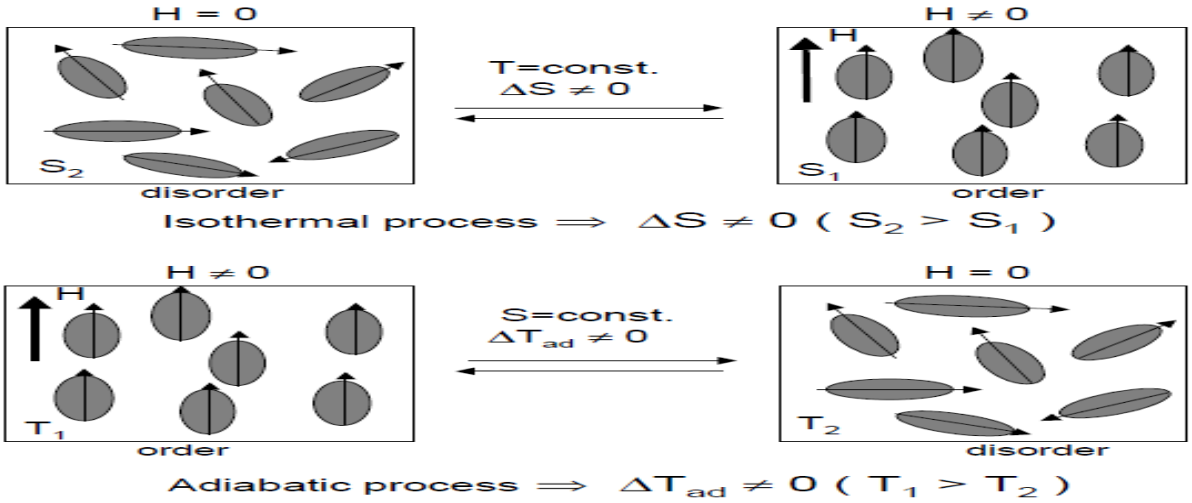


Figure 0-10: the two basic processes of the magnetocaloric effect when a magnetic field is applied or removed in a magnetic system: the isothermal process, which leads to an entropy change, and the adiabatic process, which yields a variation in temperature.

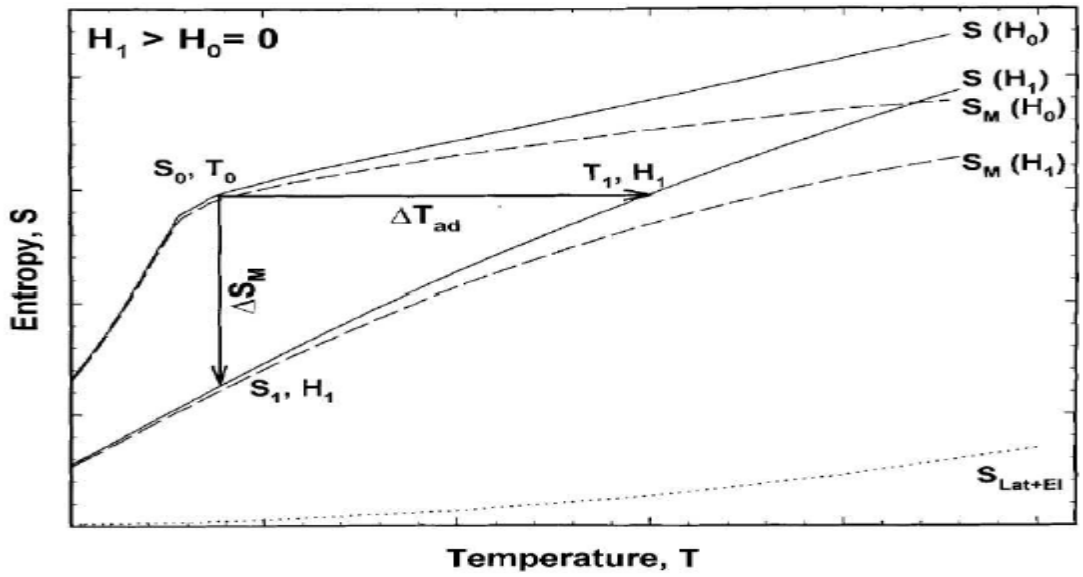


Figure 0-11: diagram showing the MCE. Solid lines represent the total entropy in two different magnetic fields (H0 = 0 and H1 > 0), dotted line shows the electronic and lattice contributions to the entropy (non-magnetic), and dashed lines show the magnetic entropy in the two fields. The horizontal arrow shows $\Delta T_{ad}$ and the vertical arrow shows $\Delta S_m$ , when the magnetic field is changed from H0 to H1. Taken from Ref. [110].

The relation between applied field (H), the magnetization (m) and the temperature (T), versus the MCE grandeurs, $\Delta T_{ad}$ and $\Delta S_m$, is given by the by one of the Maxwell [112]

$$\left(\frac{\partial S(T,H)}{\partial H}\right)_T = \left(\frac{\partial m(T,H)}{\partial T}\right)_H \quad (1.5)$$

Integrating Eq.1.5 for an isothermal (and isobaric) process we get

$$\Delta S_m(T,\Delta H) = \int_{H_1}^{H_2}\left(\frac{\partial m(T,H)}{\partial T}\right).dH_H (1.6)$$

This equation indicates that the magnetic entropy change is proportional to both the derivative of magnetization with respect to temperature at constant field and to the field variation. Using the following thermodynamic relations [112]:

$$\left(\frac{\partial T}{\partial H}\right)_S = -\left(\frac{\partial S}{\partial H}\right)_T.\left(\frac{\partial T}{\partial S}\right)_H \quad (1.7)$$

$$C_H = T\left(\frac{\partial S}{\partial T}\right)_H \quad (1.8)$$

$C_H$ denote the heat capacity at constant field, and referring to Eq. 1.5, the infinitesimal adiabatic temperature is given by:

$$dT)_{ad} = -\left(\frac{T}{C(T,H)}\right)_H \left(\frac{\partial m(T,H)}{\partial T}\right)_H dH \quad (1.9)$$

After integrating this equation, we get other expression describe the magnetocaloric effect

$$\Delta T)_{ad} = -\int_{H_1}^{H_2} \left(\frac{T}{C(T,H)}\right)_H \left(\frac{\partial m(T,H)}{\partial T}\right)_H dH \quad (1.10)$$

By analyzing Eqs. 1.6 and 1.10 all information about behavior of the MCE in solids can be gained

- Magnetization at constant field in both paramagnets (PM) and simple FM decreases with increasing temperature. Hence $\Delta T_{ad}(T, \Delta H)$ should be positive while $\Delta S_m(T, \Delta H)$ should be negative for positive applied field changes.
- In FM the absolute value of the derivate of magnetization as function of temperature $\left|\left(\frac{\partial M}{\partial T}\right)_H\right|$ is maximum at $T_c$, and therefore $\Delta S_m(T, \Delta H)$ should shows a peak at $T=T_c$ $\Delta T_{ad}(T, \Delta H)$ in FM shows a peak when $\Delta H$ tends to zero [113]
- For the same $\Delta S_m(T, \Delta H)$ value, the $\Delta T_{ad}(T, \Delta H)$ value will be larger at higher T and lower heat capacity.

### 2.3.3 Measurement of the Magnetocaloric effect

- Direct measurement

In this technique we based on measurement of the initial ($T_0$) and final ($T_f$) temperatures of the material, when the magnetic field changes for an initial ($H_0$) to a final value ($H_f$).

So, the measurement of the adiabatic temperature change is given by:

$$\Delta T_{ad}(T_0, H_f - H_0) = T_f - T_0$$

To make measurement more efficient, a rapid change of applied magnetic field is needed. Therefore, the measurement can be released ether on immobilized samples by changing the applied magnetic field [115], or by moving samples in and out of a constant applied magnetic field [114].

The accuracy of the measurement depends on these effects : the errors in thermometry and in field setting, the quality of thermal insulation of the sample, the possible modification of the reading of temperature sensor due to the applied field, according to these effect the accuracy is claimed to be within the 5-10% [110, 115, 114].

- Indirect measurement

This method is devoted to calculate $\Delta S_m(T, \Delta H)$ and $\Delta T_{ad}(T, \Delta H)$ by intervening the magnetization measurement, in this case the magnetization measured as function of T and H. This present a way to obtain $\Delta S_m(T, \Delta H)$ by integration of Eq. 1.6. The accuracy of $\Delta S_m(T, \Delta H)$ calculated from magnetization data depends on the accuracy of the measurements of the magnetic moment, T and H. It can be also affected by the exact differential in Eq.1.6. In fact, the error in the value of $\Delta S_m(T, \Delta H)$ can take range of 3-10%.

On the other hand, the measurement of heat capacity lead to calculate the entropy of solid following these equations:

$$S(T,H)_{H=0} = \int_0^T \left(\frac{c(T)}{T}\right)_{p,H=0} dT + S_0$$

$$S(T,H)_{H\neq 0} = \int_0^T \left(\frac{c(T)}{T}\right)_{p,H} dT + S_{0,H}$$

Where $S_0$ and $S_{0,H}$ are the zero-temperature entropies, for condensed systems $S_0 = S_{0,H}$[116]

However, this evaluation depends of types of order transitions, is not valid for first order transition where both entropy and entropy change curves present a discontinuity and the

accuracy in the measurement of MCE depends critically of accuracy of heat capacity when using $C(T)_{P,H}$ .

### 2.3.4 Magnetocaloric near room temperature

The lanthanide Gd is the sample materials at room temperature present a ferromagnetic ordering ($T_c$ = 294K), the values of $\Delta T_{ad}$ at $T_c$ can reach 6, 12, 16 and 20K for respectively applied magnetic field changes $\Delta H$ = 2, 5, 7.5 and 10T, many studies are devoted to study this lanthanide [113, 115, 118, 119]. To improve the MCE many alloys based of Gd and other rare earth metal have been elaborated, the only favorite alloys can increase the MCE are nanocrystalline Gd-Y witch enhance the MCE in Gd for $\Delta H = 1T$ [120]. In addition, most intermetallic compound shows a magnetic order in vicinity at room temperature and less than 290K exhibit a lower MCE than that of Gd. The $Y_2F_{12}$ with $T_c$ = 310K donate an MCE witch about 50% of that in Gd [121]. The same extent for $Nd_2F_{17}$ [121] with $T_c$ = 324K. The only intermetallic compounds that display an MCE as large as that of Gd are $Gd_5Si_4$ ($T_c$ = 335K) and the germanium substituted solid solution $Gd_5(Si_xGe_{1-x})_4$, for $0.5 \leq x \leq 1$, with $T_c$ from 290 to 335K [117]

### 2.3.5 Magnetic Refrigeration

Recently, refrigeration based on MCE present a worth deal and efficient process compared by traditional technic based on vapor compression refrigerator. The vapor compression refrigerator encloses significant inconveniences, such as the low efficiency presented in refrigerator dimension and has negative effects on the environment (use ozone-depleting chemicals (such as chlorofluorocarbons), hazardous chemicals (such as ammonia), or greenhouse gases (hydrochlorofluorocarbons and hydrofluorocarbons), for that reason, magnetic refrigeration is a technology to overcome vapor compression refrigerators.

In addition, the energy loss incurred during refrigeration cycle in magnetic refrigeration is weak than vapor compression refrigerator. In compression refrigeration the cycle composed from two phases :

- Compression phase: the gas be hot and the induced heat is evacuated to the hot source.

- Decompression phase: the refrigerant gas cools to absorb heat from the cold source or from the space to be cooled.

The process of magnetic refrigeration look like the compression refrigeration, can be reproduced by replacing the gas with the magneto-caloric material and the compression/ decompression phases with the magnetization/ demagnetization phases. Thus, the repetition of the magnetization and demagnetization cycle combined with the heat exchanges with the appropriate hot and cold sources replaces the operation of the compressor encountered in the conventional systems.

The principle of the magnetic refrigeration consists of four steps (**Figure 0-12**):

- The refrigerant material is adiabatically magnetized and its temperature is increased;
- The heat is transferred from the refrigerant material to a heat exchanger, so the temperature decreases to return to room temperature T0;
- The refrigerant material is adiabatically demagnetized and due to the magnetocaloric effect, its temperature is decreased;
- The refrigerant material can absorb heat from space we want to cool and its temperature is increased back to the starting temperature.

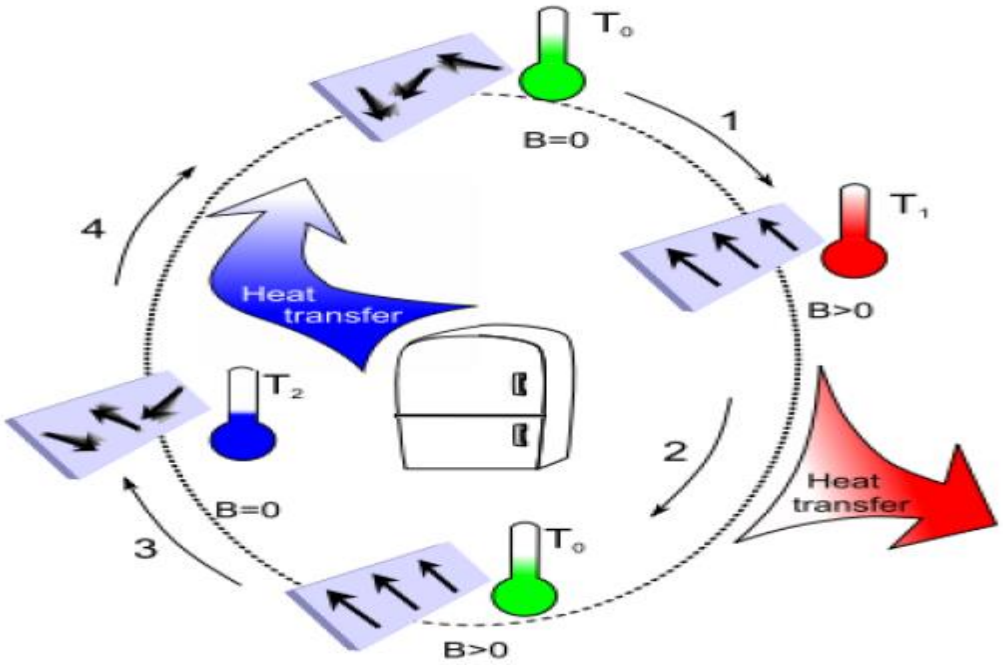


Figure 0-12: Principle of the magnetic refrigeration according to ref. [122].

The performance of such a magnetic refrigeration system demands, the study of these following issues:

- The thermodynamic cycle.
- The magnetic field sources.
- The magneto-refrigerant material.

### 2.3.6 Thermodynamic cycles

The magnetic refrigeration obeyed a several thermodynamic cycle like:

Brayton cycle, Ericsson cycle as well as AMR cycle.

a) Brayton cycle
the Brayton cycle is based on two adiabatic processes and two isofield processes [122]. It is one of the most basic cycles of refrigeration. Brayton cycle is, in turn, divided into four states. Show Figure 0-13.

- Isentropic processes (A-B, C-D)
    - A-B: the refrigerant material is adiabatically magnetized and its temperature is increased, whereas its total entropy remains constant.
    - C-D: Removing the magnetic field, the refrigerant material turns down in the adiabatic demagnetization process.
- Isofield processes (B-C, D-A)
    - B-C: The heat of the material is evacuated to the extern cool source.
    - D-A: The heat can be absorbed by the hot source and this leads to the additional cooling of the system.

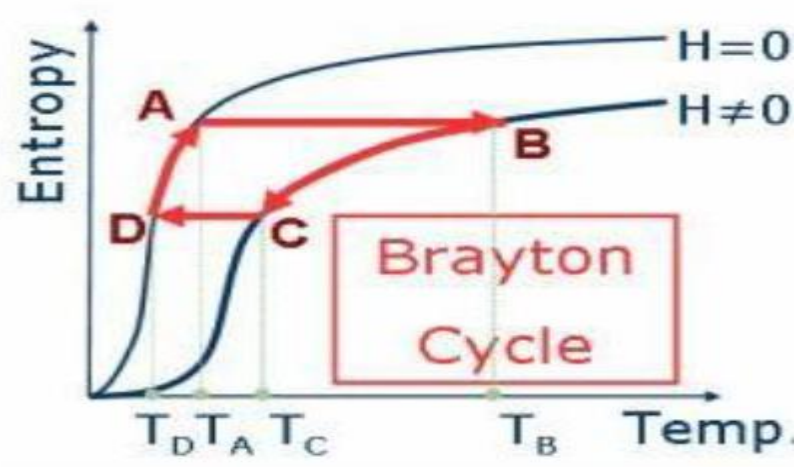


Figure 0-13: Brayton cycle

b) Ericson cycle:
The Ericson cycle contains two isotherm processes and two isofield processes and needs a thermal regenerator for its operation. Ericsson cycle is divided into four stages.

- Isothermal processes (A-B, C-D)
    - **A-B:** In the presence of magnetic field the refrigerant material transfers its heat to the regenerator.
    - **C-D:** The magnetocaloric material will reabsorb heat from the regenerator whereas its temperature become constant.
- Isofield processes (B-C, D-A)
    - **D-A:** The magnetocaloric material absorbs the heat stored in the regenerator during the isofield process (B-C). **B-C:** The magnetocaloric material loses heat absorbed in process (D-A).

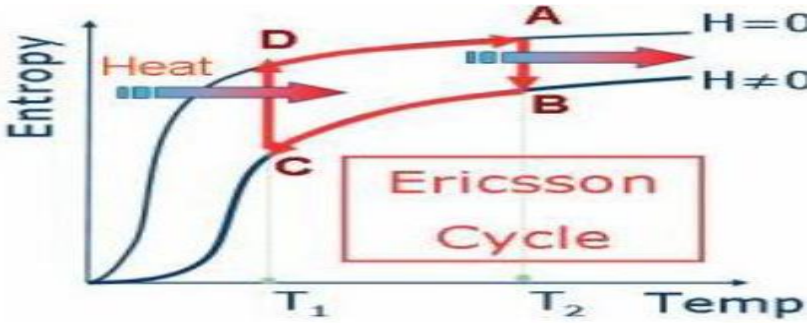


Figure 0-14: Ericson cycle

c) Active Magnetic Regenerator Cycle

The AMR cycle based on two processes:

- Adiabatic process magnetization/demagnetization
- Two isofield processes

This make AMR cycle similar to the Baryon cycle. However, in the AMR, the refrigerant provides both refrigeration and regeneration. The diagram of ARM is illustrated in Figure 0-15. Four cases are generated the AMR cycle:

(a) adiabatic magnetization: each particle in the bed become hot;

(b) isofield cooling: The high magnetic field is present; the fluid is blown from the cold end to the hot end and absorbs heat from the bed and remove heat at a temperature higher than TH in the hot heat exchanger;

(c) adiabatic demagnetization: each particle in the bed cools again;

(d) isofield heating: The magnetic field is zero, the fluid is blown from the hot end to the cold one and it expels heat to the particles of the bed and absorbs heat at a temperature lower than TC in the cold heat exchanger.

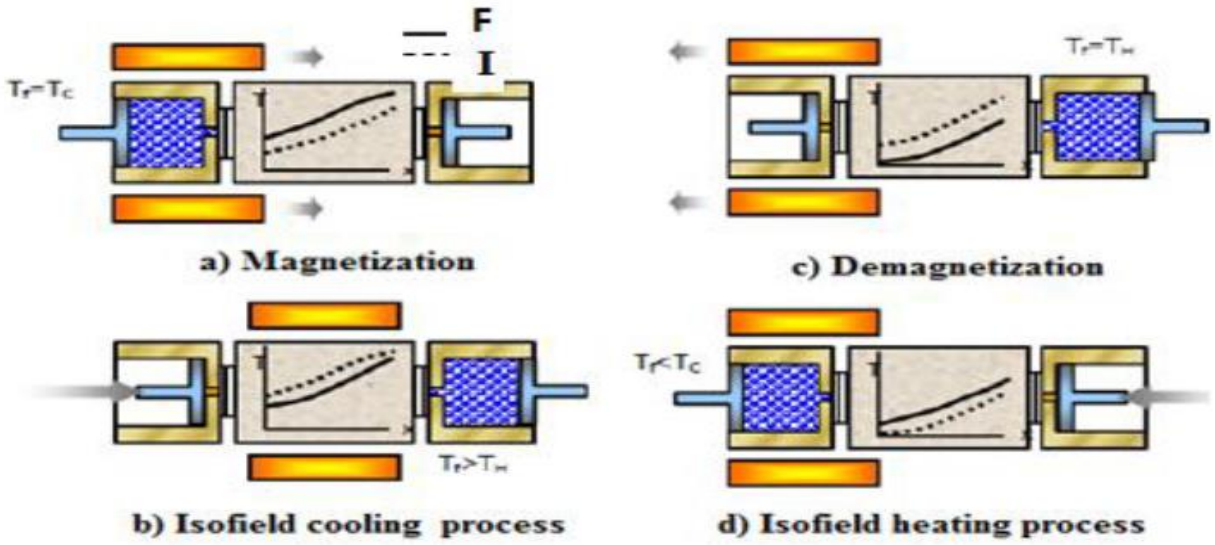


Figure 0-15: AMR cycle [122]

### 2.3.7 Relative Cooling Power (RCP)

The Relative Cooling Power reflated the performance of refrigerant material, it indicates how

much heat can be transferred between this material and its environment from the cold end to the hot end of a thermodynamic cycle. Gschneidner and Pecharsky, (2000) [123] proposed the relative cooling power as a new indicator to determine a good material suitable for the magnetic refrigerators area and to characterize magneto-caloric properties. This parameter can differentiate the magnetic materials between them.

This parameter (RCP) is defined as a product of $\Delta S_m(T, \Delta H)$ or $\Delta T_{ad}(T, \Delta H)$ peak value and the full width at half maximum ($T_{FWHM}$) of $\Delta S_m = f(T)$ or $\Delta T_{ad} = f(T)$ a curve, the Relative Cooling Power (RCP), predicated on both the magnetic entropy and the adiabatic temperature change, is given by:

$RCP(S) = \Delta S_m(\max) \times \partial T_{FWHM}$ or $RCP(T) = \Delta T_{ad}(\max) \times \partial T_{FWHM}$

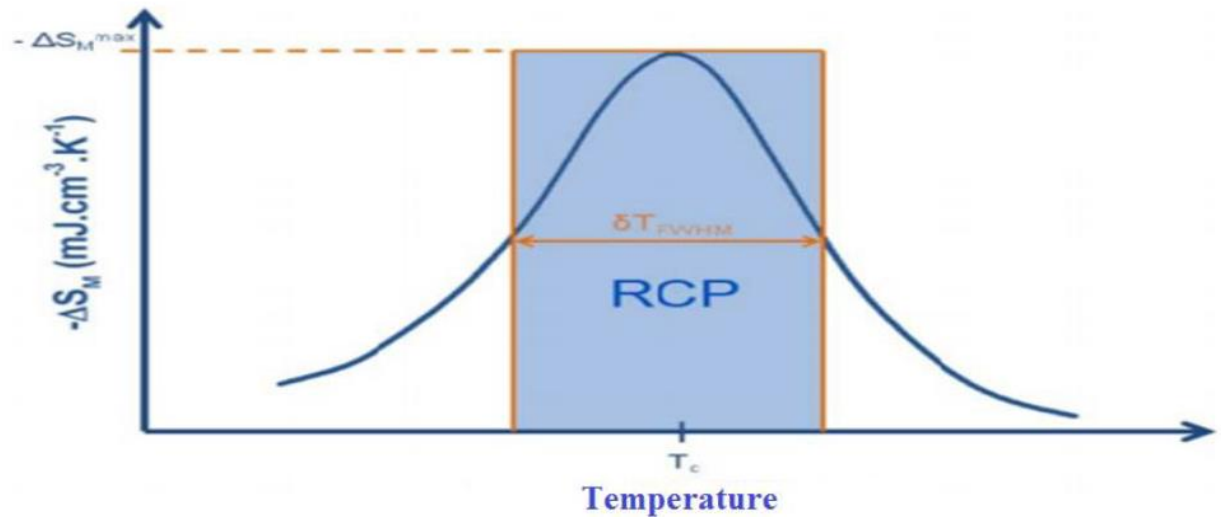


Figure 0-16: Presentation of the relative cooling power RCP

The larger RCP indicates the better magneto-caloric material.

# Part 3: Inverstigationon on magnetic, electronic properties and magnetocaloric effect of materials; Spintronics materials and magnetic refrigeration ones.

## 3.1 Investigation on electronic and magnetic properties of FeS by first principle and Monte Carlo simulations

### 3.1.1 Introduction

The mono-sulfide solid based on (Fe, Ni) present a vital precursor of primary the

Fe-Ni sulfides for this compound [124]. Wang et al. [125] reported that the substructure of the iron mono-sulfide of the general formula $Fe_{1-x}S$, where x $0 < x < 0.125$, has the same substructure of NiAs, with a hexagonal close-packed structure including troilite (FeS), monoclinic and hexagonal pyrrhotites. Connected to the hexagonal FeS, Kavner et al. [127] analyzed that structure in terms of the phase stability, density at high pressures and temperatures. Also, these authors confirm the appearance of this hexagonal structure FeS under cooling conditions, suggesting that the crystals nucleated from the FeS melt. With strong thermodynamic stability of the hexagonal phase, they considered cooling conditions.

Chemically, to prepare troilite compound, the mechano-chemical reaction between pyrite $FeS_2$ and elemental iron Fe to get the troilite FeS follows the formula: $FeS_2 + Fe \rightarrow 2FeS$ [126]. About the structure and composition related to superconductivity and magnetism, a study occurred to compare the tetragonal and hexagonal FeS [128]. The hexagonal magnetically orders well above room temperature when the tetragonal FeS is a filamentary superconductor below ($T_C$ = 4 K), having a magnetic anomaly at ~ 15 K and commensurate antiferromagnetic (AFM) order below ($T_N$ = 116 K).

In comparison with hexagonal FeS and tetragonal FeS, Kuhn et al [128]. reported that there are two susceptibility features, at 450 K where a spin transition in which the spins rotate along the c axis whereas, a structure transition occurred at $T_N$ = 600 K.

The calculations prove existence of an extreme coupling of magnetism of that structure, and the tetragonal recognizes a borderline nearest neighbor AFM instability, with magnetism strongly dependent on the sulfur concentration [129].

Pyrrhotite exhibits distinct magnetic anisotropy. Along the direction parallel to the c-axis, it is AFM or ferrimagnetic, while perpendicular to this direction and within the same ab-plane the crystal is ferromagnetic (FM) [130]. However, troilite exhibits the AFM phase, in which magnetic moments are neutralized to zero due to reversely orientated spin moments in adjacent ab-planes [125].

The Magnetic properties of troilite have been extensively studied by a number of authors above room temperature: Hirahara and Murakami [131]; Haraldsen [132]; Horwood et al. [133]; Schwarz and Vaughan [134] and Li and Franzen [135].

In addition, among magnetic iron sulfides, the system of pyrrhotite solid solution series: ($Fe_{1-x}S_x$, where $0 < x < 0.13$) displays a wide range of magnetic transitions [136].

### 3.1.2 Calculation method and Hamiltonian model

#### 3.1.2.1 Monte Carlo simulations

The Monte Carlo simulations (MCS) under the Metropolis algorithm, have been performed to study the magnetic properties of various complex structures that are difficult to handle with other simulation tools.

The principle of this simulation is to change the value and/or the orientation of the spin of all sites in the lattice at every step MCS. The Metropolis algorithm allows accepting the change or not. The physical quantities, namely the energy and the magnetic order parameter, are calculated. After normalization of these quantities, their average values at equilibrium are deduced. Then the specific heat and the magnetic susceptibility are calculated.

The equations used to calculate the magnetic order parameter noted $m$, the energy $E$, the

magnetic susceptibility χ and the specific heat $C_v$are respectively given by:

$$m = \frac{1}{N} <\sum_i Si > \quad (3.1)$$

$$E = \frac{1}{N} < H > \quad (3.2)$$

$$\chi = \beta(< m^2 > - < m >^2) \quad (3.3)$$

$$C_v = \beta^2(< E^2 > - < E >^2) \quad (3.4)$$

Where $\beta = \frac{1}{k_\beta T}$ and $k_\beta$represents the Boltzmann constant. For simplicity reason, we fix $k_\beta = 1$ in all the flowing calculations.

### 3.1.2.2 Hamiltonian model

The Hamiltonian of the studied system is given by:

$$H = -J_1 \sum_{<i,k>} S_i S_k - J_2 \sum_{<i,l>} S_i S_l - d\sum_i (S_i)^2 \qquad (3.5)$$

Where $S_\alpha$ with $\alpha = i, k, l$ stands for spin random variables which take the values ±2, ±1,0. First summation runs over the first nearest neighbors with AFM interaction $J_1 < 0$. The second summation runs over the second nearest neighbors with FM interaction $J_2 > 0$ and the third summation runs over all spins with crystal field interaction d.

This crystal field is originated from the competition between Fe-Fe, the rest of this subsection is devoted to the study of the corresponding magnetic properties exploring numerical techniques based on Monte Carlo computations.

### 3.1.2.3 ab initio calculation

Based on Density Functional Theory (DFT) and the Full Potential Linearized Augmented Plane-Wave (FPLAPW) method which is implemented in WIEN2K code [31], we study the magnetic properties of hexagonal FeS. The exchange correlation potential was treated using the Generalized Gradient Approximation (GGA) for the total energy calculations [15]. The atomic muffin-tin (MT) spheres, supposed not to be overlapped with each other, are taken as 2.22 and 1.54 atomic units (a.u), for Fe and S, respectively. The cut off is specified as the product of the smallest muffin-tin (atomic) sphere radius noted by $R_{MT}$ and the magnitude of the largest wave vector.$K_{max}$ via the following relation:

Cut off = RMT.Kmax. (3.6)

We use $R_{MT}.K_{max}=7$ in this study and 700 k-points in the irreducible Brillouin zone for self-consistent convergence. The convergence criterion was chosen to be the total energy set at 0.00001 eV.

X-ray and neutron-diffraction experiments show that the material is well crystallized in single-phase (see Figure 3.1-1), and has NiAs structure (a=b=5.966Å, c=11.66Å)[136]

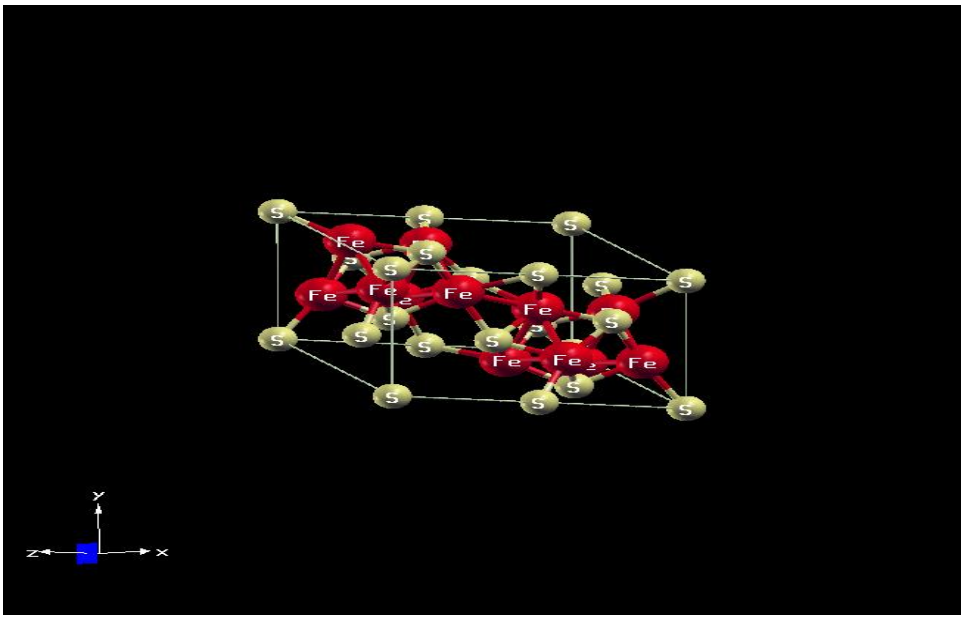


Figure 3.1-1: Hexagonal structure of FeS compound

### 3.1.3 Results and discussion:

#### 3.1.3.1 Electronic and Magnetic Properties of hexagonal FeS with ab initio calculation:

The density of states (DOS) of hexagonal FeS is plotted in Figure 3.1-2 and Figure 3.1-3. From the total and partial DOS (Figure 3.1-2.a and Figure 3.1-2.b), we predicted the FM state in which the spin up and spin down are not symmetrical, this result confirms that we have a magnetic compound with a total magnetic moment of 2.62 $\mu_B$.

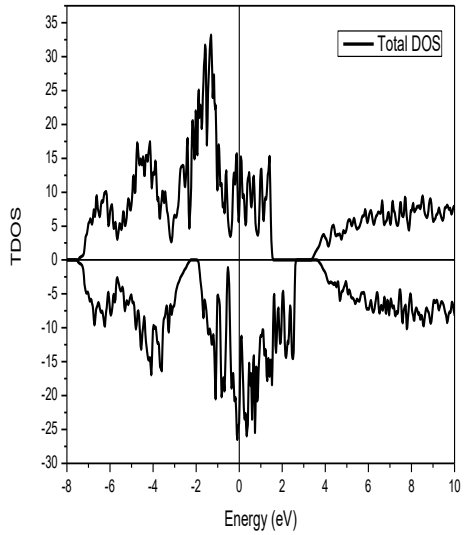


Figure 1-2.a

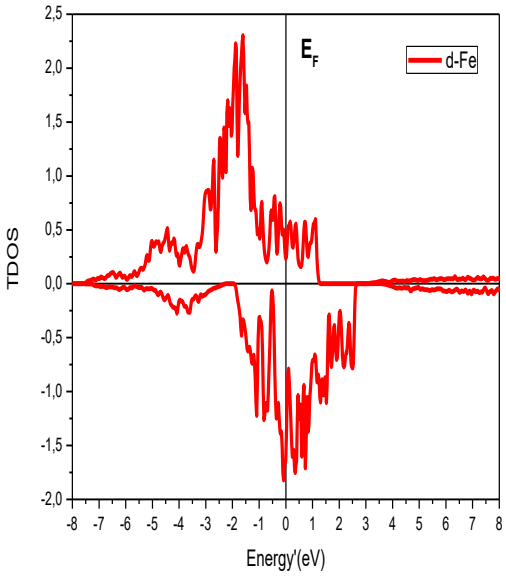


Figure 1-2.b

Figure 3.1-2**:** Total (a) and partial (b) density of states of FeS compound for the FM state treated by GGA approximation.

For the AFM state, Figure 3.1-3.a has shown the AFM A-type state in which the first nearest neighbor has an AFM coupling and the six second nearest neighbors have FM coupling. In the first case, Figure 3.1-2.a and Figure 3.1-2.b, we have a little polarization and the total magnetic moment is due to the 3D orbital of Fe polarized states (Figure 3.1-2.b). In the second case, Figure 3.1-3.a, we predicted a weak total magnetic moment due to the hybridization with orbital Fe-3d. In Figure 3.1-3.b, the partial DOS composed by Fe-3d, S-2p and S-2s, the orbitals are mainly contributed to the valence band. We can distinguish the crystal field ($t_{2g}$-$e_g$) of Fe-3d only for the FM state, and the 3d orbital contains 4 up electrons.

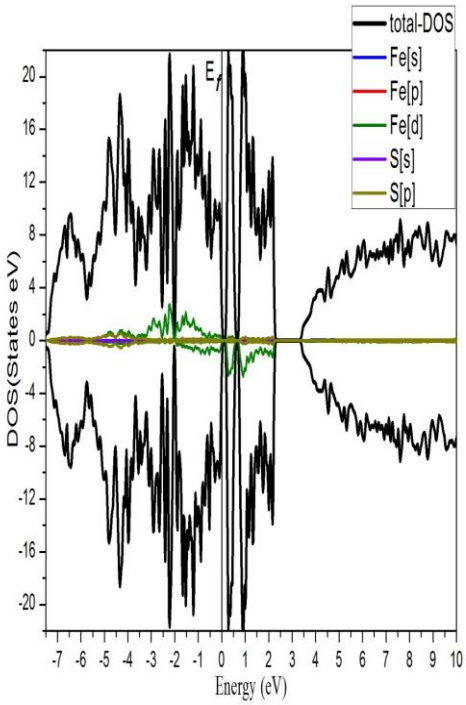


Figure 1-3.a

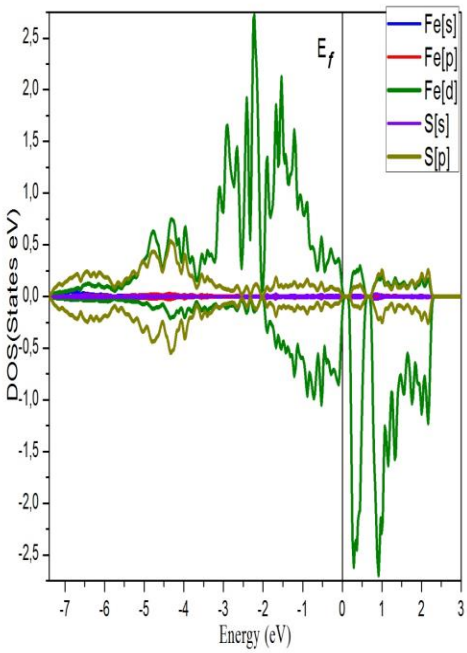


Figure 1-3.b

Figure 3.1-3: Total DOS (a) and partial DOS (b) for the AFM A-type state of FeS compound treated by GGA approximation.

The calculation of different exchange coupling has been deducted by following equation:

$j_{1=} -\frac{E_{FM} - E_{AFA}}{2.Z.m}$ , where $Z = 2$, $m = 2$, $E_{FM}$ denotes the energy of ferromagnetic state and $E_{AFA}$ is the energy of antiferromagnetic state type A.

$j_{2=} -\frac{E_{FM} - E_{AFB}}{2.Z.m}$ , where $Z = 6$, and $m = 2$, $E_{FM}$ denotes the energy of ferromagnetic state and $E_{AFB}$ is the energy of antiferromagnetic state type B.

The results show that $J_1 < 0$, ($J_1$= -383 K) and $J_2 > 0$, ($J_2$=29 K), that is to say that the FM coupling is dominated in the plan, whereas the AFM coupling is strongly dominated and follows the c-direction.

Here, we should mention that the obtained exchange couplings in Monte Carlo simulation are based on the presented DFT calculations. Then we computed the following magnetic parameters: magnetizations, susceptibilities and phase diagrams. These results have been discussed in the next section.

### 3.1.3.2 Ground state phase diagram (T = 0 K)

To investigate which phase is stable, we calculate the energies of this system and compare them for different configurations. From the Hamiltonian (1), we have computed and compared five possible configurations: (m = 2), (m = −2), (m = 1), (m = −1) and (m = 0) connected to the energy. We found that the ground state is AFM A-type, for various parameters, $J_1$ and $J_2$. Each stable phase is obtained by minimizing the energy value for fixed values of the parameters: $J_1$ and $J_2$. The corresponding phase diagram is illustrated in Figure 3.1-4.

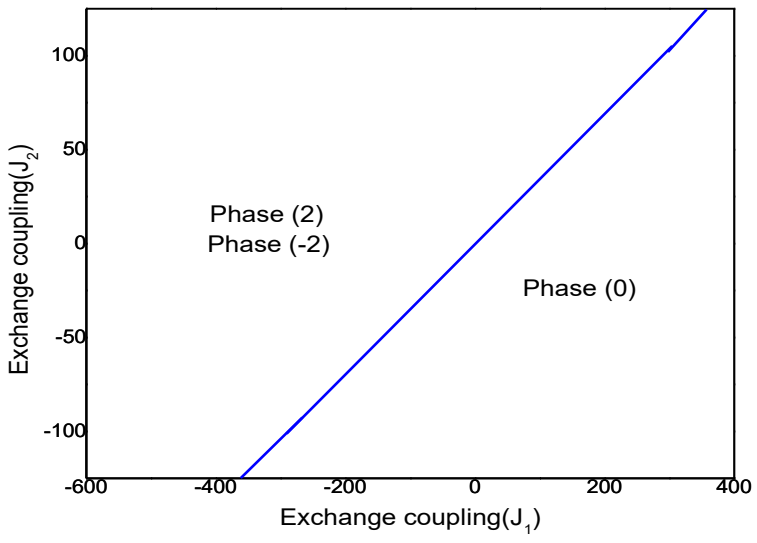


Figure 3.1-4: Ground state phase diagram, in the plan ($J_1$, $J_2$).

The most stable one is reported in the phase diagram (Figure 3.1-4) associated to the plan ($J_1$, $J_2$).

In the absence of the external magnetic field, we found only three phases: phase (2), phase (−2) and phase (0). Those phases are stable and the phases: (2) and (−2) have the same energy.

### 3.1.3.3 Monte Carlo study (T >0 K)

In this section, we have examined the magnetic properties in case of the T > 0K. We studied the magnetic properties of hexagonal iron sulfide using Monte-Carlo simulation based on the Metropolis algorithm.

The Monte Carlo simulation (MCS) combined with Metropolis algorithm, have proven their efficiency in the study of the magnetic properties of various complex structures which show some difficulties to handle with other simulation tools.

The principle of this simulation is to change the value and/or the orientation of the spin of all sites in the lattice at every step Monte Carlo. The Metropolis algorithm allows accepting the change or not. The physical quantities, namely the energy and the magnetic order parameter, are calculated. After normalization of these quantities, their average values at equilibrium are deduced. Then the specific heat and the magnetic susceptibility are calculated at the end of the simulation.

In Figure 3.1-5 we plotted the magnetization versus the temperature for different lattice sizes, we concluded that the magnetization decreases with the increase of temperature until it disappears at critical temperature $T_N$=450K, this value in good agreement with the data reported by Kuhn et al [128], when the spin flips along the c-axis. Moreover, the second-order transition has occurred due to the continuity of the magnetization.

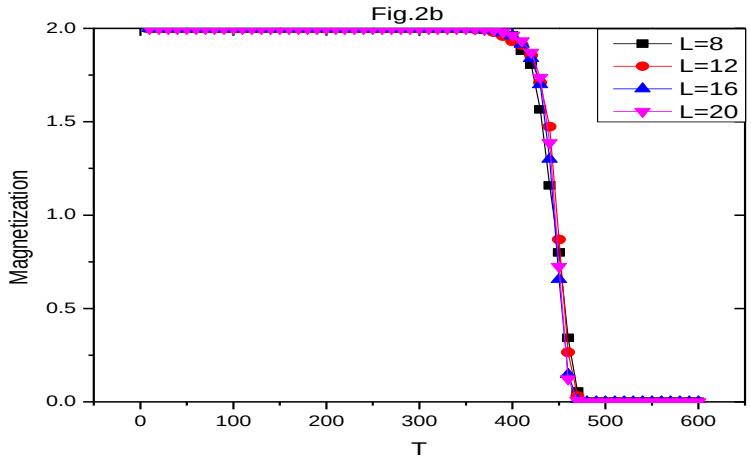


Figure 3.1-5: Magnetizations as a function of temperature for various system sizes: L= 8, 12, 16 and 20.

Similarly, Figure 3.1-6 depicted that the momentum of the peaks of susceptibility increase with rising the system size lattice. In addition, the peaks of susceptibility characterized the critical temperature $T_N$ = 450K. and separates the AFM A-type phase and the paramagnetic phase.

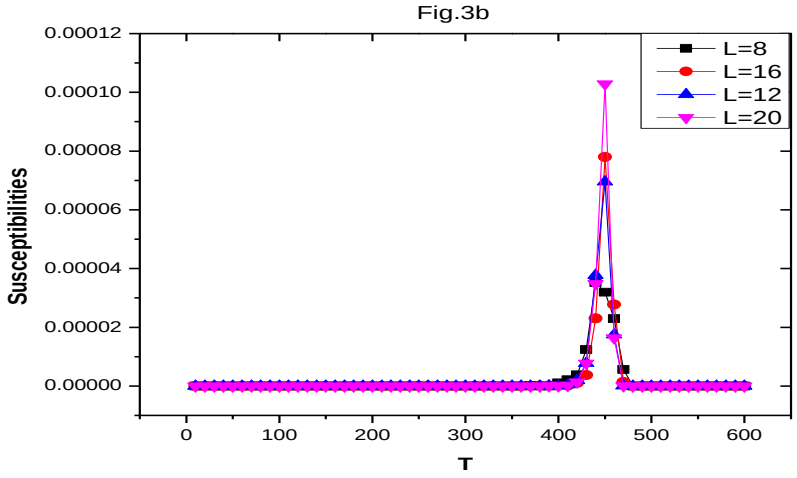


Figure 3.1-6: Susceptibilities as a function of temperature for various system sizes: L= 8, 12, 16 and 20.

Figure 3.1-7 illustrates the variation of magnetization versus the exchange coupling ($J_1$) for different temperatures and for a fixed value of $J_2$=29 and d=1. We noticed that the ordered state increases with temperature increasing, thus we can determine the necessary exchange coupling

for transition from the ordered phase (AFM) to the paramagnetic phase at each temperature.

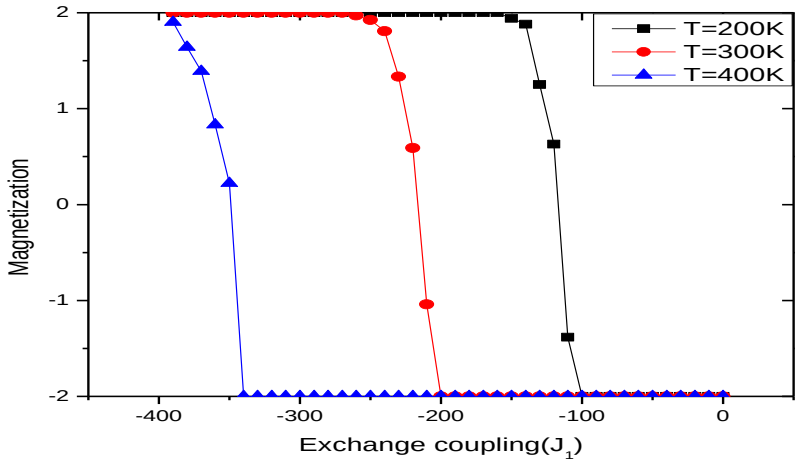


Figure 3.1-7: Magnetization as a function of exchange coupling $J_1$ at fixed temperature T=200, 300 and 400K.

### 3.1.4 Conclusion

The electronic and magnetic properties of the hexagonal FeS have been investigated using both DFT and MCS methods,

Within DFT calculations we predicted the total and partial DOS, spin moment, energies and the coupling interactions between $J_{Fe\text{-}Fe}$ in different directions. We found the minimum energy which corresponds to the AFM A-type state. Then we utilized Monte Carlo simulation based on Metropolis algorithm and spins Hamiltonian to study phase diagram and magnetization properties.

We discussed the phase configuration at (T = 0 K), as a result, we found two stable phases which are (m = ±2) and (m = 0). besides, at (T > 0 K), we have investigated the magnetization behaviors and magnetic susceptibility for different system sizes which have exhibited second-order phase transitions at $T_N$ = 450K.

## 3.2 The magnetocaloric and magnetic properties of the $MnFe_4Si_3$: Monte Carlo investigation.

### 3.2.1 Introduction

The magnetocaloric effect (**MCE**) is discovered in 1881, this effect presents a challenge to explain and understand the process of this effect, in fact several investigations have been carried on this subject, when it was first observed in iron [138].

The technology based on the ***MCE*** present high efficiencies and, in contrast to thermoelectric, which can arrive at (30 to 60%) of the Carnot-cycle [125].Regarding the vapor compression refrigerator is shows inconveniences, such as the low efficiency presented in refrigerator dimension and has negative effects on the environment, for that reason, magnetic refrigeration is a promising technology to overcome vapor compression refrigerators [125-126]

Many studies devoted to the ***MCE*** proposed that the materials based on $Gd_5Ge_2Si_2$ [127,139] and arsenide: $MnFeP_{1-x}As_x$ are good candidates for their properties.
Moreover, these systems present themselves as favorite candidates for better understanding of the fundamental mechanism of the MCE in magnetocaloric materials [140].
Meanwhile, the $Mn_{5-x}Fe_xSi_3$ systems are neither toxic nor expensive rare earth elements.
On the one hand, some previous studies [141,142] considered the $Mn_{5-x}Fe_xSi_3$ (x = 0, 1, 2, 3 and 4) matrix connected to the hexagonal structure ($P6_3/mcm$), Figure 3.2-1. In which the magneto caloric effect undergoes various magnetic phase transitions at different temperatures depending on their Fe amount. [143].

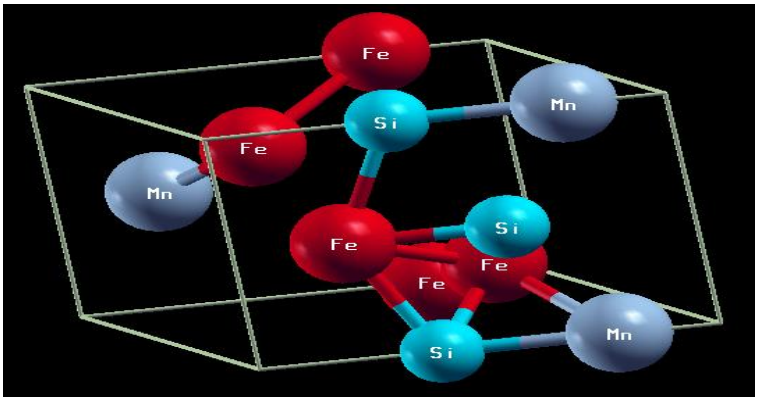


Figure 3.2-1: Hexagonal structure of $MnFe_4Si_3$ compound

On the other hand, the following researches [144-148] have been elaborated for $MnFe_4Si_3$ system, where the magnetic excitation spectrum of the ***MCE*** of the present system has been noticed [144]. At 300 K, $MnFe_4Si_3$ undergoes a phase transition to a ferromagnetic-ordered [146]. In addition, at 300K, it has the thermal evolution of the lattice parameters, showing an anisotropic characteristic and clearly reproducing the onset of magnetic ordering [146].

To better understand the magnetic behavior of $MnFe_4Si_3$ system, we have used the Monte Carlo method in connected to Ising model. For different sizes (L) of the present system (L = 8, 16 and 32), we have studied the magnetization and the susceptibility as well as the entropy for a field equal to 2T.

### 3.2.2 The model the Hamiltonian framework

#### 3.2.2.1 The Hamiltonian framework

The $MnFe_4Si_3$ structure exhibits a ***WP****:* Wyckoff positions: (6g and 4d) located by (Mn and Fe), respectively, the Fe surrounded by six Si.

In ref [144], the magnetic moment in Wyckoff positions: (4d), is neglected on while the magnetic moments of $1.5\mu_B$ is on the Wyckoff positions: (6g), in the basal plane of the hexagonal system.

Consequently, we deduced that the number of magnetic sites $N_{mag}$ is equal 1. Hence, we adopted the following Hamiltonian formula :

$$H - J_1 \sum_{<i,k>} S_i S_k J_2 \sum_{<i,l>} S_i S_l - d\sum_i (S_i)^2 - h \sum_i S_i \quad (3.7)$$

Where $S_\alpha$ (with $\alpha = i, k, l$) connected to the spin random variables (±3/2 and ±1/2).
The $[\sum_{<i,k>} S_i S_k]$ and $[\sum_{<i,l>} S_i S_l]$ summations are running over the (1st and 2ed nearest neighbors) with ferromagnetic interaction ($J_1 > 0$ and $J_2 > 0$) respectively.

From the exchange interactions calculated by Biniskoset al [144], we extract the exchange coupling $J_1$ and $J_2$, we found that ($J_1$ = 92 and $J_2$ = 20K). Given that, the relation between Heisenberg and Ising exchange coupling is expressed by the following equation [145]. Since the number of the magnetic site in our system is 1 which is 6g (Wyckoff position), then $N_{mag} = 1$

$$J_{Heis} = \frac{J_{Ising}}{N_{mag}} \quad (3.8)$$

The $d$ denoted the crystal field, in this simulation we take $d$= 1 and the $[\sum_i (S_i)^2]$ summation is running over all spin with crystal field interaction. The $[\sum_i S_i]$ summation runs over all spin with the magnetic field $h$.

The next subsection (b and c) are devoted to the exchange coupling behavior and phase diagram and the used Monte Carlo framework, respectively. Then, the magnetocaloric properties is given and discussed in the part III.

#### 3.2.2.2 The exchange coupling behavior and phase diagram at T=0K.

The stability of the magnetic phases was studied in the present paper, we computed the energies of $MnFe_4Si_3$ compound and compare them for various configurations. From the formula (1), the

Hamiltonian is expressed. Then, sixteen possible configurations have been computed and compared, Figure 3.2-2. For various parameters ($J_1$ and $J_{2)}$, Each stable phase is found by minimizing the ($E$: energy) value for fixed values of the parameters ($J_1$ and $J_2$). We stated that the ground state is ferromagnetic. The appropriating phase diagram is presented, see Figure 3.2-2. The most stable one is stated in the phase diagram, which is related to the plan $J_1$, $J_2$. Furthermore, in the absence of the ***h***: external magnetic field ,we conclude that all possible phases are stable, namely: (3/2,3/2), (-3/2, -3/2), (-3/2,3/2), (3/2, -3/2), (1/2, -1/2),(-1/2, 1/2), (-1/2, -1/2), and (1/2, 1/2).

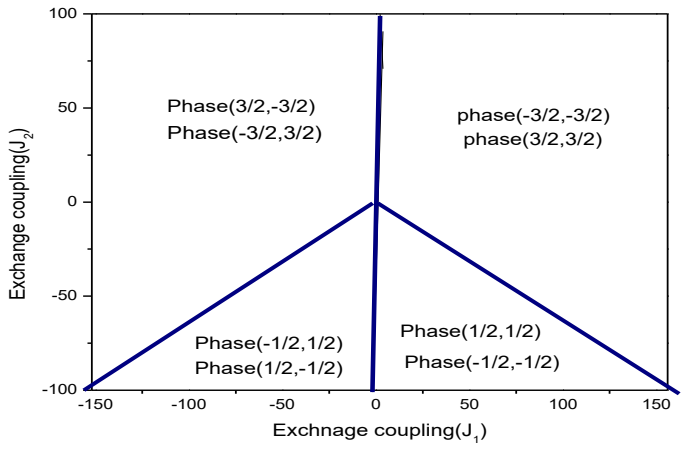


Figure 3.2-2: The exchange coupling and phase diagram

### 3.2.2.3 The magnetocaloric properties of $MnFe_4Si_3$ within the Monte Carlo framework

To describe the magnetocaloric and magnetic properties, the Monte Carlo simulation (***MCE)*** with Metropolis algorithm has shown their efficiency during the investigation of various structures.

In this work, using Metropolis algorithm on ***MCS*** and the flipping of the spin orientation of all

($MnFe_4Si_3$ sites) and Boltzmann weight condition. After the discard of a number of ***MCS***, that flip is being accepted or not by implementation of this algorithm.

The physical parameters (***m***: magnetic parameter order: , ***E***: energy , $\chi$: magnetic susceptibility, $\boldsymbol{C_v}$: specific heat, $\Delta \boldsymbol{S_m}$**:** magnetic entropy change, $\Delta \boldsymbol{T_{ad}}$: adiabatic temperature change and ***RCP***: relative cooling power) were studied and expressed by the following formulas:

$$m = \frac{1}{N} <\sum_i Si > \qquad (3.9)$$

$$E = \frac{1}{N} < H > \qquad (3.10)$$

$$\chi = \beta(< m^2 > - < m >^2) \qquad (3.11)$$

$$C_v = \beta^2 N(< E^2 > - < E >^2) \qquad (3.12)$$

where $\beta = \frac{1}{k_\beta T}$ and $k_\beta$ represents the Boltzmann constant

$$\Delta S_m = \int_0^{h_{max}} \left(\frac{\partial m}{\partial T}\right)_{h_i} dh \qquad (3.13)$$

$$\Delta T_{ad} = -T \frac{\Delta S_m}{C_{p,h}} \qquad (3.14)$$

where $C_{p,h}$ represents the total specific heat related to applied magnetic fields (***h***)

Basically, the solids and liquids can practically assume to be incompressible. Subsequently, $C_v$: specific heat at constant volume and $C_p$: specific heat at constant pressure have almost the same values, hence, only a single value of specific heat is

used for them. That is to say, $C_v \simeq C_p$. When the applied magnetic fields ($\boldsymbol{h}$) happens, we have this approximation $C_{v,h} \simeq C_{p,h}$.

$$RCP = \int_{T_1}^{T_2} \Delta S_m\ (T) dT \qquad (3.15)$$

Where, $T_1$ and $T_2$ are the cold and the hot temperatures which are corresponding to the two ends of the half maximum value of $\Delta S_m^{max}$, respectively

### 3.2.3 Outcomes and discussion

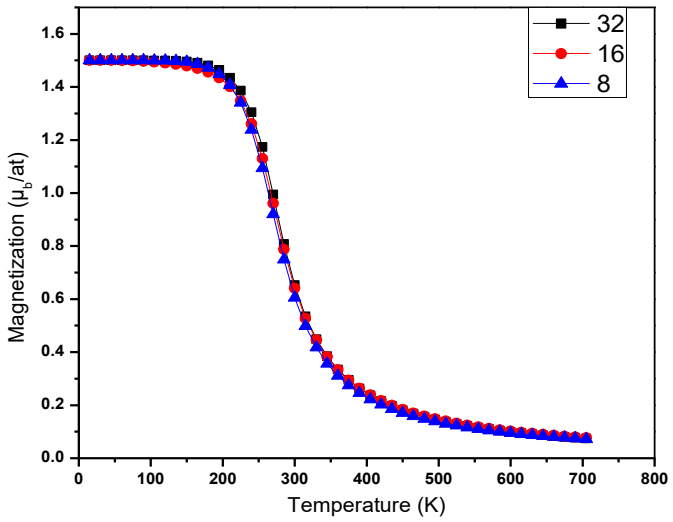


Figure 3.2-3: Magnetizations for different system sizes (L=8, 16 and 32 with h = 0T)

In Figure 3.2-3, in the absence of the applied magnetic field ($\boldsymbol{h}$ = 0T), we drew the magnetization for various system sizes (L = 8, 16 and 32). We observed that the magnetization is dropping with the augmenting of the temperature, when the temperature reaches the value of $T_C$ = 290K, the phase transition from ferromagnetic to paramagnetic occurred. Above $T_C$, the magnetization tends to zero. This value is in good harmony with the fact noticed by Biniskoset et al [144].

Moreover, the 2$^{ed}$ order transition is observed since of the magnetization continuity.

Similarly, in Figure 3.2-4 we expect that the momentum of the susceptibility peaks increases with increase of the different system sizes (L=8, 16 and 32).

The peaks of the susceptibility correspond to $T_C$=290K, as well as separate the phases of the ferromagnetic:(FM) and the para magnetic:(PM).

In the rest of this work we limit our study to L=32 size, in Figure 3.2-5, we observe the effect of (***h***: external magnetic-field) on the magnetization, we noticed that the ***"h"*** has an influence on the magnetization, where the Curie temperature shifts proportionally versus the variation of the ***"h"***.

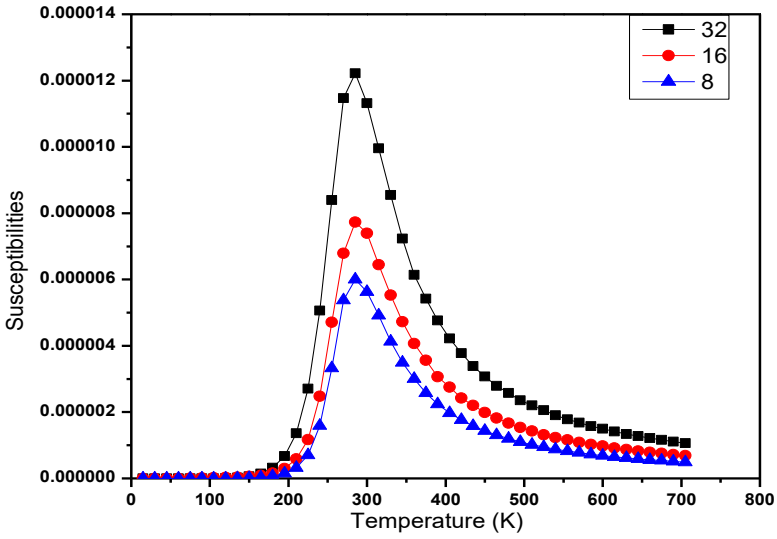


Figure 3.2-4: Susceptibilities and temperature for different system sizes (L=8, 16 and 32).

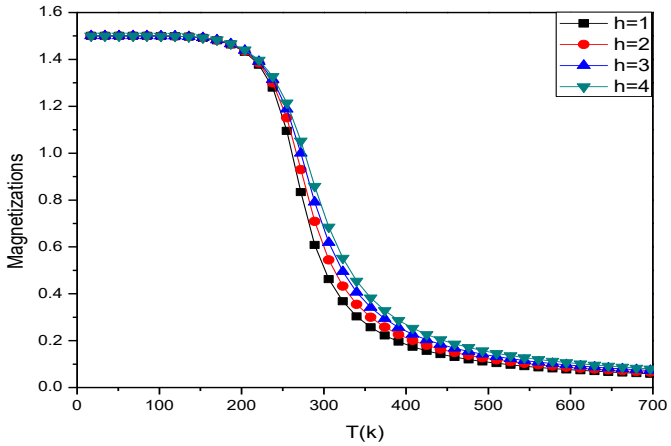


Figure 3.2-5: Magnetizations and temperature for different $\boldsymbol{h}$ values ($\boldsymbol{h}$ = 1, 2, 3 and 4T).

The $\Delta \boldsymbol{S_m}$**:** magnetic entropy change is depending on the temperature for different values of h=1,2,3, and 4 T, Figure 3.2-6, we see that $\Delta \boldsymbol{S_m} < 0$ in all temperature side, and is extended over a wide range of temperature approximately the $T_C$, which is convenient for above room-temperature (RT) magnetic refrigeration. At T =289 K The values of $\Delta S_m$ are 1.53, 2.6, 3.68, and 4.53J.(kg. K)$^{-1}$ when the applied magnetic fields having (1, 2, 3, 4) T, respectively. In addition, the obtained value for a magnetic field h = 2, and 3T presents a good agreement compared with the values reported in refs [146-147]. Similarly, in Figure 3.2-7 the adiabatic temperature change is negative and reflects the variation of the system's temperature during the adiabatic transformation.

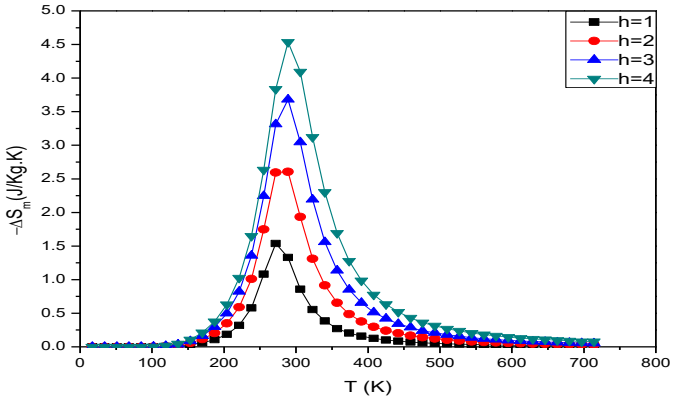


Figure 3.2-6: $\Delta S_m$: magnetic entropy change and temperature for different $h$ values ($h$ = 1, 2, 3 and 4T).

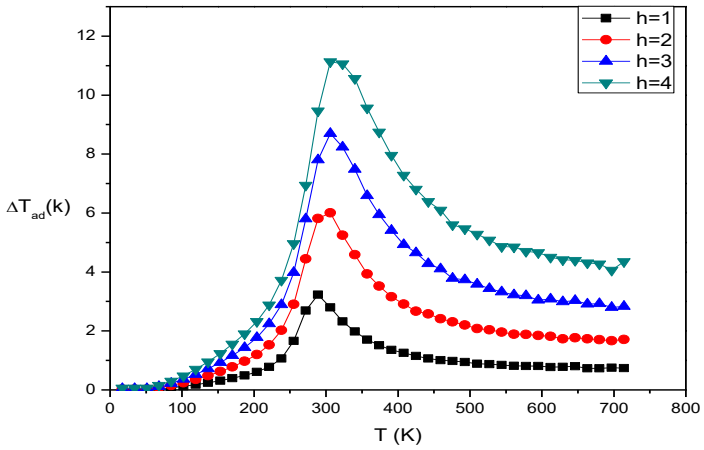


Figure 3.2-7: $\Delta T_{ad}$: adiabatic temperature change versus the temperature for different $h$ values ($h$ = 1, 2, 3 and 4T).

We conclude that the $\Delta T_{ad}$: adiabatic temperature change increases when we increase the **"$h$"**

and takes a maximal value in the vicinity of the critical

Temperature T = 289 K. The results indicate that the $MnFe_4Si_3$ is a very good and efficient material for magnetic refrigeration applications.

Finally, in Figure 3.2-8, we studied the variation of ***RCP*** with the applied ***"h"***. From Figure 3.2-8, we find that the ***RCP*** augments monotonically as the magnetic field augments, the ***RCP*** is of $448J.kg^{-1}$ for h=4T, this implies that our system is a favorite candidate for refrigerant cooling.

The parameters associated to the magnetocaloric effect, for example, the ***RCP***, $\Delta \boldsymbol{S_m}$, refrigerant capacity, etc. depend strongly on the applied ***"h"*** and the exchange interaction between Mn and Fe ions.

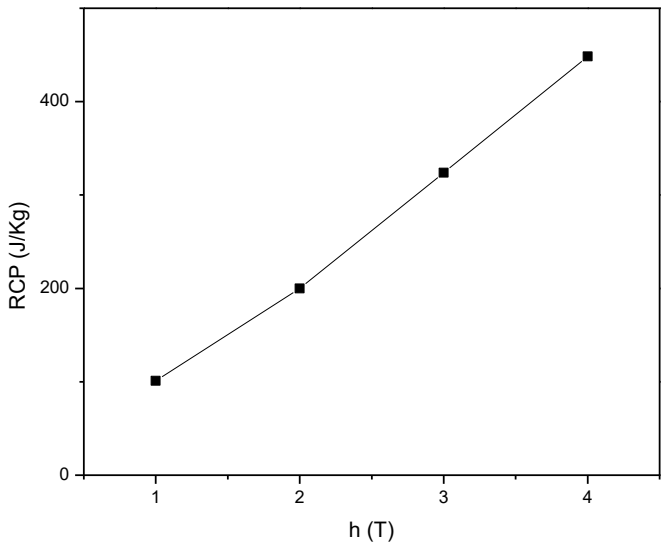


Figure 3.2-8**:** ***h***: external magnetic field dependence of the RCP for $MnFe_4Si_3$

### 3.2.4 Conclusion

The magnetic and magnetocaloric proprieties for $MnFe_4Si_3$were investigated with Monte Carlo simulations. Within the MCS we have been calculated the magnetization and susceptibility from which we deduced the transition temperature $T_C$ = 290K and the $2^{ed}$ order transition from ferro-magnetic to para-magnetic phase. Also, we predicted that the maximum of the critical magnetic behavior and magnetocaloric effect are corresponding to the same transition temperature Tc = 290K.

The magnetic entropy change $\Delta S_m$ reaches the values 1.53, 2.6, 3.68, and 4.53J.($kg^{-1}$. $K^{-1}$) at T=289K when we apply magnetic fields of (1, 2, 3, and 4T), respectively. At T = 0 K each Fe and Mn atom has four possible spin values (-3/2, -1/2, 1/2 and 3/2). Hence, we found eight stable phases, which are (3/2,3/2), (−3/2, -3/2), (-3/2,3/2), (3/2, -3/2), (1/2, -1/2), (-1/2, 1/2), (-1/2, -1/2), and (1/2, 1/2).

The exchange couplings ($J_1$ = 92K and $J_2$ = 20K) correspond to the stable phase (3/2,3/2). Our results are in harmony with the experimental works and solidify the possibility of MnFe4Si3 to be a very promising candidate for the magnetic refrigeration applications.

## 3.3 Study of the frustration in a 2D square lattice: A Monte Carlo study

### 3.3.1 Introduction

The magnetic frustration presents a magnetic order of many systems. To understand this phenomenon many studies were devoted to study the magnetic properties of a square lattices [149-152]. For 2D square lattices, the frustration properties and their aspects such as the ground state (GS) degeneracy, successive phase transitions, and partially disordered phase, re-entrance and disorder lines have been found in exactly solved 2D model [153].

The presence of frustrating interactions may destroy the existing long-range order, permits appearing a highly degenerated ground state of these systems. Under certain conditions, this can allow forming fluid like states of matter, called spin liquids, which have an exotic behavior [155]. Nevertheless, in 3D, it is believed that many of these aspects remain in complicated frustrated systems where exact solutions are not available, hence, these general frustrated systems still constitute, a challenge for theoretical physics [154]. The effects of frustration are often unexpected. Furthermore, the frustration in materials can be a result of a competition between the interactions in lattices. Randomly distributed interactions are due to the specific geometry of the systems. Therefore, there are two classes of frustrated systems, namely: (i) Spin-glasses in which frustrations are due to the disorder in these systems. The term, spin-glasses, refers to a type of magnetic ordering. They are neither paramagnetic nor ferromagnetic or anti-ferromagnetic [156-161], in superlattices, Pang et al. confirmed the coexistence of interfacial ferromagnetic and spin glass ordering [157]. Also, the frustration is due to a competition interaction of the lack of long-range order in spin-glasses as well as in meta-stable nature. This is the case for the Ising square lattice when ferromagnetic (FM) and anti-ferromagnetic (AFM) interactions between spins are randomly defined. When we have an odd number of ferromagnetic or anti-ferromagnetic bonds, it is not possible to obtain a configuration for which all interaction energies are minimized. In the second case (ii), the issue of the geometrical frustration is discussed in many studies [162-169]. Where Moessner et al. noticed that the geometrical

frustration takes place when a system of interacting particles is unable to find its lowest energy state [168].

The aim of this work is to study the frustration and the magnetic properties of a system formed by a square lattice, with ferromagnetic and anti-ferromagnetic interactions. We used Monte Carlo simulations for this purpose. Firstly, we elaborated the ground state phase diagrams. Secondly, we discussed the different magnetic properties of this system.

### 3.3.2 Model and method

The opted Hamiltonian of the studied system is given by:

$$H = -J_1 \sum_{<i,k>} S_i S_k - J_2 \sum_{<i,l>} S_i S_l \qquad (3.16)$$

Where $S_\alpha$ denote the spin random variables which take the values ±1/2 (with $\alpha = i, k, l$ ). First summation runs over the first nearest neighbors with the interaction $J_1$>0 or $J_1 < 0$ bonds indicated by continued lines in Figure 3.3-1. The second summation runs over the second nearest neighbors with the interaction $J_2$<0 bonds indicated by discontinued lines (show Figure 3.3-1). In this model, the ground state is depending to the ratio coupling $J_2 / J_1$, and the frustration phase is found only for ($J_2 / J_1$ = -0.5 and $J_2 / J_1$ = +0.5).

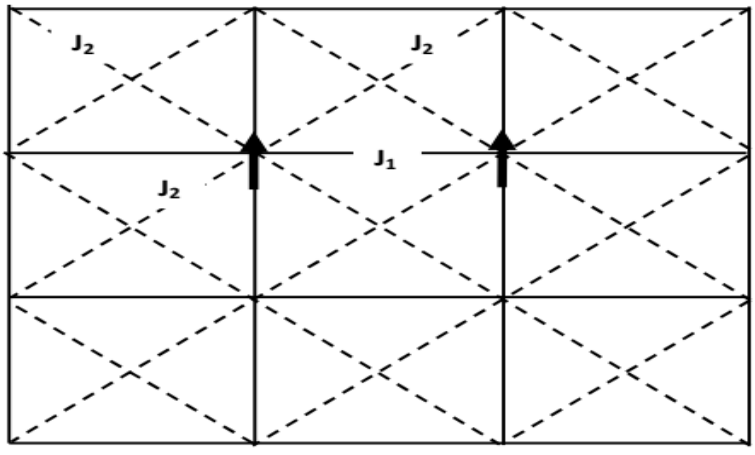


Figure 3.3-1: Fully frustrated simple square lattice discontinued (continued) lines are anti-ferromagnetic and ferromagnetic couplings, respectively.

### 3.3.3 Results and discussion

In current section, we will elaborate the ground state phase diagram (T=0K). On the other hand, we will investigate using Monte Carlo simulation the magnetic properties of such a system at T > 0 K, for the cases: ferromagnetic (FM), anti-ferromagnetic (AF) and super anti-ferromagnetic (SAF) phases. The super anti-ferromagnetic (SAF) phase is described by the ground states consists of alternating lattice rows of the up and down spins.

#### 3.3.3.1 Ground state phase diagram

We determine the ground state phase diagram for various parameters ($J_1$, $J_2$) where we computing and comparing all possible configuration energies from the Hamiltonian (1). Indeed, the Hamiltonian (1) can produce many stable topologies corresponding to different phase diagrams. All accessible phases is obtained by minimizing the energy value for fixed values of the parameters: $J_1$ and $J_2$. The corresponding phase diagram is illustrated in Figure 3.3-2.

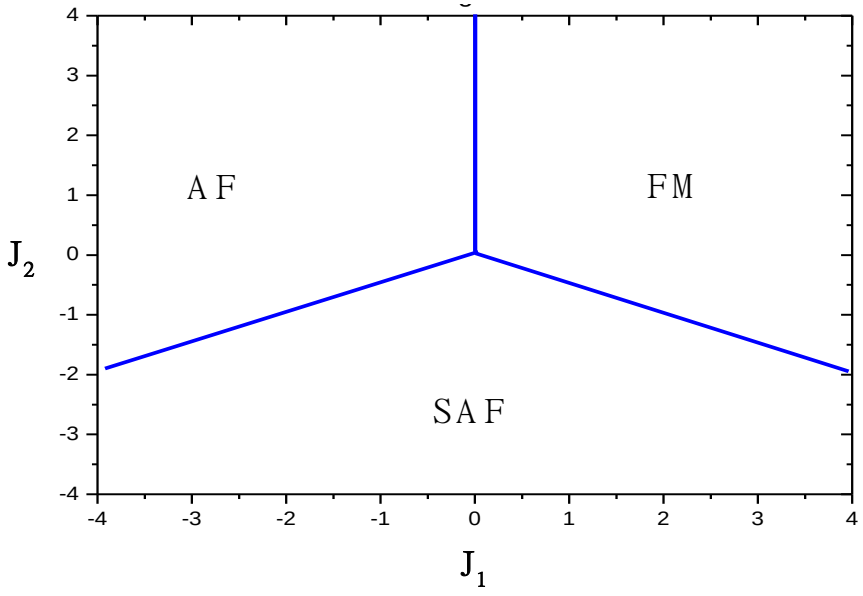


Figure 3.3-2: The ground state phase diagram of the studied system in the plane ($J_1$, $J_2$).

The possible configurations are found to be stable, namely: (i) the ferromagnetic phase (FM), (ii) the anti-ferromagnetic phase (AF) and (iii) the super anti-ferromagnetic phase (SAF). From this figure, it is found that the ferromagnetic phase is stable for $J_1>0$, $J_2>0$ and $J_2/J_1>-0.5$ where $J_1>0$.

The super anti-ferromagnetic phase is stable for $J_2$ negative and specific values of $J_1$. Finally, the anti-ferromagnetic phase (AF) is stable for $J_1<0$ and $J_2>0$, and $J_2/J_1<0.5$, where$J_1$ and $J_2$ are negative. This situation is found when the ferromagnetic (FM) and the anti-ferromagnetic (AFM) interactions are randomly obtained.

#### 3.3.3.2 Monte Carlo study (T > 0 K)

The size of our system is N x N = 45 x 45 spins. We will limit our interest to the two domains where $J_1 > 0$ and $J_1 < 0$. To evaluate the optimal solution for ferromagnetic, anti-ferromagnetic and super anti-ferromagnetic phases, we compare their free-energies. The stable solutions correspond to the minimums of these free energies.

The equations used to calculate the total magnetization moment for each phase are given by:

$$m_{FM} = \frac{1}{N\times N} <\sum_i Si > \quad (3.17)$$

$$m_{AF} = \frac{1}{N\times N} <\sum_j Sj > \quad (3.18)$$

$$m_{SAF} = \frac{1}{N \times N}(< \sum i Si >_a - < \sum j Sj >_b) \quad (3.19)$$

Where *N* represent size of lattice, a and b denoted sublattices of system.

In fact, in Figure 3.3-3 we show the obtained phase diagram. This figure illustrates the second-order as well as first-order transitions. The second-order transition is found for different values of coupling ratio $\frac{J_2}{J_1}$. We found three phases: the ferromagnetic phase (FM), the paramagnetic phase (P) and the super anti-ferromagnetic phase (SAF), Figure 3.3-3, from Figure 3.3-3, we predicted the frustrated phase when ($J_2$ / $J_1$ = -0.5). The transition from the (SAF) to (FM) phase is of the first order type at T= 0.1 K and this fact is occurred where $J_2$ / $J_1$ = -0.5, see Figure 3.3-4.a, Whereas the transitions from the phase (SAF) to the phase (P) and from the phase (FM) to the phase (P) at T=0.4 K, are of the second order type, see Figure 3.3-4.b, these results are confirmed by phase diagram. On the other hand, from the phase diagram we conclude that the critical temperature $T_C$ related to phase transition between (SAF) and (P) phase, or (FM) and (P) phase increase proportionally as function of increasing ratio coupling $J_2$ / $J_1$.

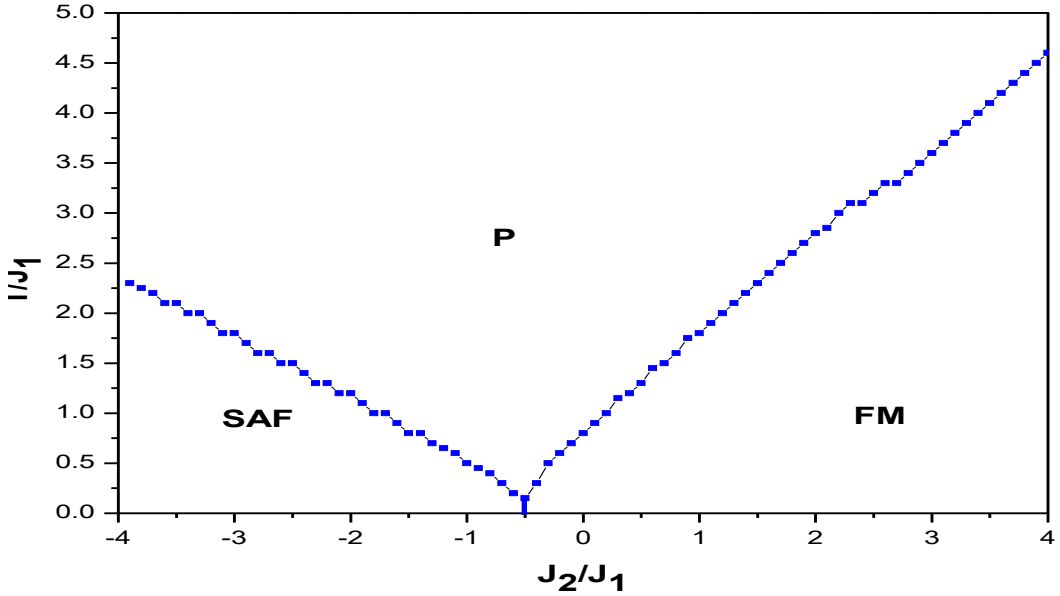


Figure 3.3-3: Phase diagram of the studied system in the plan ($T/J_1$, $J_2/J_1$) for the case $J_1$=+1.

Figure 3.3-4.a

Figure 3.3-4.b

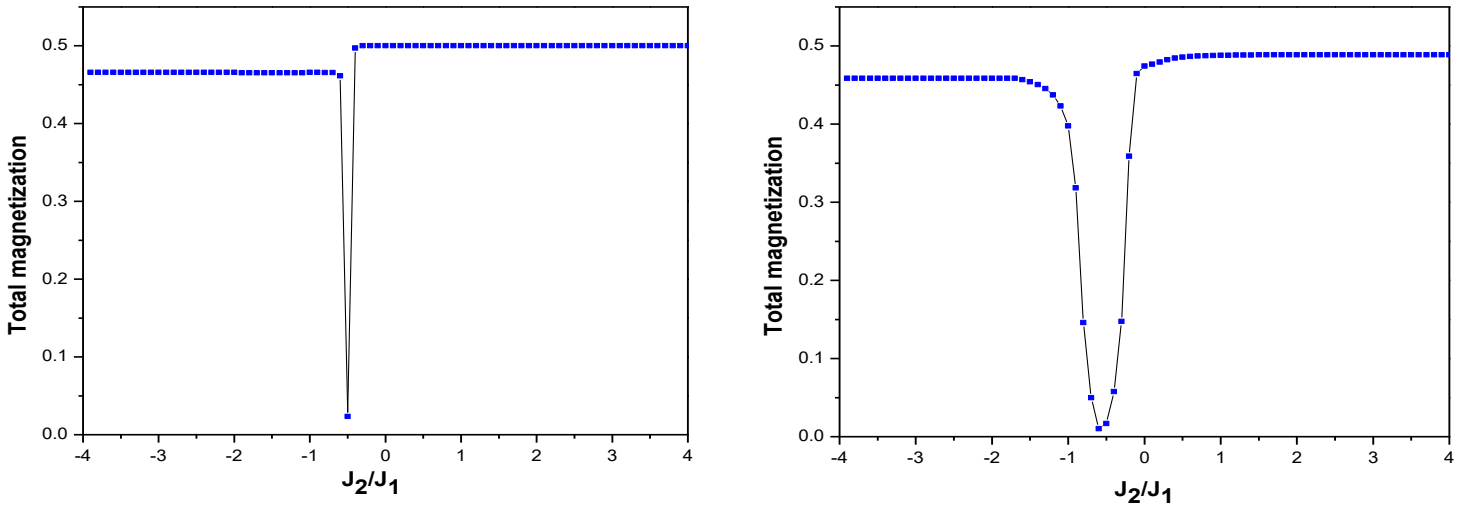


Figure 3.3-4: Total magnetization as a function of the ratio of coupling $J_2/J_1$ at fixed temperature in (a) T=0.1, in (b) T=0.4.

In order to study the anti-ferromagnetic phase (AF) paramagnetic phase (P) and the super anti-ferromagnetic phase (SAF), we plotted in Figure 3.3-5 the corresponding phase diagram, here, we have a frustrated phase when ($J_2$ / $J_1$ = 0.5). Comparing Figure 3.3-3 and Figure 3.3-5, it is found that the phase paramagnetic phase (P) is present in these two figures.

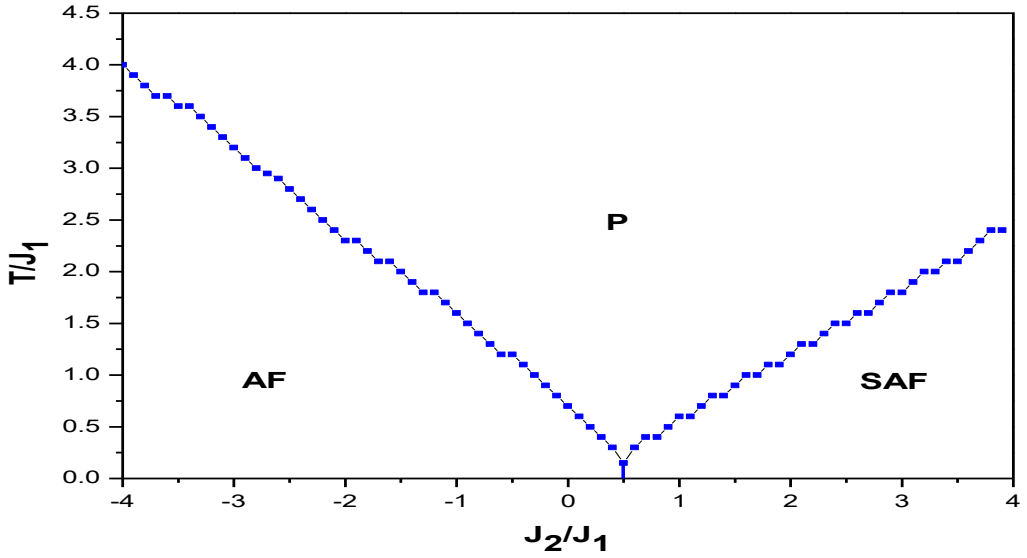


Figure 3.3-5: Phase diagram of the studied system in the plan ( $T/J_1$, $J_2/J_1$ ) for the case $J_1 = -1$.

The phase super anti-ferromagnetic (SAF) is dominant for large values of the ratio J2/J1, whereas the phase ferromagnetic (FM) is stable for J2/J1>-0.5 and. Besides this, the phase anti-ferromagnetic (AF) is found to be stable for J2/J1<0.5. This is due to the sign of the coupling interaction J1 and also the values of the ratio coupling J2/J1, see Figure 3.3-5. In Figure 3.3-6.a, we show that the transition from phase (SAF) to the phase (AF) is of first order type, then, the transitions from the phase (SAF) to the phase (P) and from the phase (AF) to the phase (P) are of the second order type, see Figure 3.3-6.b. Likewise, the critical temperature Tc increase proportionally as function of ratio coupling J2 /J1.

Figure 3.3-6.a

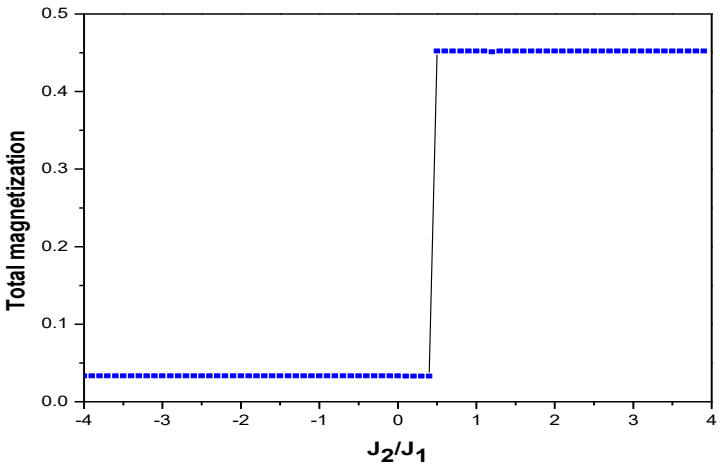


Figure 3.3-6.b

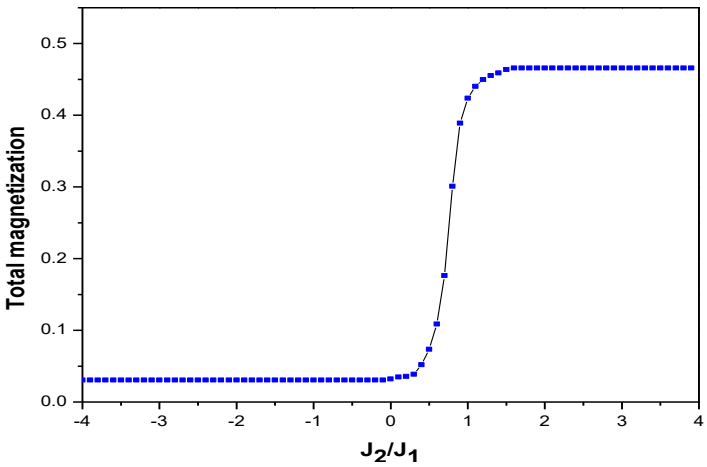


Figure 3.3-6: Total magnetization as a function of the ratio of coupling ($J_2/J_1$) at fixed temperature in (a) T=0.1, in (b) T=0.4.

Finally, in Figure 3.3-6 (a, b, c) we plotted the magnetization versus the external magnetic field. Figure 3.3-6.a presents the hysteresis loop for ($J_2/J_1$=-0.7) and ($T/J_1$=0.1). We show that the hysteresis loop is closed because the value ($J_2/J_1$=-0.7) belongs to the SAF phases. Figure 3.3-6.b illustrates the hysteresis loop for different values of the exchange coupling ($J_2/J_1$=-0.1) and ($J_2/J_1$=-0.2) with ($T/J_1$=0.1). According to this figure, the exchange coupling increases the area of the hysteresis loops and it becomes narrow because this value of the exchange coupling approaches the frustrate phases. From Figure 3.3-6.c, the hysteresis loop for frustrate phases presents double circles in this case.

Figure 3.3-7.a

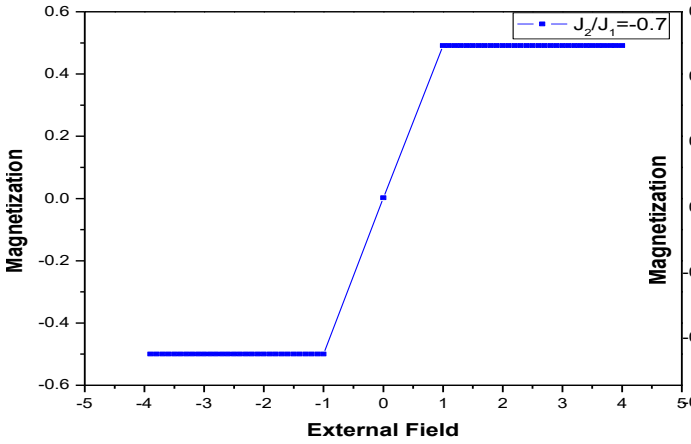


Figure 3.3-7.b

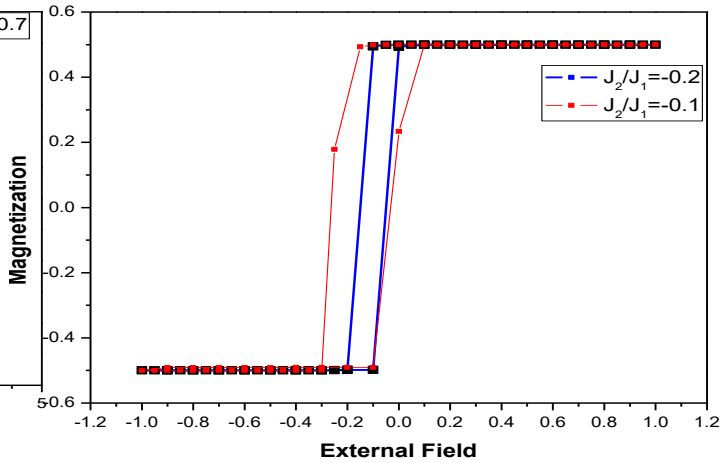


Figure 3.3-7.c

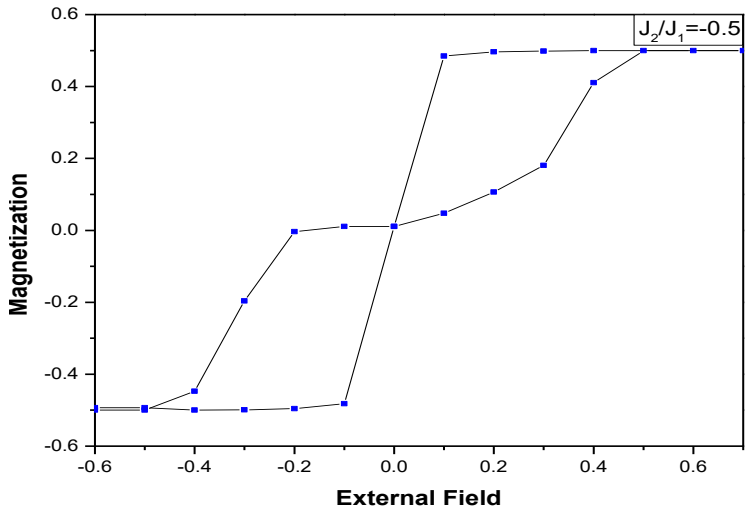


Figure 3.3-7: hysteresis loops as a function of the external field with ($T/J_1$= 0.1).

Figure 3.3-7.a : for ($J_2/J_1$ = -0.7) connected to SAF phases.

Figure 3.3-7.b : for different exchange coupling ($J_2/J_1$ = -0.1, -0.2) connected to FM phases

Figure 3.3-7.c : for ($J_2/J_1$= -0.5) with frustrate phases

### 3.3.4 Conclusion

Using Monte Carlo simulation, we have studied the magnetic properties of a system formed by square lattice with ferromagnetic and anti-ferromagnetic interactions in 2D. We have elaborated the ground state of the phase diagram in the plane ($J_1$, $J_2$), then, we have three stable configurations are: ferromagnetic (FM), antiferromagnetic (AF) and super antiferromagnetic (SAF) as well as the frustrated phases when ($J_2$ / $J_1$ = -0.5 and $J_2$ / $J_1$ = +0.5), this ratio coupling depending on the interaction coupling between the $1^{st}$ and $2^{nd}$ nearest neighbors. It is found that for low reduced temperature values, the magnetizations are found to be in good agreement with the corresponding ground state phase diagram and the transitions between different phases are appear the first transition or the second transition.

## 3.4 Investigation on (*molybdenum-doped-$SnO_2$*) for potential use in magnetoelectronic applications: the DFT framework

### 3.4.1 Introduction

Diluted-magnetic-oxides (DMO) are compounds based on the typical types of systems ($ZnO_2$, $SnO_2$, $TiO_2$, ZnO…) [170-171]. The Molybdenum-doped $SnO_2$ thin film is a functional compound for: optoelectronic, infrared coating, solar cells and other technological uses [172]. Also, tin oxide is a promised diluted magnetic semiconductor for leading edge characteristics to chemical sensing and other applications [173].

With diverse electrical and optical properties, tin oxide, is adequate for photovoltaic and thin solid films. It can be (doped and co-doped) with (Rh, W, Cu,Fe, Cr, Co, Mn…) [174-177]. For tin oxide, the ***"110"*** is among the most studied surfaces [178-182]. Wang et al. noticed that oxygen partial pressure and substrate size severely influence the magnetism of the chromium-doped-$SnO_2$ film engineered by pulsed laser deposition technique (PLD) [183]. On the one hand, the anion sites doped by the (2p orbital) elements can induced the high-Curie-temperature-ferromagnetic behavior in some systems such as sulfides, nitrides and oxides [171, 183-184]. On the second hand, to induce the magnetism, is useful to introduce the holes within valence band after incorporated (cations with lower-valence) or incorporated (anions with weak-electronegativity) as described in ref [171]. For that, our study consists of 2% of the Mo-doped-$SnO_2$ system.

The small amount of Mo is found optimal in many studies related to others fields [172, 185]. According Turgut et al. tin oxide thin films with various molybdenum amount (0 - 3.5at.% with 0.5 at.%step) grown successfully by spray pyrolysis and characterized as a function of molybdenum amount, where XRD analysis confirms that the films of the $SnO_2$ having the cassiterite structure with "***211***" orientation and the favor crystal properties is practical for 2% at molybdenum-doped sample[172].

Morales et al. cited in an experimental work that a small amount of Mo doped $SnO_2$ improves its

electrochemical cycling performance as cathode material for secondary Li-batteries operating in the (1.0-0.0 V) voltage range [185].

Dalui et al.[186] have studied the structural, optical, and magnetic properties of the (Co, Mo) co-doped $SnO_2$, where the band-gap narrows considerably, this observation, probably due to the higher oxidation state of the molybdenum as compared with tin, and consequently to the enhancement of the ( $e^-$ - $e^-$ and $e^-$ - impurity) scattering [186]. Moreover, (Mo, Sb and F) also can be doped in $SnO_2$ matrix to obtain better electrical property [187].

For $SnO_2$ system, many studies based on density-functional-theory: DFT occurred. Zhang et al.[188] have considered the cobalt-doped-$SnO_2$ thin film for the surface magnetism ***"110"*** within WIEN2k-package, which based on full-potential-linearized-augmented-plane-wave approximation. In that study, the Co[3d]and O[2p] having a strong hybridization, this fact could be the responsible for the ferromagnetic coupling.

Wang et al. [189] employed the DFT within Spanish-Initiative-for-Electronic-Simulations-with-Thousands-of-Atoms: SIESTA package, for iron, vanadium, cobalt and manganese doped tin oxide surface layers. The cobalt and iron induced the ferromagnetism in $SnO_2$, where the paramagnetism is stated with vanadium and manganese.

The current work considered the calculations based on Korringa-Kohn-Rostoker approximation method combined with Coherent Potential Approximation (KKR-CPA) method employing the local density approximation (LDA) parameterization implemented in MACHIKANEYAMA 2002V09 package in order to investigate the effect of Mo-doped $SnO_2$ on the magnetism behavior as well as the Curie temperature.

### 3.4.2 Crystal properties and density-functional-theory: DFT framework

The $SnO_2$ rutile is fit in the space **group $P4_2/mnm$**, it is **a** tetragonal **structure: (*a*=*b*=**4.7373 and ***c*** =3.1864) Å [190]. Then, this system attributed by N°136 according the **international tables of X-Ray-crystallography. The *Wyckoff-positions* are 2a and 4f which stand for tin and oxygen, respectively, see** Figure 3.4-1**.**

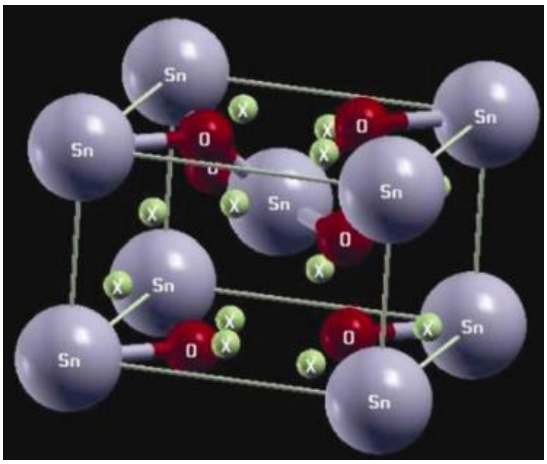


Figure 3.4-1: The tetragonal structure of $SnO_2$ unit cell, $\boldsymbol{a}$=$\boldsymbol{b}$=4.7373 and $\boldsymbol{c}$ =3.1864 Å with $\boldsymbol{\alpha}$ =$\boldsymbol{\beta}$ =$\gamma$=90°. ***Sn***, ***O*** and ***inter sites*** are *gray*, *red* and *green*, respectfully.

**For the present work, we considered** $Sn_{0.98}Mo_{0.02}O_2$ system, and the DFT framework within MACHIKANEYAMA2002V09 package based on Korringa-Kohn-Rostoker: KKR method [191-192] in order to understand the magnetoelectronic behavior when the Mo is incorporated.

In KKR CPA method, we consider the unit cell with percentage doped impurity instead the supercells. **Also,** the parameterization of Moruzzi-Janak-Williams employed in this work indicated as Local-Density-Approximation: LDA [193]. Within the output parameters of MACHIKANEYAMA2002V09 package, we situated the **inter sites (Z=0) relative to $SnO_2$ rutile (8 sites) at** ($\frac{1}{2}$,0,-0.1682); (0, $\frac{1}{2}$ ,-0.1682);(0, $\frac{1}{2}$,0.1682);($\frac{1}{2}$,0,0.1682);(-0.3125,0.3125,0);(-0.1875,-0.1875,0.3363); (0.1875,0.1875,0.3363); (0.3125,-0.3125,0), **see** Figure 3.4-1.

For the irreducible part of the first-Brillouin-zone, **our calculation is** up to 460K-point. The employed scalar relativistic approximation and the potential form is limited to the muffin-tin-spheres, and expanded with real harmonic up to the angular momentum = 2 for each site. The MACHIKANEYAMA2002V09 package is applicable for this investigation [194]. For the pure $SnO_2$, the-density-of-states: DOS is presented in Figure 3.4-2, there is no evidence of magnetism, since the DOS is symmetrical. The observed energy band gap is $E_g$=2.0481eV, where this value is 3.6eV according the experiment [171]. The band gap is not in total agreement with experimental one due to the employ of a potential which is the same for all orbitals which can

lead in semiconductors and insulators materials.

By the mean-field-approximation, the Curie-temperature is evaluated [195-197]

With $T_C = \frac{2}{3K_\beta} * \frac{E_{DLM} - E_{ferro}}{C}$ [198-201]

*K* : Boltzmann constant .

*C*: the amount concentration.

$E_{DLM}$: disordered-local-moment energy and the DLM state is belongs to anti-ferromagnetic stability.

$E_{ferro}$: ferromagnetic energy.

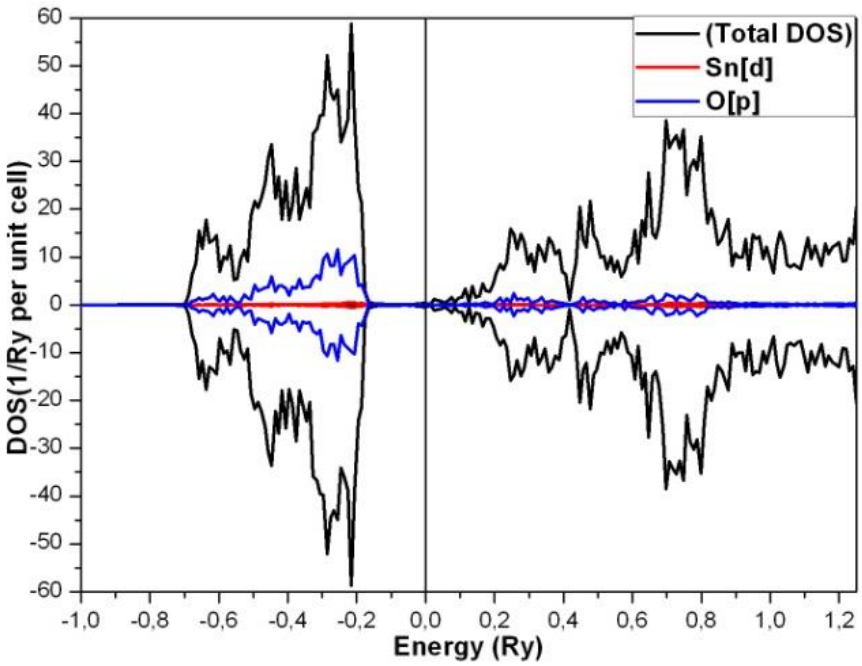


Figure 3.4-2: The-**D**ensity-**O**f-**S**tates of $SnO_2$ related to the Fermi energy. Total DOS, Sn[3d] and O[2p] are black red and blue, respectively

### 3.4.3 The magnetism behavior in $Sn_{0.98}Mo_{0.02}O_2$ system.

We have plotted the-density-of-states: DOS to understand the system of the $Sn_{0.98}Mo_{0.02}O_2$ in terms of the electronic structure. The Figure 3.4-3 illustrating the total and the partial: DOS, noticed TDOS and PDOS, respectively. This figure shows the half-metallic behavior: the Mo-doped $SnO_2$ induced a new state on the Fermi level and resulting the ferromagnetic stability. The majority and the minority spins are connected to ($t_{2g}^{+}$, $e_g^{+}$) and ($t_{2g}^{-}$, $e_g^{-}$) states, respectively, see Figure 3.4-3. Where the $t_{2g}^{+}$(Mo) state is around the Fermi level at 0 Ry, therefore, the half-metallic is predicted, since that band of conduction electron is found with 100% polarized at the up side of the Fermi energy. At this point we conclude that $Sn_{0.98}Mo_{0.02}O_2$ is belonging to the ferromagnetic: FM order. This feature is searched and applicable in spintronic devices [171, 195, 198].

These characters are elucidated by the hybridization between the orbital:[4d] of molybdenum and the nearest neighbors of the orbital:[2p] of oxygen. Therefore, it is the exchange-mechanism of ***"p – d"*** interaction, which is induced the ferromagnetism for $Sn_{0.98}Mo_{0.02}O_2$. From Figure 3.4-3, we observe in $Sn_{0.98}Mo_{0.02}O_2$ system that the crystal-field-splitting between ($e_g$ and $t_{2g}$ states) is larger than the exchange-splitting between ( $e_g^{+}$ and $e_g^{-}$states).

The Mo[4d] is divided in two states, which are $e_g(d_{x-y}^2)$ and $t_{2g}(d_{xy}, d_{yz}, d_{xz})$, respectively the high and low energy due to electronic field created by six ligands "octahedral crystal field". For Mo-doped $SnO_2$, we predict a decrease in energy gap: $E_g$, since, Mo($4d^5 5s^1$) having 6 valence electrons, the $Mo^{4+}$($4d^2$) has only two net electrons in $Sn_{0.98}Mo_{0.02}O_2$ system. Hence, the Coulomb-correlation-interaction (within $Mo^{4+}$and $O^{2-}$) would produce the difference in the gap. For the Jahn-Teller-effect, we observe a splitting for $t_{2g}$(Mo) and $e_g$(Mo), subsequently, the repulsion is weak between the cation and anion, $Mo^{4+}(t_{2g}^2 e_g^0)$ and $O^{2-}$, respectively. After that, the distance of the metal oxide is inferior to spherical-electronic-density case and the "***c***" parameter reduced.

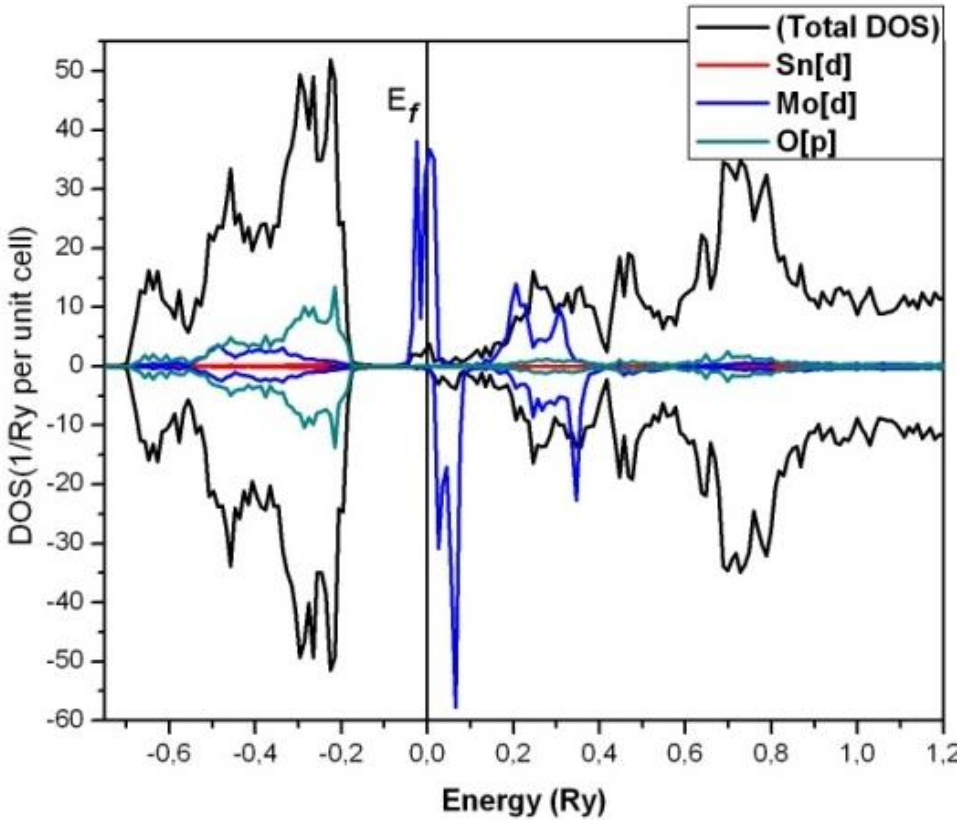


Figure 3.4-3: The-**D**ensity-**O**f-**S**tates of $Sn_{0.98}Mo_{0.02}O_2$ related to the Fermi energy. Total DOS, Sn[3d], Mo[4d] and O[2p] are black, red, blue and green, respectively

The total-energy-difference: $\Delta E$ is expressed by $\Delta E = E_{DLM} - E_{ferro}$, where the $E_{DLM}$ and $E_{ferro}$ stand for disordered-local-moment and ferromagnetic energies, respectfully. Within ΔE, we can verify the ferromagnetic stability. The ferromagnetic state in which (all spins) of the doped element (Mo) have one direction ($Sn_{0.98}Mo^{\uparrow}_{0.02}O_2$) where the disordered-local-moment state in which (half of the impurity ion spins) point to the up: Mo(↑) direction and the rest points to the down: Mo(↓) orientation as simulated by ($Sn_{0.98}Mo^{\uparrow}_{0.01}Mo^{\downarrow}_{0.01}O_2$) model, the DLM state is belongs to anti-ferromagnetic stability. The obtained total energy difference is $\Delta E$ = 7.080*10$^{-5}$ Ry > 0. This value verifies the ferromagnetic presence since $\Delta E$ > 0. With $T_C = \frac{2}{3K_\beta} * \frac{E_{DLM} - E_{ferro}}{C}$, the calculated value is of 372.78 K, the predicted $T_C$ would be adequate at room-temperature for spinotronic applications. For the magnetic properties, we observed value of the

total-magnetic-:moment: $M^{Total}(\mu_B)$ is of 0.07621 $\boldsymbol{\mu_B}$, see Table. 1. The main involvement to the moment is from Mo component with $\mathbf{M^{Mo}}$=1.26324 $\boldsymbol{\mu_B}$ where $\mathbf{M^{Sn}}$ and $\mathbf{M^{O}}$ are neglected, these characteristics could be make the present studied system as a potential matter in magnetoelectronic at adequate room-temperature.

Tableau 2: Energies, magnetic moments and Curie temperature $T_C$ $Sn_{0.98}Mo_{0.02}O_2$

| | $E_{ferro}$(Ry) | $E_{DLM}$(Ry) | $E_{DLM}$ - $E_{ferro}$ (Ry) | $T_C$ (K) | $M^{Total}$ ($\mu_B$) | $M^{Sn}$ ($\mu_B$) | $M^{Mo}$ ($\mu_B$) | $M^{O}$ ($\mu_B$) |
|---|---|---|---|---|---|---|---|---|
| $Sn_{0.98}Mo_{0.02}O_2$ | -25114.6199333 | -25114.6198625 | 7.080*10$^{-5}$ | 372.78 | 0.07621 | 0.00110 | 1.26324 | 0.00124 |

### 3.4.4 Conclusion

For the considered systems, the density-functional-theory: DFT framework within MACHIKANEYAMA2002V09 package occurred. The FM stability is observed, since the majority-spin of $t_{2g}^{+}$(Mo) state is around the Fermi level at 0 Ry and 100% spin polarized, the half-metallic behavior is useful in magnetoelectronic applications.

The FM stability is verified within the total energy difference. The mean-field approximation enabled us to predict that $Sn_{0.98}Mo_{0.02}O_2$ system has a useful $T_C$ and can promise the uses on this system in adequate room-temperature.

# General Conclusion

The aim of this work is adding a value in the scientific research, namely: Magnetic refrigeration and spintronic application. These two-research fields have been theoretically investigated and discussed.

Within Monte Carlo and Ab initio simulations, we have studied the magnetic and electronic properties of the **FeS** compound in the framework of spintronic application. We have employed Monte Carlo simulation to study and analyze the magnetic properties and the magneto caloric effect of the $\mathbf{MnFe_4Si_3}$ alloy as magnetic refrigeration materials. The results found are according and validated by experimental data. The main conclusions in this work are as follows:

In Part I, we describe the basic concepts of Ab-initio method and Monte Carlo simulation. We have started by demonstration of theoretical formalism of Ab initio method and the Density Functional Theory. It is a method of quantum computing for accurately studying the electronic structure.

We have described two approaches for the application of this theory, namely; the approximation of the pseudo-potential (PW) and "Full Potential Linearized Augmented Plane Wave (FP LAPW)" method. For the Monte Carlo method, we have throwing a study of Ising model and then we have presented the principal notions of the static Monte Carlo simulation. Finally, we have described some algorithms used in the framework of the Ising model.

In Part II we started by presenting and discussing the basic pillars of Spintronic.

We investigated the giant magneto-resistance and the tunnel magnetoresistance. NV-MRAM has been given and discussed as an application in the area of Spintronic, principally in information storage. Then we exposed the magnetic properties of the materials such as the origin of

magnetism and the type of magnetic order in magnetic materials. Then, we have discussed the different types of transition temperatures as well as the Néel classification of magnetism, in addition, the crystal field theory and magnetic anisotropy and hysteretic properties of magnetic materials has been provided. In the rest of this part, we broached the magneto caloric effect subject. Firstly, we have introducing the short history and the origin of the magneto caloric effect. Then, we have treated the magneto caloric properties and the magnetic refrigeration. We have discussed and established the different cycles used in the magnetic refrigeration and we have closed this part by analyzing and treating the **$MnFe_4Si_3$** compound.

Part III of this thesis consists of four axis. In the first axis, we have investigated the electronic and magnetic properties of **FeS** compound by first principle and Monte Carlo simulations. Using DFT calculations, we predicted the total and partial DOS, energies and the coupling interactions between $J_{Fe\text{-}Fe}$ in different directions, spin moment. We calculated the minimum energy and we deduced that this is corresponds to the AFM A-type state. Then we employed the Monte Carlo simulation based on Metropolis algorithm and spins Hamiltonian in the framework of Ising model to study phase diagram and magnetization properties.

At (T = 0 K) we established the phase diagram configuration, consequently, we found two stable phases which are (m = ±2) and (m = 0). For (T > 0 K), we have investigated the magnetic properties for different system sizes which have exhibited second-order phase transitions at $T_N$ = 450K.

In the second axis, we have studied the magnetic and magneto caloric properties of the **$MnFe_4Si_3$** alloy using the Monte Carlo simulation. Employing Monte Carlo simulation in the framework of Ising model we have been investigated the magnetic properties from which we determined the transition temperature $T_C$ = 290K and we concluded that the transition from Ferro-magnetic to para-magnetic phase shows as $2^{ed}$ order transition. In addition, we predicted that the maximum of the critical magnetic behavior and magnetocaloric effect are corresponding to the same transition temperature Tc = 290K.

The magnetic entropy change $\Delta S_m$ reaches the values 4.53J.($kg^{-1}$. $K^{-1}$) at T=289K when we apply magnetic field $h = 4T$. At T = 0 K each Fe and Mn atom has four possible spin values (±3/2 and ±1/2). Hence, we found eight stable phases, which are (3/2,3/2), (−3/2, -3/2), (-3/2,3/2), (3/2, -3/2), (1/2, -1/2), (-1/2, 1/2), (-1/2, -1/2), and (1/2, 1/2).

The exchange couplings ($J_1$ = 92K and $J_2$ = 20K) correspond to the stable phase (3/2,3/2). Our results present a good agreement with the experimental works and solidify the possibility of MnFe4Si3 to be a very promising candidate for the magnetic refrigeration applications.

In third axis, we have used Monte Carlo Simulation method to study the magnetic frustration in 2D square lattice. We examined the frustration due to couplings competitions ($J_1$, $J_2$) between the 1st and 2nd nearest neighbors, we have elaborated the ground state of the phase diagram in the plane ($J_1$, $J_2$), then, we founded three stable configurations are: ferromagnetic (FM), antiferromagnetic (AF) and super antiferromagnetic (SAF), likewise the frustrated phases occurred at ($J_2$ / $J_1$ = -0.5 and $J_2$ / $J_1$ = +0.5), this ratio coupling depending on the interaction coupling between the 1st and 2nd nearest neighbors. It is found that for low reduced temperature values, the magnetizations are found to be in good agreement with the corresponding ground state phase diagram and the transitions between different phases are appear the first transition or the second transition.

Finally, in the DFT framework we have presented an investigation on molybdenum-doped-$SnO_2$ for potential use in magnetoelectronic applications. We observed the FM order, since the majority-spin of $t_{2g}^{+}$(Mo) state is around the Fermi level at 0 Ry and 100% spin polarized, the half-metallic behavior is useful in magnetoelectronic applications.

The FM stability is verified within the total energy difference. The mean-field approximation enabled us to predict that $Sn_{0.98}Mo_{0.02}O_2$ system has a useful $T_C$ and can promise the uses on this system in adequate room-temperature.

# References


[1] M. Born, J. R. Oppenheimer, Annalen der Physik, 389 (1927) 457–484

[2] P. Baranek, G. Pinarello, C. Pisani , R. Dovesi, Phys. Chem. Chem. Phys, 2 (2000) 3893-3901

[3] S. Casassa, A. Ferrari, M. Busso, and C. Pisani. J. Phys. Chem. B, 106 (2002) 12978-12985

[4] A. Szabo, N. S. Ostlund, Modern Quantum Chemistry, 1982

[5] P. Pulay, S. Saebø, Theor. Chim. Acta, 69 (1986), 357-368

[6] G. E. Scuseria, Chem. Phys. Lett, 176 (1991) 27-35

[7] L. H. Thomas. Math. Proc. Cambridge Philos. Soc, 23 (1927) 542

[8] E. Fermi. Z. Phys, 48 (1928) 73-79

[9] P. Hohenberg, W. Kohn. Phys. Rev, 136 (1964) B864

[10] W. Kohn , L. J. Sham, Phys. Rev, 140 (1965) A1133

[11] P. A. M. Dirac. Proc. Cambridge Phil. Roy. Soc., 26 (1930) 376

[12] W. Kohn, Rev. Mod. Phys, 71 (1999) 1253

[13] C. S. Wang, B. M. Klein, H. Krakauer, Phys. Rev. Lett, 54 (1985) 1852

[14] T. C. Leung, C. T. Chan, B. N. Harmon, Phys. Rev. B, 44 (1991) 2923

[15] J. P. Perdew, K. Burke, M. Ernzerhof, Phys. Rev. Lett, 77 (1996) 3865

[16] A. D. Becke, Phys. Rev. A, 38 (1988) 3098

[17] F. Tran, P. Blaha. Phys. Rev. Lett, 102 (2009) 226401

[18] A. D. Becke, E. R. Johnson, J. Chem. Phys, 124 (2006) 221101

[19] A. D. Becke and M. R. Roussel. Phys. Rev. A, 39 (1989) 3761

[20] j. Korringa, Physica, 13 (1947) 392-400

[21] W. Kohn, N. Rostoker, Phys. Rev 94 (1954) 1111

[22] K. Inoue, K. Ohtaka, eds. Photonic crystals: physics, fabrication and applications. Vol. 94. Springer, 2013

[23] J. S. Galsin, Impurity scattering in metallic alloys. Springer Science & Business Media, 2012

[24] Y. Kumashiro, Electric refractory materials. CRC Press, 2000

[25] A. Meike, A. Gonis, P. E. Turchi, K. Rajan (2000). Properties of Complex Inorganic Solids 2. Springer. p. 213

[26] S. Blügel, G. Bihlmayer, NIC series, 31 (2006) 85–129 or http://juser.fz-juelich.de/record/50026/files/FZJ-2014-02213.pdf

[27] J. C. Slater, Phys. Rev, 81 (1951) 385

[28] O. K. Andersen., Phys. Rev. B, 12 (1975) 3060

[29] D. D. Koelling, G. O. Arbman, J. Phys. F: Metal Phys, 5 (1975) 2041

[30] E. Sjöstedt, L. Nordström, and D. J. Singh. Solid State Commun, 114 (2000) 15–20

[31] P. Blaha, K. Schwarz, G. Madsen, D. Kvasnicka, and J. Luitz, WIEN2k, Augmented Plane Wave + Local Orbitals Program for Calculating Crystal Properties, Vienna, Austria, 2001. See also: http://www.wien2k.at

[32] W. Lenz, Physikalische Zeitschrift **21** (1920).

[33] E. Ising, Z. *Phys.* **31**, 253 (1925).

[34] R. B. Potts, *Proc. Camb. Phil. Soc.* **48**, 106 (1952).

[35] J. Ashkin and E. Teller, *Phys. Rev.* **64**, 5 (1943).

[36] C. Domb, *Phase Transitions and Critical Phenomena*, (Eds.) M. S. Green, J. Lebowitz, and C. Domb, London: Academic Press **1-20**, 1974 (2000).

[37] M. Yeomans, *Statistical Mechanics of Phase Transitions*, Oxford: Oxford University Press, (1993).

[38] H. E. Stanley, *Phys. Rev. Lett.* **20**, 589 (1968).

[39] R. J. Baxter, *Exactly solved models in statistical mechanics*, San Diego: Academic Press Inc. (1982).

[40] *G. Gallavotti, Statistical mechanics, Texts and Monographs in Physics, Berlin: Springer-Verlag (1999).*

*[41] L. Onsager, Physical Review, Series II **65** (3–4), 117 (1944).*

[42] D. W. Hubbard, *The Failure of Risk Management: Why It's Broken and How to Fix It, (eds.) J. willy and Sons, New Jerzy (2009).*

[43] D. P. Landau and K. Binder, *A Guide to Monte Carlo Methods in Statistical Physics*, Cambridge: Cambridge University Press (2000).

[44] M. E. J. Newman and G. T. Barkema, *Monte Carlo Methods in Statistical Physics*, Oxford: Clarendon Press (1999).

[**45**] N. *Metropolis, A.W. Rosenbluth, M.N. Rosenbluth, A.H. Teller, and E. Teller, Journal of Chemical Physics **21** (6), 1087 (1953).*

[46] W. Janke, *Computational Many-Particle Physics, in: Lect. Notes Phys*, (eds.) R. Schneider, A. Weisse, and H. Fehske, Berlin: Springer, 739 (2008).

[47] H. E. Stanley, *Introduction to Phase Transitions and critical phenomena*, Oxford: Oxford University Press (1971).

[48] O. Kahn, J.S. Miller, F. Palacio D. Gatteschi, *Magnetic Molecular Materials*, Plenum: NATO ASI E, 198 (1991).

[49] P. Weiss, *J. Phys. Radium* **6**, 661 (1907).

[50] R. Honmura and T. Kaneyoshi, *J. Phys. C: Solid State Phys.* **12**, 3979 (1979).

[51] N. Boccara, *Phys. Lett.A* **94**, 185 (1983).

[52] A. Benyoussef and N. Boccara, *J. Appl. Phys.* **55**, 1667 (1985).

[53] K.G. Wilson, *Phys. Rev. B* **4**, 3184 (1971).

[54] J. Oitmaa, *Phys. Lett. A* **33**, 230 (1970).

[55] K. Binder and P.C. Hohenberg, *Phys. Rev. B* **9**, 2194 (1974).

[56] *M. Matsumoto and T. Nishimura, ACM Transactions on Modeling and Computer Simulation* ***8*** *(1), 3 (1998).*

[57] R. Glauber, *J. Math. Phys.* **4**, 294 (1963).

[58] U. Wolff, *Phys. Rev. Lett.* **62**, 361 (1989).

[59] W. Lenz, Physikalische Zeitschrift **21** (1920).

[60] E. Ising, Z. *Phys.* **31**, 253 (1925).

[61] Kristen Coyne, E.S. *Giant Magnetoresistance: The Really Big Idea Behind a Very Tiny Tool*.

[62] Tsymbal, E.Y. and D. Pettifor, *Perspectives of giant magnetoresistance.* Solid State Physics, 2001. **56**: p. 113 – 237.

[63] http://simple.wikipedia.org/wiki/Giant_magnetoresistance

[64] Pretzer, L.A., H.J. Song, Y.-L. Fang, Z. Zhao, N. Guo, T. Wu, J.T. Miller, and M.S. Wong. Regulating the Hydrodechlorination Activity of Pd-on-Au Nanoparticles Through Au Particle

Size. in 22rd North American Catalysis Society Meeting. 2011.

[65] Barron, A.R., *Physical Methods in Chemistry and Nano Science.* Connexions: Houston, TX, 2012: p. 365.

[66] Pretzer, L.A., H.J. Song, Y.-l. Fang, Z. Zhao, N. Guo, T. Wu, J.T. Miller, and M.S. Wong. *Hydrodehalogenation activity of Pd-on-Au nanoparticles: A function of Au particle size and Pd surface coverage*. in *Abstracts of Papers of the American Chemical Society*. 2012. AMER CHEMICAL SOC 1155 6TH ST,NW, WASHINGTON, DC 20036 USA.

[67] Zhao, Z., J. Arentz, J. Clomburg, R. Gonzalez, L.A. Pretzer, N. Schweitzer, J.T. Miller, and M.S. Wong. *Modulating palladium-on-gold catalysis for glycerol oxidation with Pd surface coverage*. in *Abstracts of Papers of the American Chemical Society*. 2012. AMER CHEMICAL SOC 1155 16TH ST, NW, WASHINGTON, DC 20036 USA

[68] Zhao, Z. and A. Barron, *Gas Chromatography Analysis of the Hydrodechlorination Reaction of Trichloroethene.* Connexions: Houston, TX, 2012.

[69] Zhao, Z. and A. Barron, *Dynamic Headspace Gas Chromatography Analysis.* Connexions: Houston, TX, 2012.

[70] Pretzer, L.A., H.J. Song, Y.-L. Fang, Z. Zhao, N. Guo, T. Wu, I. Arslan, J.T. Miller, and M.S. Wong, *Hydrodechlorination catalysis of Pd-on-Au nanoparticles varies with particle size.* Journal of Catalysis, 2013. **298**: p. 206-217.

[71] Qian, H., L.A. Pretzer, J.C. Velazquez, Z. Zhao, and M.S. Wong, *Gold nanoparticles for cleaning contaminated water.* Journal of Chemical Technology & Biotechnology, 2013. **88**(5): p. 735-741.

[72] Qian, H., M.S. Wong, Z. Zhao, J. Velazquez, and L.A. Pretzer. *Mitigating Nitrate/Nitrite Water Emissions through Bimetal-catalyzed Reduction*. in *23nd NAM: North American Catalysis Meeting*. 2013.

[73] Wong, M.S., L.A. Pretzer, J. Velazquez, Z. Zhao, and H. Qian. *Synthesizing and*

*Characterizing Catalysts Using Gold Nanoparticles as the Support Material*. in *23nd NAM: North American Catalysis Meeting*. 2013.

[74] Zhao, Z. *Pd-on-Au Surface Coverage Effect on Room-temperature Hydrogen Generation from Formic Acid*. in *23rd North American Catalysis Society Meeting*. 2013. Nam.

[75] Zhao, Z., J. Arentz, L.A. Pretzer, P. Limpornpipat, J.T. Miller, and M.S. Wong. *Modulating the Catalytic Activity and Selectivity of Palladium-Decorated Gold Nanoparticles With Pd Surface Coverage for Glycerol Oxidation*. in *AIChE meeting*. 2013.

[76] Zhao, Z., Y.-L. Fang, P.J.J. Alvarez, and M.S. Wong, *Degrading perchloroethene at ambient conditions using Pd and Pd-on-Au reduction catalysts.* Applied Catalysis B: Environmental, 2013. **140–141**(0): p. 468-477.

[77] Qian, H., Z. Zhao, J.C. Velazquez, L.A. Pretzer, K.N. Heck, and M.S. Wong, *Supporting palladium metal on gold nanoparticles improves its catalysis for nitrite reduction.* Nanoscale, 2014. **6**(1): p. 358-364.

[78] Wong, M.S., H. Qian, Z. Zhao, and L. Pretzer. *Developing metal-on-metal catalysts for nitrate, nitrite and nitrophenol catalytic reduction*. in *247th ACS National Meeting*. 2014.

[79] Zhao, Z., J. Arentz, L.A. Pretzer, P. Limpornpipat, J.M. Clomburg, R. Gonzalez, N.M. Schweitzer, T. Wu, J.T. Miller, and M.S. Wong, *Volcano-shape glycerol oxidation activity of palladium-decorated gold nanoparticles.* Chemical Science, 2014. **5**(10): p. 3715-3728.

[80] Zhou, K., W. Wang, Z. Zhao, G. Luo, J.T. Miller, M.S. Wong, and F. Wei, *Synergistic Gold–Bismuth Catalysis for Non-Mercury Hydrochlorination of Acetylene to Vinyl Chloride Monomer.* ACS Catalysis, 2014: p. 3112-3116.

[81] Eley, D.D. and P. Luetic, *The formic acid decomposition on palladium-gold alloys.* Transactions of the Faraday Society, 1957. **53**: p. 1483-1487.

[82] Visser, C., J.G.P. Zuidwijk, and V. Ponec, *Reactions of hydrocarbons on palladium-gold alloys.* Journal of Catalysis, 1974. **35**(3): p. 407-416.

[83] Sinfelt, J.H., *Catalysis by alloys and bimetallic clusters.* Accounts of Chemical Research, 1977. **10**(1): p. 15-20.

[84] Schwank, J., *Bimetallic catalysts: Discoveries, concepts, and applications. By John H. Sinfelt, John Wiley & Sons, 1983. XI + 164 pp.* AIChE Journal, 1985. **31**(8): p. 1405-1405.

[85] Gretz, E., T.F. Oliver, and A. Sen, *Carbon-hydrogen bond activation by electrophilic transition-metal compounds. Palladium(II)-mediated oxidation of arenes and alkanes including methane.* Journal of the American Chemical Society, 1987. **109**(26): p. 8109-8111.

[86] Thomas, J.M., *Colloidal metals: past, present and future.* Pure and Applied Chemistry, 1988. **60**(10): p. 1517-1528.

[87] Tedrow P M, Meservey R 1971 Spin-dependent tunneling into ferromagnetic nickel. Phys. Rev. Lett. 26, 192–5

[88] happert C, Fert A, Nguyen F 2007 The emergence of spin electronics in data storage. Nat. Mater. 6, 813–23

[89] JPL Publication 13-3 2/13

[90] W. J. Gallagher, S. P. P. Parkin, "Development of the magnetic tunnel junction MRAM

[91] J. M. D. Coey, Magnetism and Magnetic Materials, Cambridge University Press, 2010

[92] R. Thompson, Environmental magnetism, Springer, 2012.

[93] D. D. Stancil, Springer, 1993

[94] Ralf Skomski, Simple Model of Magnetism, Oxford University Press, 2008 and http://www.electronics-tutorials.ws/electromagnetism/magnetic-hysteresis.html.

[95] Miha Marolt, Superparamagnetic materials, University of Ljubljana Faculty of Mathematics and Physics, 2014

[96 ]K. H. J. Buschow et F. R. de Boer, Physics of Magnetism and Magnetic Materials, New

York : Kluwer Academic/Plenum Publishers, 2003.

[97] E.O.Wollan and W. C. Koehler," Neutron diffraction study of the magnetic properties of the series of perovskite-type compound l1xlaxcamno",Rev **100**, (1955) 545.

[98] K. E. Geckeler et H. Nishide, Advanced nanomaterials, John Wiley and Sons, 2009

[99] D. Gubbins et E. H. Bervera, Encyclopedia of geomagnetism and paleomagnetism, Springer, 2007.

[100] C. Kittel, Introduction to solid state physics, Wiley, 2005

[101] J. Bigot, W. Hubner, T. Rasing et R. Chantrell, "Ultrafast Magnetism I", Springer, 2015.

[102] A. Goldman, Modern ferrite technology, Springer, 2006.

[103] Van Vleck, J. (1932). "Theory of the Variations in Paramagnetic Anisotropy Among Different Salts of the Iron Group". *Physical Review*. **41** (1932) 208.

[104] Ronny Knut, New Materials for spintronics, University of Uppsala, 2012.

[105] Fredrik Gustavsson, Properties of Fe/ZnSe Heterostrucutes, University of Uppsala, 2002.

[106] E. Warburg, Ann. Phys. 13, 141 (1881).

[107] V. K. Pecharsky and K. A. Gschneidner, Jr., J. Appl. Phys.**85**, 5365 (1999).

[108] K. A. Gschneidner, Jr. and V. K. Pecharsky, Annu. Rev. Mater. Sci.**30**, 387 (2000).

[109] A. M. Tishin and Y. I. Spichkin. "The magnetocaloric effect and its application: Series in condensed matter physics. Institute of Physics Pub., Bristol and Philadelphia, 2003.

[110] P. Debye, Ann. Phys. 81, 1154 (1926).

[111] W. F. Giauque, J. Amer. Chem. Soc. 49, 1864 (1927).

[112] A. H. Morrish, The Physical Principles of Magnetism (Wiley, New York,1965), Chap. 3.

[113] A. M. Tishin, K. A. Gschneidner, Jr., and V. K. Pecharsky, Phys. Rev. B 59,503 (1999).

[114] B. R. Gopal, R. Chahine, and T. K. Bose, Rev. Sci. Instrum. 68, 1818 (1997).

[115] S. Y. Dan'kov, A. M. Tishin, V. K. Pecharsky, and K. A. Gschneidner, Jr.,Rev. Sci. Instrum. 68, 2432 (1997).

[116] M. W. Zemansky, Heat and Thermodynamics, 6th ed. (McGraw-Hill, New York, 1981).

[117] V. K. Pecharsky and K. A. Gschneidner, Jr., Appl. Phys. Lett. 70, 3299 (1997).

[118] S. M. Benford and G. Brown, J. Appl. Phys. 52, 2110 (1981).

[119] S. Y. Dan'kov, A. M. Tishin, V. K. Pecharsky, and K. A. Gschneidner, Jr., Phys. Rev. B 57, 3478 (1998).

[120] Y. Z. Shao, J. K. L. Lai, and C. H. Shek, J. Magn. Magn. Mater. 163, 103 (1996).

[121] S. Y. Dan'kov, V. V. Ivtchenko, A. M. Tishin, K. A. Gschneidner, Jr., and V. K. Pecharsky, Adv. Cryog. Eng. 46A, 397 (2000).

[122] Voraksmy BAN PhD thesis Université de Nancy 2011. and Talbott, For Refrigeration Problems, a Magnetically Attractive Solution, NIST, 2009. And Jiri Kastil “Magnetocaloric properties of rare-earth compounds”. Thesis Charles University in Prague 2014. And C. Aprea and A. Maiorino, ―A flexible numerical model to study an active magnetic refrigerator for near room temperature applications,‖ Appl. Energy, vol. **87**, 2010, pp. 2690– 2698.

[123] J.K.A. Gschneidner, V.K. Pecharsky, Annual Review of Materials Science, **30** (2000) 387-429.

[124] H. Wang, A. Pring, Y. Ngothai and B. O’Neill, Thermochim. Acta 427 13 (2005).

[125] H. Wang, I. Salveson, Phase Transitions, 78 (2005) 547-567

[126] Y.Ziat, Z. Zarhri, A. Slassi, A. Benyoussef, A. El Kenz, J. Supercond. Nov. Magn, 28 (2015) 3645-3649.

[127] A. Kavner, T. S. Duffy, G. Shen, Earth and Pl**nte Carlo study**anetary Science Letters, 185 (2001) 25-33.

[128] S. J. Kuhn et al, arXivpreprintarXiv:1603.01598, https://arxiv.org/abs/1603.01598

[129] A. Subedi, L. Zhang, D. J. Singh, M. H. Du, Phys. Rev. B, 78 (2008)134514

[130] A.H. Craig, Inst. Mining Metallurgy Trans, 75B (1966) 232.

[131] E. Hirahara, M. Murakami, J. Phys. Chem. Solids, 7 (1958) 281-289.

[132] H. Haraldsen, Zeitschriftfüranorganische und allgemeineChemie, 231(1937) 78-96

[133] J. L. Horwood, M. G. Townsend, A. H. Webster, J. Sol. State. Chem, 17 (1976) 35-42

[134] E.J. Schwarz and D. I. Vaughan, J. Geomag. Geoelec, 24 (1972) 441-458

[135] F. Li and F.H. Franzen, J. Alloys Comp, 215 (1994) L3-L6.

[136] L. Sagnotti, Iron sulfides. In Encyclopedia of Geomagnetism and Paleomagnetism. Springer (2007).

[137] S. Takele,G. R. Hearne, Phys. Rev. B, 60 (1999) 4401

[138] Anders Smith, The European Physical Journal H, 38 (2013) 507-517. https://doi.org/10.1140/epjh/e2013-40001-9

[139] V. K. Pecharsky and K. A. Jr Gschneidner, J. Magn. Magn. Mater., 167 (1997) L179.

[140] L. Caron et al., Phys. Rev. B 88, (2013) 094440.

[141] E. Brück, O. Tegus et al., Int. J. Refrig. 31, (2008) 763-770.

[142] H. Bińczycka Ž. Dimitrijević B. Gajić, A. Szytula, Physica status solidi (a), 19 (1973) K13-K17. https://doi.org/10.1002/pssa.2210190145

[143] Songlin; Dagula; Tegus, O.; Brueck, E.; Klaasse, J. C. P.; de Boer, F. R.; Buschow, K. H. J.

Journal of Alloys and Compounds.334 (2002) 249−252. https://doi.org/10.1016/S0925-8388(01)01776-5

[144] N. Biniskos, S. Raymond, K. Schmalzl, A. Schneidewind, J. Voigt, R. Georgii, P. Hering, J. Persson, K. Friese, T. Brückel. Physical Review B, 10 (2017) 104407.

[145] N. Sambhu. Datta, Shekhar Hansda, Chemical Physics Letters 621 (2015) 102-108.

[146] P. Hering, K. Friese, J. Voigt, J. Persson, N, Aliouane, A. Grzechnik, A. Senyshyn, T. Brückel. *Chem. Mater.*, 27 (2015) 7128–7136.

[147] Gourdon O, Gottschlich M, Persson J, de la Cruz C, Petricek V, McGuire MA, Brückel T. J. Solid State Chem., 216 (2014) 56-64.

[148] M. Herlitschke, B. Klobes, I. Sergueev, P. Hering, J. Persson, R. P. Hermann. Physical Review B. 93 (2016) 094304.

[149] Ling Wang and Anders W. Sandvik, Phys. Rev. Lett. **121**, 107202 (2018)

[150] W-Y. Liu, S. Dong, C. Wang, Y. Han, H. An, G-C. Guo, L. He, Gapless spin liquid ground state of spin-1/2 J1-J2 Heisenberg model on square lattices,arXiv preprint arXiv:1806.07031. (2018)

[151]J. Drisko, T. Marsh, J. Cumings, Nature communications,**8**, 14009 (2017)

[152]H. Ishikawa, N. Nakamura, M. Yoshida, M. Takigawa, Physical Review B, **95**, 064408 (2017)

[153] H. T. Diep, M. Debauche, H. Giacomini, Phys. Rev. **B43**(1991) 8759.

[154] V. Thanh Ngo and H. T. Diep, J. Appl. Phys. **103** (2008) 07C712.

[155] L. Balents, Nature **464**, 199 (2010).

[156] L. Shlyk, S. Strobel, B. Farmer, LE. De. Long, R Niewa, Physical Review B 97.5, **054426** (2018)

[157] B. Pang, L. Zhang, Y. B. Chen, J. Zhou, S. Yao, S. Zhang, Y. Chen, ACS applied materials & interfaces, **9**, 3201-3207(2017).

[158] R. Darradi, O. Derzhko, R. Zinke, J. Schulenburg, S. E. Krüger and J. Richter,Phys. Rev. **B 78**, 214415 (2008).

[159] A. A. Tsirlin and H. Rosner, Phys. Rev. **B 79**,214417 (2009).

[160] A. A. Tsirlin, A. Nath, A. M. Abakunov, R.V. Shpanchenko, C. Geibel and H. Rosner,

Phys. Rev. **B 81**, 174424 (2010).

[161] A. A. Tsirlin, A. A. Belik, R. V.Shpanchenko, E. V. Antipov, E. T.Muromachi and H. Rosner, Phys. Rev. **B 77**,092402 (2008).

[162] A. Farhan, C. F. Petersen et al, Nature communications, 8, 995(2017)

[163] T. Jiang, El. Magnotti, VP. Conticello Interface focus, 7, 20160141 (2017)

[164] S. Arai, S. Inoue, T. Hamai, R. Kumai, T. Hasegawa, Advanced Materials, 30, 1707256 (2018)

[165] CarolinBehncke, Christian F. Adolff et al, Scientific Reports, 8, 186 (2018)

[166] S. P. Chilakalapudi, A. Shahee, A. V. Mahajan, S. Srinath, B.Koteswararao, AIP Conference Proceedings 1832, 130032 (2017)

[167] P. Farkašovský, P. Eur. Phys. J. B 91, 74(2018) https://doi.org/10.1140/epjb/e2018-80650-7

[168] R. Moessner, A. P. Ramirez, Physics Today 59, 2, 24 (2006); doi: 10.1063/1.2186278.

[169] A. S. Wills, A. Harrison, S. A. M. Mentink, T.E. Masonj and Z. Tun, Europhys. Lett.**42**,

325 (1998).

[170] Y. Ziat, M. Boujnah, A.Benyoussef, A.El Kenz, Journal of Superconductivity and Novel

Magnetism, 28 (2015) 3397-3403

[171] Y. Ziat, M. Hammi, Z. Zarhri, C. Laghlimi, O. El Rhazouani, Journal of Magnetism and Magnetic Materials, 483 (2019) 219-223

[172] G. Turgut and E. Sönmez, Superlattices and Microstructures, 69 (2014) 175-186

[173] D. Zanders, E. Ciftyurek, et. al, Advanced Materials Interfaces, 6 (2019) 1801540. https://doi.org/10.1002/admi.201801540

[174] Ahmed, Ateeq, et al, Applied Surface Science, (2019).

https://doi.org/10.1016/j.apsusc.2019.03.209

[175] R. A. Nachiar S Muthukumaran, Optics & Laser Technology, 112 (2019) 458-466.

[176] M. Batzill, U. Diebold, Prog. Surf. Sci, 79 (2005) 47-52.

[177] TR. Cunha, IM. Costa, RJS. Lima, JGS. Duque, CT. Meneses, Journal of Superconductivity and Novel Magnetism, 26 (2013) 2299-2302

[178] M. A. Maki Jaskari, T. T. Rantala, Physical Review B, 65 (2002) 245428

[179] J. Oviedo, M. J. Gillan, Surface Science, 463 (2000) 93

[180] JM. Themlin, R. Sporken, J. Darville, R. Caudano, JM. Gilles, RL. Johnson, Physical Review B, 42 (1990) 11914.

[181] DF. Cox, TB. Fryberger, S. Semancik, Physical Review B, 38 (1988) 2072

[182] XL Wang, Z Zeng, XH Zheng, HQ Lin, Journal of applied physics,101 (2007): 09H104

[183] M. Yogeswari, G. Kalpana, Journal of Alloys and Compounds, (2013) 83-89.

[184] P. Wu, B. Zhou, W. Zhou, Applied Physics Letters, 100 (2012) 182405

[185] Julián Morales and Luis Sánchez, J. Electrochem. Soc,146 (1999), Issue 5, Pages 1640-

[186] S. Dalui, S.Rout, AJ. Silvestre, G. Lavareda, LCJ. Pereira, P. Brogueira, O. Conde , Applied Surface Science, 278 (2013) 127-131.

[187] L Dua, P K. Biswas, Applied Surface Science, 280 (2013) 33-41

[188] C. W. Zhang, C. W et al. Solid State Sciences, 13 (2011)1608-1611.

[189] X. L. Wang, Z. X. Dai, Z. Zeng, Journal of Physics: Condensed Matter, 20 (2008) 045214

[190] A. A. Bolzan, C. Fong, B. J. Kennedy, C. J. Howard, Acta Crystallogr. B53 (1997)

[191] H. Akai, Journal of Physics: Condensed Matter, 1(1989) 8045

[192] Á. Nagy, Physics Reports, 298 (1998)1-79

[193]VL. Mouruzzi, JF. Janak, AR. Williams Properties of Metals. Pergramon, New York (1998)

[194] Graduate-School-of-Science; Department-of-Physics; The University of Osaka, Machikaneyama-1-1,Toyonaka:560-0043, Japan. Introduction to AkaiKKR: http://kkr.issp.u-tokyo.ac.jp/

[195] Z. Zarhri, Y. Ziat, et. al , Journal of Physical and Chemistry of Solids, 9 (2016) 12-16

[196] E. Şaşioglu, L.M. Sandratskii, and P. Bruno, Journal of Physics: Condensed Matter,17 (2005) 995-1001

[197] DJ. Priour Jr, EH. Hwang, and SD. Sarma, Physical review letters, 92 (2004) 117201

[198] Y. Ziat, Z. Zarhri, M. Hammi, et. al, Solid State Communications, 237 (2016) 5

[199] Y. Ziat et al, Journal of Superconductivity and Novel Magnetism, 29 (2016) 2979-2985

[200] YH. Chang, CH. Park, K. Sato, H. Katayama Yoshida, Physical Review B, 75 (2007) 125211

[201] Y. Ziat, Z. Zarhri, A. Slassi, A. Benyoussef, A. El Kenz, Journal of Superconductivity and Novel Magnetism, 28 (2015) 3645-36

## Résumé

Dans cette thèse, Nous avons étudié les propriétés magnétiques des composés **FeS** et **$MnFe_4Si_3$** qui sont caractérisés par la température de Curie très élevée. D'abord, pour le composé **FeS** nous avons calculé les couplages d'interactions et décrit les propriétés électroniques en intervenant l'approximation de la théorie fonctionnelle de la densité (DFT), ainsi par l'implémentation du code Métropolise dans le cadre du model d'Ising on déduit les diagrammes de phase et les propriétés magnétiques du **FeS**. Nous avons étudié également l'effet magnétocalorique et les propriétés magnétiques dans l'alliage **$MnFe_4Si_3$** par méthode de simulation Monte Carlo (MCS) après avoir calculer les couplages d'interactions menés par les études expérimentales. Cette simulation a permis de mettre en évidence les performances et les fonctionnalités de ces composés dans différents domaines. Ensuite, nous avons mené une étude par MCS pour étudier la frustration magnétique dans un réseau carré due à la compétition des couplage ferromagnétique et antiferromagnétique ainsi on identifie les différents états possibles et précisément l'état frustré, de même on étudie les propriétés magnétiques et les cycles d'Hystérésis pour chaque état.

**Mots-clefs:** Simulation Monte Carlo; théorie fonctionnelle de la densité; Effet Magnétocalorique; Frustration magnétique.

## Abstract

In this thesis, we studied the magnetic properties of the FeS and MnFe4Si3 compounds which are characterized by the very high Curie temperature. First, for the compound **FeS** we calculated the interaction couplings and described the electronic properties by intervening the approximation of the functional density theory (DFT), thus by the implementation of the Metropolis code within the framework of the model from Ising we deduce the phase diagrams and the magnetic properties of FeS. We also studied the magnetocaloric effect and the magnetic properties in the MnFe4Si3 alloy by Monte Carlo simulation method (MCS) after having calculated the interaction couplings carried out by experimental studies. This simulation shows the performances and the functionalities of these compounds in various fields. Then, we carried out a study by MCS to study the magnetic frustration in a square lattice due to the competition of the ferromagnetic and antiferromagnetic coupling so we identify the different possible states and precisely the frustrated state, so we studied the magnetic properties and the hysteresis cycles for each state.

**Keys words**: Monte Carlo simulation; Functional Density Theory; Magnetocaloric Effect; Magnetic Frustration.

**Année Universitaire : 2020-2021**